BIOENGINEERED NANOPARTICLES FOR TARGETED CANCER THERAPY

DISSERTATION

Presented to the Graduate Council of the

Graduate School of Biomedical Sciences

University of North Texas Health Science Center

in Partial Fulfillment of the Requirements

For the Degree of

DOCTOR OF PHILOSOPHY

BY

ANDREW S. GDOWSKI

Fort Worth, Texas

April 5, 2018

ACRONYMS

ADT-androgen deprivation therapy

BMPs- bone morphogenetic proteins

BS3- bis [sulfosuccinimidyl] substrate

CBFA1- core-binding factor alpha 1

CTC- circulating tumor cell

CXCR4- CXC-chemokine receptor 4

EBRT- external beam radiation therapy

EDTMP- ethylenediaminetetramethylene phosphate

EMT- epithelial-to-mesenchymal

FGF- fibroblast growth factor

FRR- flow rate ratio

FTIR- Fourier transform infrared spectroscopy

HIFU- high intensity focused ultrasound

IMRT-intensity modulated radiation therapy

M-CSF- macrophage colony stimulating factor

NLP- nanolipomer

NCCN- National Comprehensive Cancer Network

NP- nanoparticle

OPG- osteoprotegerin

P-BiNPs- programmable bioinspired nanoparticles

PDGF- platelet-derived growth factor

PDI- polydispersity Index

PI3K- phosphatidylinositol-4,5-bisphosphate 3 kinase

PLGA- poly (lactic-co-glycolic acid)

PVA- poly vinyl alcohol

QOL- quality of life

RANKL- receptor activator of nuclear factor-κB ligand

SBRT- stereotactic body radiation therapy

SDF-1- stromal derived factor-1

SEM- scanning electron microscopy

SSRT- spinal stereotactic radiation therapy

TEM- transmission electron microscopy

TFR- total flow rate

TNF- tumor necrosis factors

TNF alpha- tumor necrosis factor alpha

TGF-β-transforming growth factor β

VCAM-1- vascular cell adhesion molecule 1

VEGF- vascular endothelial growth factor

ACKNOWLEDGEMENTS

I would like to offer my sincere gratitude to the following people who have helped me with the completion of my thesis:

Dr. Jamboor K. Vishwanatha for providing mentoring and direction along the PhD process.

Dr. Amalendu Ranjan who has provided me with insights and knowledge into the engineering and testing of nanoparticles.

Past and present lab members of the Vishwanatha lab who have helped me with experiments and discussions.

My committee members: Dr. Albert Yurati, Dr. David Cistola and University Member Dr. Robert Leudkte who have provided constructive criticism, suggestions, and guidance on experiments.

All the professors and clinicians that have taught me throughout medical school and graduate school.

Most importantly my family and friends for the support they have provided throughout the dual degree program.

TABLE OF CONTENTS

LIST OF TABLES

LIST OF FIGURES

CHAPTER I

INTRODUCTION

I. GENERAL INTRODUCTION TO THESIS

The overarching goal of this thesis was to develop novel bone targeted nanoparticle therapies. The main emphasis was focused on metastatic prostate cancer but various components and ideas contained within this thesis are applicable to other cancers that metastasize to the bone. Metastatic prostate cancer was chosen due to the limited current therapeutic options, poor survival outcomes, and diminished quality of life in these patients.

The first chapter of this thesis is a general introduction to bone metastasis. It covers the current biological understanding of the "seed and soil" hypothesis which comprises the main factors contributing to the ability of tumor cells to create bone lesions. It also summarizes the current landscape of treatment options that are available to patients with bone metastasis. Finally, all currently ongoing clinical trials (as of 2017) that involve bone metastatic therapies have been categorized to give the reader an impression of options that may be available to patients in the near future.

The second chapter describes a unique formulation of bone targeted nanoparticles engineered to target metastases by binding to the hydroxyapatite structure of the bone in areas of high bone turnover. Subsequently, releasing the nanoparticle therapeutic cargo at the site of the tumor. In the pre-clinical evaluation, this nanoparticle system was efficacious at tumor reduction, preserving bone structure, and decreasing pain.

The third chapter demonstrates a promising approach to engineering a programmable bioinspired nanoparticle targeting system through guidance from genomic information of prostate cancer patients. This nanoparticle utilizes a stimulated cancer cell membrane to cloak the nanoparticles and improve nanoparticle bone adhesion and homotypic targeting to prostate cancer cells.

Chapter four addresses the challenge of scaling up the process of nanoparticle development from the lab size batches to clinical trial size batches. In this chapter, we have developed a microfluidic process which can be used for seamless optimization of small nanoparticle batches and translation to large batches.

Chapter five describes the development and characterization of an addition nanoparticle system and focuses on the technical challenges of encapsulating a monoclonal antibody within a polymeric nanoparticle. This nanoparticle is unique because the design could allow delivery of monoclonal antibodies to the interior of cells which has previously been a challenge for drug delivery.

Finally, chapter six summarizes the projects contained within this thesis and discusses future directions in translating these targeting concepts into clinical realities for patients with bone metastatic cancers.

II. INTRODUCTION TO BONE METASTASIS

Elucidation of mechanisms regulating bone metastasis has progressed significantly in recent years and this has translated to many new therapeutic options for patients with bone metastatic cancers. However, the rapid rate of progress in both the basic science literature and therapies undergoing clinical trials makes staying abreast with current developments challenging. This review seeks to provide an update on the current state of the science in bone metastasis research and give a snap shot of therapies in clinical trials for bone metastatic cancer.

Bone metastasis represents a difficult to treat clinical scenario due to pain, increased fracture risk, decreased quality of life and diminished overall survival outcomes. Multiple types of cancer have the specific ability to home to the bone microenvironment and cause metastatic lesions. This osteotropism was first described by Stephen Paget nearly 100 years ago as the 'seed and soil' hypothesis. Once cancer cells arrive at the bone they encounter a variety of cells native to the bone microenvironment which contribute to the establishment of bone metastatic lesions. In the first part of this review, the 'seed and soil' hypothesis is revisited while emphasizing recent developments in understanding the impact of native bone microenvironment cells on the metastatic process. Next, approved therapies for treating bone metastasis at the systemic level as well as those that target the bone microenvironment are discussed and current National Comprehensive Cancer Network (NCCN) guidelines relating to treatment of bone metastases are summarized. Finally, all open interventional clinical trials for therapies relating to treatment of bone metastasis have been complied and categorized.

Understanding the recent advancements in bone metastasis research is important for continued development of novel bone targeted therapies. The plethora of ongoing clinical trials will hopefully translate into improved treatments options for patients suffering from bone metastatic cancers.

Treatment options and survival outcomes for patients with many types of cancer have improved during the past 50 years[1, 2]. While these improvements are encouraging, those patients who present with metastatic cancer almost ubiquitously face poor prognosis. Patients with metastatic solid tumors are generally not candidates for surgical resection of their primary tumor which immediately limits therapeutic options. Additionally, there is ample room for improvement in the repertoire of the medical therapeutic options that are currently approved for these patients with metastasis. Understanding the mechanisms and engineering solutions is critical to advancing therapies and improving outcomes in patients who develop metastases. Indeed, new therapeutics are under development and in clinical trials with the goal to improve survival, alleviate pain and decrease fracture risk in patients with bone metastatic cancers.

"Seed and Soil" Hypothesis

Tumor cells necessarily require interaction with the microenvironment of a specific host organ to create a metastatic lesion[3]. This concept was first described over 100 years ago by the English surgeon, Stephen Paget. Paget described the 'seed and soil' hypothesis in which he sought to explain why certain cancers favored developing metastasis in specific organs. In his research, he studied the autopsy results of patients who had various primary tumors and found that these

patients had specific organ patterns where the metastases developed. For example, he found that women who had breast cancer had a much greater probability of having metastases to the bone than any other organ. He explained these results by proposing that the tumor cells acted as 'seeds' and have an affinity for particular organs or the 'soil'. Thus, metastases will develop when the right combination of a compatible seed is planted in the right soil[4, 5] (Figure 1).

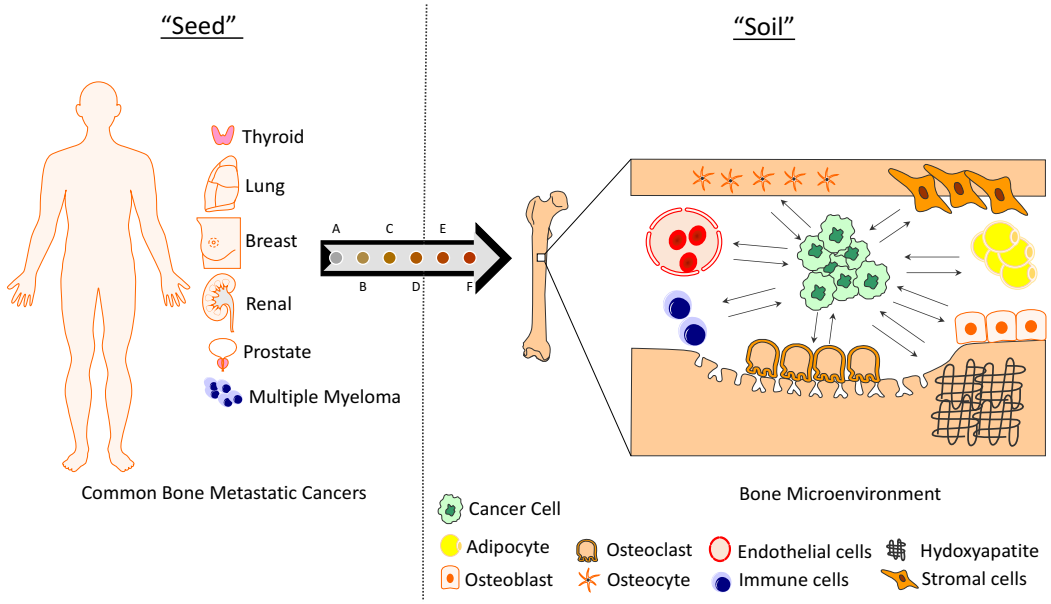

Figure 1: Depiction of the seed and soil hypothesis. The most commonly bone metastatic cancers are: thyroid, lung, breast, renal, prostate, and multiple myeloma. The bone microenvironment can be viewed as the soil and contains multiple entities that impact cancer cell survival and establishment of bone lesions. The metastatic process involves: **(A)** Primary tumor, **(B)** Angiogenesis, **(C)** Local invasion and intravasation, **(D)** Dissemination via circulation, **(E)** Extravasation, and **(F)** Colonization of a metastatic site (bone). Components of the bone

microenvironment include: endothelial cells, osteocytes, stromal cells, adipose cells, osteoclasts, osteoblasts, T cells, B cells, and the chemical structure of the bone.

Metastatic Process

This complicated process is precisely coordinated and the molecular basis underlying its orchestration from initiation to development of distant metastasis is a vigorous area of research. The initial step in metastasis necessitates that the cancer cells escape from the primary tumor and into systemic circulation. Cancer cells accomplish this through a process termed epithelial-to-mesenchymal transition (EMT). This transformation enables epithelial type cancer cells to undergo a phenotypic change to exhibit mesenchymal traits such as loss of cell surface intercellular adhesion proteins and loss of epithelial polarization[6]. The cancer cells also secrete extracellular proteolytic enzymes to dissolve the extracellular matrix and escape the physical environment of the tumor stroma[7]. The most prominent of these factors are the matrix metalloproteinase enzymes[8]. After an adequate amount of the extracellular matrix has been dissolved, the cancer cells become locally invasive and begin to migrate into surrounding tissue[9]. Cancer cells continue to migrate through the endothelial cells to gain access to systemic circulation through a process called intravasation[10]. This process is mediated at the vascular level by the tortuous and leaky tumor vasculature[11] as well as cell signaling aberrations in the cancer cells that increase cellular adhesion factors such as integrin B1, enabling the cancer cells to interact with the endothelium[12].

Once cancer cells invade blood vessels and get into systemic circulation, they are termed circulating tumor cells (CTC) and are presented with a new set of challenges. The circulatory system is an inhospitable environment but metastatic tumor cells have mechanisms to improve their chances of survival[13]. One example of how these cells survive is by inhibiting anoikis. Anoikis is normally an apoptotic process which cells undergo when there is loss of cell-matrix or cell-cell interactions. As such, the deregulation of anoikis in the context of metastasis is likely present before cancer cells intravasate and continues during the circulation process[14]. One specific example that has been linked to anoikis resistance is a tyrosine kinase receptor, TrkB. It has been shown that overexpression of this receptor on the membrane of cancer cells, results in activation of the phosphatidylinositol-4,5-bisphosphate 3 kinase (PI3K)-AKT pro-survival pathways[15]. Cancer cells also have mechanisms to escape destruction by immune cells, such as macrophages, by upregulating certain cell surface proteins like CD47[16].

The two main factors impacting the location CTCs will develop a metastatic lesion are: blood flow and molecular signaling. This is particularly true for cancers that metastasize to the bone. Consider the example of breast cancers which have a preference to metastasize to the thoracic spine due to venous drainage of the breast from the azygos venous system communicating with the plexus of Batson in the thoracic region[17]. This is in comparison to lung cancers which show a more general skeletal distribution due to venous drainage from the pulmonary veins into the left side of the heart and from there dissemination to systemic circulation[18]. Alternatively, the majority of prostate cancer metastasis are seen in the axial skeleton in the lumbar spine, sacrum, and pelvis due to venous drainage of the prostate through the pelvic plexus[19]. Further, colon cancer is known to metastasize to the liver due to portal venous drainage[20]. However, blood flow

patterns do not fully explain the distribution of metastatic lesions. In addition to blood flow, a plethora of other factors and signaling events are crucial in the dissemination of CTCs. One well documented process is CTC homing to the bone marrow microenvironment.

One of the signaling pathways regulating CTC homing to the bone is the CXCL12-CXC-chemokine receptor 4 (CXCR4) axis[21]. CXCL12, also called stromal derived factor-1 (SDF-1), is a chemokine factor that is made by bone marrow mesenchymal stem cells, endothelial cells, and osteoblasts. CXCL12 binds primarily to the g-protein coupled receptor, CXCR4, activating several divergent intracellular signaling pathways that are involved in cellular processes including: cell survival, gene transcription, chemotaxis, and expression of integrins such as integrin avB3 on the surface of the CTCs[22]. The increased expression of avB3 on the surface of the metastatic prostate tumor cells has been shown to cause it to adhere to endothelial cells of the bone marrow[23]. The CXCL12-CXCR4 axis is not only important for CTC from solid tumors, but also plays a significant role in hematopoietic stem cells and leukemia cells homing to the bone marrow[24, 25]. Other molecules have shown importance in the adhesion process as well. These include others factors such as integrin $\alpha4\beta1$[26], annexin II[27], and E-cadherin[28].

In addition to the significance of CXCL12-CXCR4 axis for cell adhesion in cancer cells, this signaling pathway has also been shown to be important in cancer cell survival. In fact, breast cancer cells that aberrantly express the non-receptor cytoplasmic tyrosine kinase, Src, have improved survival in the bone marrow. It was shown that Src mediates this improved survival through Akt signaling in response to CXCL12-CXCR4 stimulation and through increasing

resistance to TNF-related apoptosis-inducing ligand (TRAIL) specifically in the bone marrow microenvironment[29].

Bone Microenvironment

Once the process of homing and extravasation have taken place, the metastatic cells encounter native bone microenvironment cells. These cells play a vital role in maintaining homeostasis of the bone and include: osteoclast, osteoblasts, osteocytes, endothelial cells, and cells of the bone marrow. The growth and dynamic turnover of bone is regulated through precise signaling between these cells. Alteration in the homeostasis of these native cells can have disastrous effects. When cancer cells infiltrate the bone, the lesions that develop are traditionally classified as either osteolytic, in which bone is broken down, or osteoblastic, in which bone is formed[30]. These processes are not binary. Rather, both the osteoclastic and the osteoblastic activities are generally activated in all metastatic bone lesions[31]. However, depending on which process is dominant the radiological appearance of a bone metastasis is either lytic, sclerotic, or mixed. The cancers that conventionally cause osteolytic lesions are breast and multiple myeloma[32]. These types of lesions can be particularly dangerous and have the highest rates of fracture. Osteoblastic lesions are seen most often with metastases from prostate cancer[33] and have an increased risk of fracture due to the altered architecture of the bone but not to the same degree as in osteolytic lesions.

The cells responsible for bone resorption are known as osteoclasts. These cells are monocyte-macrophage derived multinuclear cells that are initially inactive[34]. Osteoclasts generally are positioned in resorption pits and when activated secrete cathepsin K. This creates an acidic

environment on the underside of the osteoclast where the cell maintains a sealed ruffled border[35]. Osteoclast activation is under the control of both systemic factors as well as locally secreted cytokines. Parathryroid hormone, 1,25-dihydroxyvitamin D_3, and prostaglandins cause upregulation of receptor activator of nuclear factor-κB ligand (RANKL)[36, 37]. RANKL is a family member of tumor necrosis factors (TNF) which is expressed on the membrane surface of both stromal cells and osteoblasts as well as released by active T cells. Structurally, RANKL is a homotrimeric type II membrane protein with three isoforms[38]. The full length version of RANKL is denoted RANKL1. RANKL2 is shorter due to a portion of the intracytoplasmic domain missing. While RANKL3 is the soluble isoform and has the N-terminal portion deleted[38]. RANKL activates osteoclasts by signaling though its receptor, RANK, with subsequent activation of nuclear factor-κB and Jun N-terminal kinase pathways. Locally, stromal cells and osteoblasts also activate osteoclasts by production of macrophage colony stimulating factor. Additional control over osteoclast activation is managed by osteoprotegerin, which is a decoy receptor for RANKL and is normally present in the marrow[39]. An altered ratio of osteoprotegerin to RANKL can result in osteopetrosis or osteopenia[40, 41].

In addition to the osteoclasts, osteoblasts have a major role in maintaining the bone structure. These cells originate from mesenchymal stem cells and are responsible for synthesizing new bone[42]. This is a critical function, not only during development but also throughout life. Several factors allow for successful differentiation of osteoblasts such as bone morphogenetic proteins (BMPs), platelet-derived growth factor (PDGF), fibroblast growth factor (FGF) and transforming growth factor β (TGF-β)[43, 44]. The differentiation of osteoblasts is not as well understood as the process in osteoclasts, but one factor that is known to drive the differentiation process is the

transcription factor Runx-2, also called core-binding factor alpha 1 (CBFA1)[45]. As osteoblasts become more mature they secrete osteocalcin and calcified matrix, eventually becoming osteocytes as they are encapsulated within the bone[46].

Osteocytes make up approximately 90% of the bone cells in the adult human, however less is known about their role in bone metastasis than osteoblasts and osteoclasts[47]. Even though osteocytes are surrounded by the bone matrix, they communicate through an extensive lacunar-cannicular network which connects the osteocytes to other osteocytes, the bone surface, and marrow cells. They regulate osteoclast development through expression of: RANKL, macrophage colony stimulating factor (M-CSF) and osteoprotegerin (OPG). In addition, they can inhibit osteoblasts by expression of sclerostin[48]. Osteocytes have an interesting ability to respond to stress and pressure. In fact, increased pressure in the bone from prostate cancer metastasis can upregulate matrix metalloproteinases and CCL5 in osteocytes resulting in increased tumor growth[49]. IL-11 has been shown to be released from apoptotic osteocytes causing osteoclast differentiation[50]. Additionally, physical interactions and secreted factors from cancer cells such as multiple myeloma cells impact osteocyte function[51].

Endothelial cells comprise another component of the bone microenvironment that contribute to the bone metastatic process through a variety of mechanisms. Endothelial cells in the metaphysis of long bones are known to constitutively express P-selectin, E-selectin, vascular adhesion molecule 1 and intercellular adhesion molecule A which aid in CTC adhesion when they travel through the bone marrow[52]. The physical architecture of the bone vasculature also plays a role in

the homing process. The large volume of sinusoids decreases blood flow velocity thus decreasing shear forces and increasing the favorability for attachment of cancer cells[53]. Additional mechanisms by which the endothelial cells promote bone metastatic lesions are through promotion of cell dormancy and neovascularization for metastatic growth[54]. Tumor cells can secrete angiogenetic factors such as vascular endothelial growth factor (VEGF) and IL-8 that can serve to increase survival of the tumor cells and neovascularization[55].

More recent evidence has demonstrated the importance of immune cells in the development of bone metastases. The bone marrow is a major reservoir for dendritic cells, macrophages, myeloid derived cells, and different subsets of T cells[56]. T cells have been shown to regulate bone resorption in both solid tumors bone metastasis and multiple myeloma[57, 58]. T cells and B cells also produce RANKL and can impact osteoclastogenesis. IL-7 is an important cytokine that mediates interactions between T cells and the proliferative bone metastatic environment[59]. Myeloid derived suppressor cells from the bone marrow have proven to be impactful in their ability to drive cancer progression through suppression of innate and adaptive immune responses, impairing T cell antigen recognition and promotion of T regulatory cells[60-62]. In the microenvironment of multiple myeloma patients, dendritic cells and IL-6, IL-23 and IL-1 are involved in increased Th17 cells, which increase IL-17 and can promote osteoclast and myeloma proliferation[48]. Additionally, IL-17 has been shown to be a growth factor for both prostate and breast cancer cells[63, 64].

During development, the bone marrow changes from being predominately red or hematopoietic marrow and having very little adipocytes or yellow marrow to being composed of approximately 70% adipose tissue, by the age of twenty five[65]. These adipocytes were previously thought to be inert but now are considered to have a significant impact on the development of bone metastasis in the microenvironment. It has been proposed that adipocytes play a supporting role for cancer cell survival in the bone marrow as an energy source[66, 67]. Bone marrow adipocytes also secrete several pro-inflammatory mediators such as IL-1B, IL-6, leptin, adiponectin, vascular cell adhesion molecule 1 (VCAM-1), tumor necrosis factor alpha (TNF-alpha) and CXCL12 that increase bone tropism, proliferation, and survival of certain cancer cells[65, 68-70].

Additionally, cancers cells that are already within the bone microenvironment play in impactful role on the further development of these metastatic lesions. Important activating factors expressed by the prostate cancer cells that create bone metastasis include: FGFs[71] and BMPs[72]. It has been shown that FGF can act through autocrine or paracrine signaling[73]. Binding of FGF to an FGF receptor results in activation of multiple signal transduction pathways beneficial for the tumor. These stimulated pathways include: phosphatidylinositol 3-kinase (PI3K), phospholipase Cγ (PLCγ), mitogen-activated protein kinase (MAPK), and signal transducers and activators of transcription (STAT)[31, 73]. The resulting stimulation of these pathways from multiple FGFs results in simulation of the cells in the bone microenvironment and the cancer cells during metastatic lesion development[31].

The mineral structure of the bone itself presents additional components that can serve to enhance bone metastatic lesions. Encased within the hydroxyapatite are a number of factors such as: bone morphogenetic proteins, insulin like growth factors I and II, platelet-derived growth factor, transforming growth factor-beta and fibroblast growth factor[74]. These factors become important when liberated from the mineralized hydroxyapatite by promoting growth and proliferative effects on tumor cells and worsening the metastatic lesion.

III. CURRENT BONE METASTASIS THERAPIES

Introduction to treatment concepts

Therapeutic strategies for bone metastatic cancers rely on three main principles: 1.) The cancer cells should be treated. This is critical because the cancer cells are the initial insult which cause bone metastatic lesions to develop. If cancer cells continue to proliferate and divide, it should not be expected that survival time will be extended. This principle can be broken down further into therapies that are cytotoxic and kill the cells, hormonal deprivation, or targeted agents that inhibit specific signaling pathways; 2.) Targeting the bone microenvironment is impactful. As was discussed in the above sections on the bone microenvironment, the complex biological signaling between cancer cells and bone resident cells creates a vicious cycle. Disruption of these interactions represents a therapeutic opportunity; 3.) Palliative therapies focus on alleviating symptoms associated with bone metastasis. This becomes an area that can be very impactful on the quality of life for these cancer patients as bone metastasis can be extremely debilitating and painful.

Most of the following discussion on approved therapeutics will focus on prostate, breast, and multiple myeloma. These are the most common cancers which cause bone metastatic lesions and thus represent the bulk of research efforts to understand the mechanisms involved. Patients with other cancers such as kidney, thyroid, lung and melanoma can also present with metastasis to the bone. There are many treatment commonalities between the various cancers that metastasize to the bone and strategies appropriate for one type of cancer are often effective for others.

Bisphosphonates

Bisphosphonates are a unique drug class that have been used in multiple clinical settings for their ability to prevent bone loss. In addition to their role in the treatment of patients with bone metastatic cancer, they are also clinically effective for use in osteoporosis, Paget's disease and osteogenesis imperfecta[75-77]. However, use of these agents is not without the potential for adverse side effects such as osteonecrosis of the jaw, esophageal irritation, and fractures[78, 79].

The bone targeting ability of bisphosphonates for the mineral structure of hydroxyapatite is due to their chemical configuration. Bisphosphonates consist of two phosphonate groups that are bound by a carbon atom. Additional functional groups have been attached to the central carbon atom which confers different pharmacological properties to these molecules. The two phosphonate groups in these drugs allow high binding affinity to the hydroxyapatite structure and this is enhanced in areas of high bone turnover such as bone metastatic lesions[80, 81]. Depending on the side groups of the bisphosphonate molecule either a bidentate bond forms

through calcium ion chelation on the surface of the hydroxyapatite or a stronger tridentate bond can form [82,83].

Bisphosphonates can be subdivided based on the presence of a nitrogen containing side group. The clinically approved nitrogen containing molecules are ibantdronate, pamidronate, alendronate, risedronate and zoledronate. The nitrogen free bisphosphonates are clodronate, tiludronate and etidronate[84]. Zoledronic acid has been shown to have the best efficacy among the bisphosphonate molecules and was approved based on its ability to prolong the time to symptomatic skeletal related events but did not show an improvement in overall median survival when compared to the placebo[85].

The overall mechanism of bisphosphonates is to inhibit bone resorption through its apoptotic effects on osteoclasts after being endocytosed. Uptake causes osteoclast apoptosis through one of two main mechanisms depending on the class of bisphosphonate. Endocytosis of non-aminobisphosphonates results in disruption of ATP supply as osteoclasts metabolize this class into analogues of ATP and eventually undergo apoptosis[86]. The mechanism by which amino-bisphosphonates cause apoptosis in osteoclasts is through inhibition of farnesyl pyrophosphate synthase and the mevalonate pathway[87]. Additionally, osteoclast apoptosis limits the vicious cycle of signaling that takes place between the osteoclasts and cancer cells in the bone microenvironment.

Denosumab

Denosumab was FDA approved based on the study by Fizazi et. al in 2011 where they showed a prolonged time to skeletal related event by 3.6 months compared to zoledronic acid[88]. Denosumab is a human monoclonal IgG2 antibody that acts by binding to both membrane bound and soluble RANKL with high affinity[89, 90]. As was discussed in earlier sections, RANKL is a molecule that is primarily secreted by osteoblasts and upon attachment to RANK (located on osteoclasts) stimulates osteoclastic activity. The exact location of binding of denosumab is on the DE loop region of RANKL, which forms a contact with RANK[91]. Thus, treatment with denosumab prevents this contact and inhibits bone resorption. In addition to the RANKL that is secreted by osteoblasts, inflammatory cells and stromal cells also secrete RANKL and impact tumor development[92, 93]. In the clinical setting, denosumab has shown positive results in preventing pain[94, 95], lessening hypercalcemia of malignancy[89, 96] and may also have effects on tumor cells independent of its role in bone homeostatsis[89].

Radioisotopes

Radioisotopes also play a role in the treatment of bone metastasis. Ideal candidates for this type of therapy are generally those with osteoblastic or mixed metastatic lesions that are multifocal and causing significant pain[97]. Approved radioisotopes for treating bone metastasis are either members of the alkaline earth metals or conjugated to ligands that can direct the radioisotope to the bone. Alkaline earth metals have the same electron valence as calcium so they are concentrated to areas of high bone turnover along with calcium. As a class, these agents are

effective at reducing pain associated with bone metastasis but haven't shown to be effective at prolonging overall survival until the most recently approved radioisotope, radium-223[98, 99].

Clinically approved radioisotopes can be divided into β-emitters and α-emitters. Two β-emitters, Stontium-89 and Samarium-153, are approved for treating bone pain in patients with bone metastases. These agents deliver ionizing radiation and incorporate into the bone. Strontium can incorporate due to its similarity to calcium and Samarium-153 has been conjugated to ethylenediaminetetramethylene phosphate (EDTMP) which can chelate calcium to allow it to home to the bone[100]. These β-emitters are considered outdated due to other therapeutics with stronger evidence[101].

Radium-223 is an α-alpha emitting radioisotope. It has been approved based on the results of the ALSYMPCA trial after demonstrating not only prolonged time to skeletal related event by 5.8 months as compared to a placebo but also increased overall median survival by 3.6 months[102]. Alpha-emitters can deliver high radiation but the depth of radiation penetration in tissues is less, making them more targeted[103]. As a group, radiopharmaceuticals that target the bone have high rates of myelosuppresion[104]. The adverse effects of Radium-223 appear to be less, with only mild thrombocytopenia[105].

Hormonal Therapy and Chemotherapy

One of the most important goals in the treatment of bone metastatic cancer is disease control. If a cancer is localized, surgery or radiation therapy are generally the first choice. However, for advanced bone metastasis disease, systemic therapy is often required with either cytotoxic agents, targeted therapies, hormonal therapy or a combination of the above. In advanced hormonally driven tumors such as prostate and breast, the first line treatment is hormone deprivation to cut off the proliferative signaling in the cancers. The standard treatment for men with advanced prostate cancer for the past 70 years has been androgen deprivation therapy[106, 107]. There is typically a good initial response to treatment but almost inevitably the patient will become refractory to the treatment and will progress to castration resistant prostate cancer in a period of 18 to 24 months[108]. As the cancer progresses, it will metastasize to the bone in 90% of patients[109] and at this point overall survival is generally less than 2 years[110].

Two newer anti-androgen agents are approved in the setting of castration resistant bone metastatic prostate cancer. Abiraterone inhibits 17-α-hydroxylase/17,20 lyase, which is a testosterone synthesis enzyme that is found in the adrenals, testes and tumor[111]. Enzulatamide is an antiandrogen and exerts its effect by inhibiting nuclear translocation of the androgen receptor, inhibiting the androgen receptor from binding to DNA and blocking co-activator recruitment[101, 112]. The androgen receptor also promotes growth in the bone microenvironment through its expression and activity in the bone microenvironment stromal cells[113].

Cytotoxic chemotherapy is also approved in the context of bone metastatic prostate cancer. Docetaxel is a microtubule inhibitor and was the first chemotherapeutic to show a survival benefit in these patients[114]. More recent results of the STAMPEDE trial showed a survival benefit in prostate cancer patients when docetaxel was started earlier in the treatment course along with long term androgen deprivation treatment[115]. Cabazitaxel is a newer generation taxol and was developed to treat patients who have previously been treated with docetaxel. It was chemically modified in two locations from the previous docetaxel drug. These alterations give it decreased affinity for the P-glycoprotein pump which on many advanced cancer cells can pump chemotherapy out of the cell rendering it resistant to therapy. It was approved based on the results of the TROPIC trial which showed an overall survival benefit compared to mitoxantrone in patients who were previously treated with docetaxel[116].

The concepts that guide the standard of care for patients with bone metastatic breast cancer are similar to those guiding prostate cancer therapy. Treatment options include systemic agents against the cancer, bone-targeted agents and local therapy as well[117]. The current recommendation is for initiation of endocrine therapy in women who experience recurrence and who are estrogen receptor positive, with the exception if there is rapidly developing disease and organ involvement, in which case chemotherapy should be offered[118]. In addition, bone targeted agents such as bisphosphonates and denosumab are important in delaying skeletally related events such as fractures and for improvement in pain.

Immunotherapy

Development and approval of immunotherapy for cancers in general has made considerable progress and attracted interest in recent years. In the advanced prostate cancer field, Sipuleucel-T has been approved after showing a survival benefit in castration-resistant prostate cancer patients who are asymptomatic or minimally symptomatic[119]. It is made using a patient's own mononuclear cells that are sent to a central processing facility and treated with prostatic acid phosphatase and granulocyte/macrophage colony stimulating factor. These cells are injected back into the patient and the antigen presenting cells activate the patient's T cells to attack the prostate cancer[120]. As the field of immune-oncology continues to expand, specific bone directed therapies may materialize.

Percutaneous Minimally Invasive Techniques

Treatments such as percutaneous vertebroplasty, kyphoplasty, and radiofrequency ablation are often employed as a palliative measure in the treatment of patients with bone metastatic spinal tumors[121]. In the percutaneous vertebroplasty procedure bone needles are placed into the vertebral body, and polymethylmethacrylate (quick setting bone cement) is injected. The reduction in pain is likely due to restoration of vertebral height and the exothermic nature of the bone cement as it sets[121]. Balloon kyphoplasty is like vertebroplasty but utilizes a balloon to control bone cement extravasation in the spine[122]. Radiofrequency ablation uses alternating current to generate heat and multiple mechanisms may be contributing to reduction in pain such as: cancer cell death causing reduction in pain inducing cytokines, decreasing size of cancer bone

lesions, destruction of pain fibers and inhibiting osteoclastogenesis[123]. The goal of these therapies is palliation of pain symptoms so that overall quality of life is improved.

Radiation Therapy

Radiation therapy is another palliative approach to treating bone metastasis. It is a non-invasive and effective way to improve pain from these lesions generally within 2-6 week of treatment [117]. This treatment can be performed by dose fractionation in which multiple doses of radiation are given or administered in a single-dose[124-126]. The ideal candidates for this therapy are those with solitary or oligometastatic disease to the bone[127].

Surgery

Surgical intervention is generally not the first option in patients with bone metastasis but may be helpful in certain instances. For spinal tumors, hormonal and radiation treatments are considered first. However, decompression laminectomy and fixation as well as en bloc spondylectomy may be beneficial in appropriately selected patients[128]. Treatments for metastasis to long bones include internal fixation, external fixation and prosthesis placement[129, 130].

NCCN Guidelines Summary of Bone Metastatic Cancer Treatments

Table 1. Treatment options for various types of bone metastatic cancers

	Prostate	Breast	Renal	Lung	Thyroid	Multiple Myeloma
Systemic Therapy	Yes	Yes	Yes	Yes	Yes	Yes
Bone-Targeted	Denosumab Zoledronic Acid Radium-223	Denosumab Zoledronic Acid Pamidronate	Denosumab Zoledronic Acid	Consider: Denosumab Zoledronic Acid	Denosumab Pamidronate Zoledronic Acid	Pamidronate Zoledronic Acid
Radiation Therapy	Yes	Yes	Yes	Yes	Yes	Yes
Vitamins	Calcium Vitamin D	Calcium Vitamin D	Calcium Vitamin D	Not Mentioned	Not mentioned	Not mentioned
Notes	Possible use of Sr-89 or Sm-153				Consider embolization prior to surgical resection to reduce hemorrhage	

Table 1: Compilation of the individual 2017 National Comprehensive Cancer Network (NCCN) cancer treatment guidelines for recommendations on treating bone metastasis.

Cancers with the highest bone metastases prevalence were selected.

Clinical trials in bone metastasis

Table 2. Summary of Current Clinical Trials for Bone Metastatic Cancers

Therapy	Clinical Trial Description	Multiple Cancers	Prostate	Breast	Renal	Thyroid	Lung	Myeloma
Radiotherapy	Hypofractionated radiotherapy regimen	NCT02376322						
	SBRT vs EBRT	NCT00922974						
	1 vs 2 fractions of EBRT	NCT02699697						
	Dose regimen of radiotherapy	NCT02163226						
	SBRT + ADT	NCT02563691						
	IMRT vs EBRT	NCT02832830						
	EBRT +/- hyperthermia	NCT01842048						
	Surgery +/- postoperative radiotherapy	NCT02705183						
	Treatment of opiod refractory pain with pituitary radiosurgery	NCT02637479						
	LHRH agonist + Enzulutamide +/- SBRT		NCT02685397					
	ADT +/- radiotherapy		NCT02913859					
	SBRT + anti PD-1 antibody			NCT02303366				
	SBRT with sunitinib				NCT02019576			
	FDG-PET guided radiotherapy with conventional dose vs FDG-PET with SBRT dose escalation	NCT01429493						
	Conventional radiotherapy vs SBRT	NCT02364115						
	SBRT workflow	NCT02145286						
	SBRT	NCT02880319						
	Single fraction SSRTvs multple fraction SSRT	NCT02608866						
	Zoledronic acid + high dose radiotherapy or low dose radiotherapy						NCT02480634	
	Conventional radiotherapy vs SBRT	NCT02512965						
	Observation vs SBRT vs SBRT +18F-DCFPyL		NCT02680587					
Small Molecule	Zoledronic acid (prevention)						NCT02622607	NCT02286830
	Docetaxel + zoledronic acid +/- apatinib						NCT03127319	
	Dose escalation of sirolimus + cyclophosphamide, methotrexate, zolendronic acid	NCT02517918						
	Dosing schedule of pamidronate or denosumab or zolendronate	NCT02721433						
	Zoledronic acid or densoumab +/- amorphous calcium carbonate		NCT02864784					
	Calcifediol + denosumab or zoledronic acid	NCT02274623						
	Cabozantinib		NCT01703065					
	Receptor tyrosine kinase inhibitor	NCT02219711						
	Selinexor (selective inhibitor of nuclear export)		NCT02215161					
	Docetaxel + clarithromycin vs cabazitaxel + clarithromycin		NCT03043989					
	Enzalutamide + LHRH analogue therapy vs bicalutamide + LHRH analogue therapy		NCT02058706					
	Copper + disulfram		NCT02963051					
	Palbociclib + tamoxifen			NCT02668666				
	Denosumab + enzalutamide +/- abiraterone and prednisone		NCT02758132					
Mab	Dosing schedule of denosumab	NCT02051218						
	Denosumab in patients with circulating tumor cells plus bone metastasis			NCT03070002				
	Denosumab + hormonal therapy			NCT01952054				
	Pembrolizumab		NCT02787005					
	Radium 223 +/- pembrolizumab		NCT03093428					
Radioisotopes	ADT +/- radium 223		NCT02582749					
	Hormonal therapy +/- radium 223			NCT02258464				
	EBRT +/- radium 223		NCT02484339					
	Radium 223		NCT03062254			NCT02390934	NCT02283749	
			NCT03002220					
			NCT02312960					
Cellular therapy	Genetically modified dendritic cells + cytokine induced killer cells						NCT02688686	
	Sipuleucel-T +/- radiation therapy		NCT01833208					
	Engineered autologous T cells + cyclophosphamide		NCT01140373					
	Dendritic cell based cryoimmunotherapy + cyclophosphamide +/- ipilimumab		NCT02423928					
	Sipuleucell-T +/- radium 223		NCT02463799					
HIFU	HIFU vs EBRT	NCT01091883						
	MRI guided HIFU	NCT03106675						
		NCT02718404						
		NCT00981578						
		NCT01833806						
		NCT02616016						
Surgery	Surgery +/- radiation therapy	NCT01428895						
	Radical Prostatectomy + ADT		NCT02454543					
	Intraoperative radiotherapy with kyphoplasty		NCT02480036					
	Kyphoplasty vs vertebroplasty	NCT02700308						
	Resection of primary breast tumor in stage IV patients			NCT02125630				
Other	Modified Polio virus		NCT03071328					
	Somatostatin		NCT02631616					
	Intermittant Fasting		NCT02710721					
	Bifunctional macromolecular poly-bisphosphonate		NCT02825628					
	Thermal ablation + steriotactic radiosurgery	NCT02713269						
	Pembrolizumab + pTVG-HP plasmid DNA vaccine		NCT02499835					
	Isometric resistance training	NCT02847754						
	Fentanyl transmucosal	NCT02426697						
	Fentynl intranasal	NCT03071744						
	Tanezumab (for pain)	NCT02609828						
	QOL with denosumab or bisphosphonates	NCT02839291						
	Cryoablation	NCT02511678						

Table 2: A review of current, open, interventional clinical trials for "bone metastasis" was performed using the clinical trials database at clinicaltrails.gov and 445 trials were found.

Relevant clinical trials on cancers involving prostate, breast, renal, thyroid, lung, multiple myeloma, or trials involving therapies for multiple types of cancers were included.

IV. CONCLUSIONS

Research into the molecular mechanisms of metastatic cancer, particularly bone metastatic cancer, has progressed rapidly in the past decade. Understanding the interactions and signaling processes at the bone microenvironment level has proven beneficial in advancing the field. Indeed, this knowledge has translated into the development and subsequent approval of several new targeted agents for patients with bone metastatic cancers. There are many promising therapeutic options in current pre-clinical development and in clinical trials that give hope for improved treatments and outcomes in patients with bone metastatic cancer.

V. REFERENCES

1. Kinch, M.S. An analysis of FDA-approved drugs for oncology. *Drug discovery today* 19, 1831-1835 (2014).

2. Siegel, R.L., Miller, K.D. & Jemal, A. Cancer statistics, 2016. *CA: a cancer journal for clinicians* 66, 7-30 (2016).

3. Hanahan, D. & Weinberg, R.A. Hallmarks of cancer: the next generation. *Cell* 144, 646-674 (2011).

4. Fidler, I.J. The pathogenesis of cancer metastasis: the 'seed and soil' hypothesis revisited. *Nature reviews. Cancer* 3, 453-458 (2003).

5. Ribatti, D., Mangialardi, G. & Vacca, A. Stephen Paget and the 'seed and soil' theory of metastatic dissemination. *Clinical and experimental medicine* 6, 145-149 (2006).

6. Thiery, J.P., Acloque, H., Huang, R.Y. & Nieto, M.A. Epithelial-mesenchymal transitions in development and disease. *Cell* 139, 871-890 (2009).

7. Duffy, M.J. The role of proteolytic enzymes in cancer invasion and metastasis. *Clinical & experimental metastasis* 10, 145-155 (1992).

8. Kessenbrock, K., Plaks, V. & Werb, Z. Matrix metalloproteinases: regulators of the tumor microenvironment. *Cell* 141, 52-67 (2010).

9. Gialeli, C., Theocharis, A.D. & Karamanos, N.K. Roles of matrix metalloproteinases in cancer progression and their pharmacological targeting. *The FEBS journal* 278, 16-27 (2011).

10. Wan, L., Pantel, K. & Kang, Y. Tumor metastasis: moving new biological insights into the clinic. *Nature medicine* 19, 1450-1464 (2013).

11. Weis, S.M. & Cheresh, D.A. Tumor angiogenesis: molecular pathways and therapeutic targets. *Nature medicine* 17, 1359-1370 (2011).

12. Reymond, N. et al. Cdc42 promotes transendothelial migration of cancer cells through beta1 integrin. *The Journal of cell biology* 199, 653-668 (2012).

13. Luzzi, K.J. et al. Multistep nature of metastatic inefficiency: dormancy of solitary cells after successful extravasation and limited survival of early micrometastases. *The American journal of pathology* 153, 865-873 (1998).

14. Paoli, P., Giannoni, E. & Chiarugi, P. Anoikis molecular pathways and its role in cancer progression. *Biochimica et biophysica acta* 1833, 3481-3498 (2013).

15. Douma, S. et al. Suppression of anoikis and induction of metastasis by the neurotrophic receptor TrkB. *Nature* 430, 1034-1039 (2004).

16. Weiskopf, K. et al. Engineered SIRPalpha variants as immunotherapeutic adjuvants to anticancer antibodies. *Science (New York, N.Y.)* 341, 88-91 (2013).

17. Maccauro, G. et al. Physiopathology of spine metastasis. *International journal of surgical oncology* 2011, 107969 (2011).

18. Gilbert, R.W., Kim, J.H. & Posner, J.B. Epidural spinal cord compression from metastatic tumor: diagnosis and treatment. *Annals of neurology* 3, 40-51 (1978).

19. Kakhki, V.R., Anvari, K., Sadeghi, R., Mahmoudian, A.S. & Torabian-Kakhki, M. Pattern and distribution of bone metastases in common malignant tumors. *Nuclear medicine review. Central & Eastern Europe* 16, 66-69 (2013).

20. Robinson, J.R., Newcomb, P.A., Hardikar, S., Cohen, S.A. & Phipps, A.I. Stage IV colorectal cancer primary site and patterns of distant metastasis. *Cancer epidemiology* 48, 92-95 (2017).

21. Sun, Y.X. et al. Expression of CXCR4 and CXCL12 (SDF-1) in human prostate cancers (PCa) in vivo. *Journal of cellular biochemistry* 89, 462-473 (2003).

22. Teicher, B.A. & Fricker, S.P. CXCL12 (SDF-1)/CXCR4 pathway in cancer. *Clinical cancer research : an official journal of the American Association for Cancer Research* 16, 2927-2931 (2010).

23. Sun, Y.X. et al. Expression and activation of alpha v beta 3 integrins by SDF-1/CXC12 increases the aggressiveness of prostate cancer cells. *The Prostate* 67, 61-73 (2007).

24. Greenbaum, A. et al. CXCL12 in early mesenchymal progenitors is required for haematopoietic stem-cell maintenance. *Nature* 495, 227-230 (2013).

25. Pitt, L.A. et al. CXCL12-Producing Vascular Endothelial Niches Control Acute T Cell Leukemia Maintenance. *Cancer cell* 27, 755-768 (2015).

26. Schneider, J.G., Amend, S.R. & Weilbaecher, K.N. Integrins and bone metastasis: integrating tumor cell and stromal cell interactions. *Bone* 48, 54-65 (2011).

27. Shiozawa, Y. et al. Annexin II/annexin II receptor axis regulates adhesion, migration, homing, and growth of prostate cancer. *Journal of cellular biochemistry* 105, 370-380 (2008).

28. Wang, H. et al. The osteogenic niche promotes early-stage bone colonization of disseminated breast cancer cells. *Cancer cell* 27, 193-210 (2015).

29. Zhang, X.H. et al. Latent bone metastasis in breast cancer tied to Src-dependent survival signals. *Cancer cell* 16, 67-78 (2009).

30. Mundy, G.R. Metastasis to bone: causes, consequences and therapeutic opportunities. *Nature reviews. Cancer* 2, 584-593 (2002).

31. Suva, L.J., Washam, C., Nicholas, R.W. & Griffin, R.J. Bone metastasis: mechanisms and therapeutic opportunities. *Nature reviews. Endocrinology* 7, 208-218 (2011).

32. Coleman, R.E. Skeletal complications of malignancy. *Cancer* 80, 1588-1594 (1997).

33. Roudier, M.P. et al. Histopathological assessment of prostate cancer bone osteoblastic metastases. *The Journal of urology* 180, 1154-1160 (2008).

34. Roodman, G.D. Cell biology of the osteoclast. *Experimental hematology* 27, 1229-1241 (1999).

35. Blair, H.C., Teitelbaum, S.L., Ghiselli, R. & Gluck, S. Osteoclastic bone resorption by a polarized vacuolar proton pump. *Science (New York, N.Y.)* 245, 855-857 (1989).

36. Kodama, H., Nose, M., Niida, S. & Yamasaki, A. Essential role of macrophage colony-stimulating factor in the osteoclast differentiation supported by stromal cells. *The Journal of experimental medicine* 173, 1291-1294 (1991).

37. Roodman, G.D. Mechanisms of bone metastasis. *The New England journal of medicine* 350, 1655-1664 (2004).

38. Ikeda, T., Kasai, M., Utsuyama, M. & Hirokawa, K. Determination of three isoforms of the receptor activator of nuclear factor-kappaB ligand and their differential expression in bone and thymus. *Endocrinology* 142, 1419-1426 (2001).

39. Simonet, W.S. et al. Osteoprotegerin: a novel secreted protein involved in the regulation of bone density. *Cell* 89, 309-319 (1997).

40. Min, H. et al. Osteoprotegerin reverses osteoporosis by inhibiting endosteal osteoclasts and prevents vascular calcification by blocking a process resembling osteoclastogenesis. *The Journal of experimental medicine* 192, 463-474 (2000).

41. Mizuno, A. et al. Severe osteoporosis in mice lacking osteoclastogenesis inhibitory factor/osteoprotegerin. *Biochemical and biophysical research communications* 247, 610-615 (1998).

42. Aubin, J.E. Bone stem cells. *Journal of cellular biochemistry. Supplement* 30-31, 73-82 (1998).

43. Wozney, J.M. Overview of bone morphogenetic proteins. *Spine* 27, S2-8 (2002).

44. Mundy, G.R. et al. Growth regulatory factors and bone. *Reviews in endocrine & metabolic disorders* 2, 105-115 (2001).

45. Yang, X. & Karsenty, G. Transcription factors in bone: developmental and pathological aspects. *Trends in molecular medicine* 8, 340-345 (2002).

46. Stein, G.S. & Lian, J.B. Molecular mechanisms mediating proliferation/differentiation interrelationships during progressive development of the osteoblast phenotype. *Endocrine reviews* 14, 424-442 (1993).

47. Bonewald, L.F. The amazing osteocyte. *Journal of bone and mineral research : the official journal of the American Society for Bone and Mineral Research* 26, 229-238 (2011).

48. David Roodman, G. & Silbermann, R. Mechanisms of osteolytic and osteoblastic skeletal lesions. *BoneKEy reports* 4, 753 (2015).

49. Sottnik, J.L., Dai, J., Zhang, H., Campbell, B. & Keller, E.T. Tumor-induced pressure in the bone microenvironment causes osteocytes to promote the growth of prostate cancer bone metastases. *Cancer research* 75, 2151-2158 (2015).

50. Giuliani, N. et al. Increased osteocyte death in multiple myeloma patients: role in myeloma-induced osteoclast formation. *Leukemia* 26, 1391-1401 (2012).

51. Delgado-Calle, J., Bellido, T. & Roodman, G.D. Role of osteocytes in multiple myeloma bone disease. *Current opinion in supportive and palliative care* 8, 407-413 (2014).

52. Glinsky, V.V. Intravascular cell-to-cell adhesive interactions and bone metastasis. *Cancer metastasis reviews* 25, 531-540 (2006).

53. Mastro, A.M., Gay, C.V. & Welch, D.R. The skeleton as a unique environment for breast cancer cells. *Clinical & experimental metastasis* 20, 275-284 (2003).

54. Raymaekers, K., Stegen, S., van Gastel, N. & Carmeliet, G. The vasculature: a vessel for bone metastasis. *BoneKEy reports* 4, 742 (2015).

55. Bussard, K.M., Gay, C.V. & Mastro, A.M. The bone microenvironment in metastasis; what is special about bone? *Cancer metastasis reviews* 27, 41-55 (2008).

56. Cook, L.M., Shay, G., Araujo, A. & Lynch, C.C. Integrating new discoveries into the "vicious cycle" paradigm of prostate to bone metastases. *Cancer metastasis reviews* 33, 511-525 (2014).

57. Colucci, S. et al. T cells support osteoclastogenesis in an in vitro model derived from human multiple myeloma bone disease: the role of the OPG/TRAIL interaction. *Blood* 104, 3722-3730 (2004).

58. Roato, I. et al. Mechanisms of spontaneous osteoclastogenesis in cancer with bone involvement. *FASEB journal : official publication of the Federation of American Societies for Experimental Biology* 19, 228-230 (2005).

59. D'Amico, L. & Roato, I. The Impact of Immune System in Regulating Bone Metastasis Formation by Osteotropic Tumors. *Journal of immunology research* 2015, 143526 (2015).

60. Kusmartsev, S., Nefedova, Y., Yoder, D. & Gabrilovich, D.I. Antigen-specific inhibition of CD8+ T cell response by immature myeloid cells in cancer is mediated by reactive oxygen species. *Journal of immunology (Baltimore, Md. : 1950)* 172, 989-999 (2004).

61. Liu, Y. et al. Nitric oxide-independent CTL suppression during tumor progression: association with arginase-producing (M2) myeloid cells. *Journal of immunology (Baltimore, Md. : 1950)* 170, 5064-5074 (2003).

62. Mazzoni, A. et al. Myeloid suppressor lines inhibit T cell responses by an NO-dependent mechanism. *Journal of immunology (Baltimore, Md. : 1950)* 168, 689-695 (2002).

63. Zhang, Q. et al. Interleukin-17 promotes formation and growth of prostate adenocarcinoma in mouse models. *Cancer research* 72, 2589-2599 (2012).

64. Bian, G. & Zhao, W.Y. IL-17, an important prognostic factor and potential therapeutic target for breast cancer? *European journal of immunology* 44, 604-605 (2014).

65. Morris, E.V. & Edwards, C.M. Bone Marrow Adipose Tissue: A New Player in Cancer Metastasis to Bone. *Frontiers in endocrinology* 7, 90 (2016).

66. Herroon, M.K. et al. Bone marrow adipocytes promote tumor growth in bone via FABP4-dependent mechanisms. *Oncotarget* 4, 2108-2123 (2013).

67. Templeton, Z.S. et al. Breast Cancer Cell Colonization of the Human Bone Marrow Adipose Tissue Niche. *Neoplasia (New York, N.Y.)* 17, 849-861 (2015).

68. Caers, J. et al. Neighboring adipocytes participate in the bone marrow microenvironment of multiple myeloma cells. *Leukemia* 21, 1580-1584 (2007).

69. Jourdan, M. et al. Tumor necrosis factor is a survival and proliferation factor for human myeloma cells. *European cytokine network* 10, 65-70 (1999).

70. Gado, K., Domjan, G., Hegyesi, H. & Falus, A. Role of INTERLEUKIN-6 in the pathogenesis of multiple myeloma. *Cell biology international* 24, 195-209 (2000).

71. Valta, M.P. et al. FGF-8 is involved in bone metastasis of prostate cancer. *International journal of cancer* 123, 22-31 (2008).

72. Morrissey, C., Brown, L.G., Pitts, T.E., Vessella, R.L. & Corey, E. Bone morphogenetic protein 7 is expressed in prostate cancer metastases and its effects on prostate tumor cells depend on cell phenotype and the tumor microenvironment. *Neoplasia (New York, N.Y.)* 12, 192-205 (2010).

73. Kwabi-Addo, B., Ozen, M. & Ittmann, M. The role of fibroblast growth factors and their receptors in prostate cancer. *Endocrine-related cancer* 11, 709-724 (2004).

74. Mohan, S. & Baylink, D.J. Bone growth factors. *Clinical orthopaedics and related research*, 30-48 (1991).

75. Cole, L.E., Vargo-Gogola, T. & Roeder, R.K. Targeted delivery to bone and mineral deposits using bisphosphonate ligands. *Advanced drug delivery reviews* 99, 12-27 (2016).

76. Glorieux, F.H. Experience with bisphosphonates in osteogenesis imperfecta. *Pediatrics* 119 Suppl 2, S163-165 (2007).

77. Drake, M.T., Clarke, B.L. & Khosla, S. Bisphosphonates: mechanism of action and role in clinical practice. *Mayo Clinic proceedings* 83, 1032-1045 (2008).

78. Watts, N.B. & Diab, D.L. Long-term use of bisphosphonates in osteoporosis. *The Journal of clinical endocrinology and metabolism* 95, 1555-1565 (2010).

79. Kim, S.M. et al. Atypical Complete Femoral Fractures Associated with Bisphosphonate Use or Not Associated with Bisphosphonate Use: Is There a Difference? *BioMed research international* 2016, 4753170 (2016).

80. Lewiecki, E.M. Safety of long-term bisphosphonate therapy for the management of osteoporosis. *Drugs* 71, 791-814 (2011).

81. Nadar, R.A. et al. Bisphosphonate-Functionalized Imaging Agents, Anti-Tumor Agents and Nanocarriers for Treatment of Bone Cancer. *Advanced healthcare materials* (2017).

82. Iafisco, M. et al. Adsorption and conformational change of myoglobin on biomimetic hydroxyapatite nanocrystals functionalized with alendronate. *Langmuir : the ACS journal of surfaces and colloids* 24, 4924-4930 (2008).

83. van Beek, E., Hoekstra, M., van de Ruit, M., Lowik, C. & Papapoulos, S. Structural requirements for bisphosphonate actions in vitro. *Journal of bone and mineral research : the official journal of the American Society for Bone and Mineral Research* 9, 1875-1882 (1994).

84. Ebetino, F.H. et al. The relationship between the chemistry and biological activity of the bisphosphonates. *Bone* 49, 20-33 (2011).

85. Saad, F. et al. Long-term efficacy of zoledronic acid for the prevention of skeletal complications in patients with metastatic hormone-refractory prostate cancer. *Journal of the National Cancer Institute* 96, 879-882 (2004).

86. Coxon, F.P., Thompson, K. & Rogers, M.J. Recent advances in understanding the mechanism of action of bisphosphonates. *Current opinion in pharmacology* 6, 307-312 (2006).

87. Caraglia, M. et al. Emerging anti-cancer molecular mechanisms of aminobisphosphonates. *Endocrine-related cancer* 13, 7-26 (2006).

88. Fizazi, K. et al. Denosumab versus zoledronic acid for treatment of bone metastases in men with castration-resistant prostate cancer: a randomised, double-blind study. *Lancet (London, England)* 377, 813-822 (2011).

89. Lacey, D.L. et al. Bench to bedside: elucidation of the OPG-RANK-RANKL pathway and the development of denosumab. *Nature reviews. Drug discovery* 11, 401-419 (2012).

90. Kostenuik, P.J. et al. Denosumab, a fully human monoclonal antibody to RANKL, inhibits bone resorption and increases BMD in knock-in mice that express chimeric (murine/human) RANKL. *Journal of bone and mineral research : the official journal of the American Society for Bone and Mineral Research* 24, 182-195 (2009).

91. Lacey, D.L. et al. Osteoprotegerin ligand is a cytokine that regulates osteoclast differentiation and activation. *Cell* 93, 165-176 (1998).

92. Brown, J.M. et al. Osteoprotegerin and rank ligand expression in prostate cancer. *Urology* 57, 611-616 (2001).

93. Giuliani, N. et al. Human myeloma cells stimulate the receptor activator of nuclear factor-kappa B ligand (RANKL) in T lymphocytes: a potential role in multiple myeloma bone disease. *Blood* 100, 4615-4621 (2002).

94. Luger, N.M. et al. Osteoprotegerin diminishes advanced bone cancer pain. *Cancer research* 61, 4038-4047 (2001).

95. Roudier, M.P., Bain, S.D. & Dougall, W.C. Effects of the RANKL inhibitor, osteoprotegerin, on the pain and histopathology of bone cancer in rats. *Clinical & experimental metastasis* 23, 167-175 (2006).

96. Oyajobi, B.O. et al. Therapeutic efficacy of a soluble receptor activator of nuclear factor kappaB-IgG Fc fusion protein in suppressing bone resorption and hypercalcemia in a model of humoral hypercalcemia of malignancy. *Cancer research* 61, 2572-2578 (2001).

97. Wong, M. & Pavlakis, N. Optimal management of bone metastases in breast cancer patients. *Breast cancer (Dove Medical Press)* 3, 35-60 (2011).

98. Vengalil, S., O'Sullivan, J.M. & Parker, C.C. Use of radionuclides in metastatic prostate cancer: pain relief and beyond. *Current opinion in supportive and palliative care* 6, 310-315 (2012).

99. Brady, D., Parker, C.C. & O'Sullivan, J.M. Bone-targeting radiopharmaceuticals including radium-223. *Cancer journal (Sudbury, Mass.)* 19, 71-78 (2013).

100. Longo, J., Lutz, S. & Johnstone, C. Samarium-153-ethylene diamine tetramethylene phosphonate, a beta-emitting bone-targeted radiopharmaceutical, useful for patients with osteoblastic bone metastases. *Cancer management and research* 5, 235-242 (2013).

101. Body, J.J., Casimiro, S. & Costa, L. Targeting bone metastases in prostate cancer: improving clinical outcome. *Nature reviews. Urology* 12, 340-356 (2015).

102. Parker, C. et al. Alpha emitter radium-223 and survival in metastatic prostate cancer. *The New England journal of medicine* 369, 213-223 (2013).

103. Jadvar, H. & Quinn, D.I. Targeted alpha-particle therapy of bone metastases in prostate cancer. *Clinical nuclear medicine* 38, 966-971 (2013).

104. Autio, K.A. & Morris, M.J. Targeting bone physiology for the treatment of metastatic prostate cancer. *Clinical advances in hematology & oncology : H&O* 11, 134-143 (2013).

105. Nilsson, S. et al. Bone-targeted radium-223 in symptomatic, hormone-refractory prostate cancer: a randomised, multicentre, placebo-controlled phase II study. *The Lancet. Oncology* 8, 587-594 (2007).

106. Huggins, C. & Hodges, C.V. Studies on prostatic cancer: I. The effect of castration, of estrogen and of androgen injection on serum phosphatases in metastatic carcinoma of the prostate. 1941. *The Journal of urology* 168, 9-12 (2002).

107. Zhang, Q. & Gray, P.J. From bench to bedside: bipolar androgen therapy in a pilot clinical study. *Asian journal of andrology* 17, 767-768 (2015).

108. Seruga, B., Ocana, A. & Tannock, I.F. Drug resistance in metastatic castration-resistant prostate cancer. *Nature reviews. Clinical oncology* 8, 12-23 (2011).

109. Bubendorf, L. et al. Metastatic patterns of prostate cancer: an autopsy study of 1,589 patients. *Human pathology* 31, 578-583 (2000).

110. Huang, X., Chau, C.H. & Figg, W.D. Challenges to improved therapeutics for metastatic castrate resistant prostate cancer: from recent successes and failures. *Journal of hematology & oncology* 5, 35 (2012).

111. Reid, A.H., Attard, G., Barrie, E. & de Bono, J.S. CYP17 inhibition as a hormonal strategy for prostate cancer. *Nature clinical practice. Urology* 5, 610-620 (2008).

112. El-Amm, J., Patel, N., Freeman, A. & Aragon-Ching, J.B. Metastatic castration-resistant prostate cancer: critical review of enzalutamide. *Clinical Medicine Insights. Oncology* 7, 235-245 (2013).

113. Mantalaris, A. et al. Localization of androgen receptor expression in human bone marrow. *The Journal of pathology* 193, 361-366 (2001).

114. Tannock, I.F. et al. Docetaxel plus prednisone or mitoxantrone plus prednisone for advanced prostate cancer. *The New England journal of medicine* 351, 1502-1512 (2004).

115. James, N.D. et al. Addition of docetaxel, zoledronic acid, or both to first-line long-term hormone therapy in prostate cancer (STAMPEDE): survival results from an adaptive, multiarm, multistage, platform randomised controlled trial. *Lancet (London, England)* 387, 1163-1177 (2016).

116. de Bono, J.S. et al. Prednisone plus cabazitaxel or mitoxantrone for metastatic castration-resistant prostate cancer progressing after docetaxel treatment: a randomised open-label trial. *Lancet (London, England)* 376, 1147-1154 (2010).

117. Li, B.T., Wong, M.H. & Pavlakis, N. Treatment and Prevention of Bone Metastases from Breast Cancer: A Comprehensive Review of Evidence for Clinical Practice. *Journal of clinical medicine* 3, 1-24 (2014).

118. Beslija, S. et al. Third consensus on medical treatment of metastatic breast cancer. *Annals of oncology : official journal of the European Society for Medical Oncology* 20, 1771-1785 (2009).

119. Kantoff, P.W. et al. Sipuleucel-T immunotherapy for castration-resistant prostate cancer. *The New England journal of medicine* 363, 411-422 (2010).

120. Slovin, S.F. Immunotherapy in metastatic prostate cancer. *Indian journal of urology : IJU : journal of the Urological Society of India* 32, 271-276 (2016).

121. Stephenson, M.B., Glaenzer, B. & Malamis, A. Percutaneous Minimally Invasive Techniques in the Treatment of Spinal Metastases. *Current treatment options in oncology* 17, 56 (2016).

122. Dohm, M., Black, C.M., Dacre, A., Tillman, J.B. & Fueredi, G. A randomized trial comparing balloon kyphoplasty and vertebroplasty for vertebral compression fractures due to osteoporosis. *AJNR. American journal of neuroradiology* 35, 2227-2236 (2014).

123. Mannion, R.J. & Woolf, C.J. Pain mechanisms and management: a central perspective. *The Clinical journal of pain* 16, S144-156 (2000).

124. Wu, J.S., Wong, R., Johnston, M., Bezjak, A. & Whelan, T. Meta-analysis of dose-fractionation radiotherapy trials for the palliation of painful bone metastases. *International journal of radiation oncology, biology, physics* 55, 594-605 (2003).

125. Sze, W.M., Shelley, M., Held, I. & Mason, M. Palliation of metastatic bone pain: single fraction versus multifraction radiotherapy - a systematic review of the randomised trials. *The Cochrane database of systematic reviews*, Cd004721 (2004).

126. Chow, E. et al. Update on the systematic review of palliative radiotherapy trials for bone metastases. *Clinical oncology (Royal College of Radiologists (Great Britain))* 24, 112-124 (2012).

127. Horwich, A., Parker, C., de Reijke, T. & Kataja, V. Prostate cancer: ESMO Clinical Practice Guidelines for diagnosis, treatment and follow-up. *Annals of oncology : official journal of the European Society for Medical Oncology* 24 Suppl 6, vi106-114 (2013).

128. Tomita, K. et al. Surgical strategy for spinal metastases. *Spine* 26, 298-306 (2001).

129. Toliusis, V., Kalesinskas, R.J., Kiudelis, M., Maleckas, A. & Griksas, M. Surgical treatment of metastatic tumors of the femur. *Medicina (Kaunas, Lithuania)* 46, 323-328 (2010).

130. Ward, W.G., Holsenbeck, S., Dorey, F.J., Spang, J. & Howe, D. Metastatic disease of the femur: surgical treatment. *Clinical orthopaedics and related research*, S230-244 (2003).

CHAPTER II

BONE TARGETED CABAZITAXEL NANOPARTICLES FOR METASTATIC PROSTATE CANCER SKELETAL LESIONS AND PAIN

I. ABSTRACT

Aims: The aim of this study was to develop a novel cabazitaxel bone targeted nanoparticle system for improved drug delivery to the bone microenvironment.

Materials and Methods: Nanoparticles were developed using PLGA and cabazitaxel as the core with amino-bisphosphonate surface conjugation. Optimization of nanoparticle physiochemical properties, *in vitro* evaluation in prostate cancer cell lines, and *in vivo* testing in an intraosseous model of metastatic prostate cancer was performed.

Results: This bone targeted cabazitaxel nanocarrier system showed significant reduction in tumor burden, while at the same time maintaining bone structure integrity and reducing pain in the mouse tumor limb.

Conclusions: This bone microenvironment targeted nanoparticle system and clinically relevant approach of evaluation represents a promising advancement for treating bone metastatic cancer.

II. INTRODUCTION

Despite improved overall survival in cancer patients over the past 50 years, limited advances have been made in treating patients with metastatic cancers. Multiple types of cancers demonstrate the unique ability to specifically home to the bone. Among these, prostate cancer exhibits increased capacity to create bone specific lesions with high frequency[1]. Once bone localization takes place, treatment regimens are inadequate and overall survival is poor[2]. Nearly all patients who die from prostate cancer will have skeletal involvement[1]. These bone metastases often cause debilitating and life threatening problems including: uncontrollable pain, hypercalcemia, broken bones, spinal cord compression, and the inability to perform activities of daily living.

Several barriers exist to developing optimal therapy for bone metastatic prostate cancer. At the molecular level, receptor activator for nuclear factor κB (RANK), its ligand (RANKL), osteoprotegerin (OPG) and other signaling molecules are secreted by osteoclasts, osteoblasts, and cancer cells. This creates a vicious cycle of bone turnover and increased proliferation of cancer cells[3]. Some therapeutic strategies direct treatment at the bone with drugs such as denosumab or bisphosphonates. These are effective at delaying the time to fractures and providing improvement in pain[4, 5]. Other treatments for bone metastatic prostate cancer utilize androgen deprivation or cytotoxic agents[6, 7]. These are effective to a point. However, prostate cancer cells will inevitably become resistant to androgen deprivation and cytotoxic agents have known toxicities which limit administration. Another strategy involves targeting bone metastasis

with alpha particles using radium-223. This provides some improved overall survival[8] but may have logistical and shelf life limitations [9].

One of the current discussions revolving around optimal therapy of bone metastasis is which target or targets are most important[10]. We argue that focusing on treatment of cancer cells is most important because they are the primary insult to the system. In a previous study, we have utilized two chemotherapeutic agents, bortezomib and curcumin, which were effective in a mouse model of bone metastatic breast cancer[11].

Another challenge to effective treatment of bone metastasis is observed at the level of the tumor and the bone structure. The hydroxyapatite structure of the bone contains growth factors such as: insulin like growth factors I and II, bone morphogenetic proteins, platelet-derived growth factor, transforming growth factor-beta, and fibroblast growth factor[12]. These factors are released as lesions develop and cause further growth and proliferation of the tumor cells. Additionally, drugs may not adequately penetrate the tumor and thus are delivered to the bone at suboptimal therapeutic levels.

Finally, *in vivo* functional assessment of clinically relevant parameters during the preclinical testing phase is often overlooked. However, there are some groups who have investigated functional assessment in the preclinical development of bone targeted therapies for bone metastatic cancer. One recent example of a novel liposomal formulation demonstrated pain

improvement in a bone metastatic model of prostate cancer after treatment with RGD peptide conjugated cisplatin liposomes[13]. Strategies like this are important because once these bone metastatic lesions have become established, severe and debilitating bone pain is a challenge to manage as performance status decreases. More research emphasis should be placed on validating pain assessment assays while testing pre-clinical therapies for bone metastatic cancers.

In this manuscript, we describe the engineering and validation experiments of a novel cabazitaxel encapsulated bone microenvironment targeted nanoparticle system. Bone targeting was achieved by utilizing an amino-bisphosphonate molecule attached to the surface of polymeric nanoparticles. Poly (D,L-lactic-co-glycolic acid) (PLGA) was chosen as the core of the nanoparticle for its biocompatibility and ability for controlled release of cargo. We have optimized the chemical and physical characteristics of this system and have tested the nanoformulation in both *in vitro* and *in vivo* models of metastatic prostate cancer. We have tested the efficacy in an intraosseous model of bone metastatic prostate cancer while monitoring bone structure. Finally, we have utilized behavior assays to measure pain response after treatment with the bone targeted nanoparticles.

III. RESULTS

Formulation and physicochemical properties of nanoparticles

Nanoparticles were successfully synthesized by a double emulsion solvent evaporation technique in which cabazitaxel was encapsulated inside the nanoparticles and alendronate (ALN) was attached to the outside of the nanoparticles. Nanoparticles with aldendronate decoration will be

referred to as targeted NP. Nanoparticles that have no alendronate (prepared similar to targeted NP except the linkers neutralized with Tris buffer incubation) will be referred to as non-targeted NP. The optimal drug concentration was decided at 5% cabazitaxel to PLGA (w/w). This starting concentration yielded an encapsulation efficiency of 55.87% and drug loading of 3.74% (Figure 2). Thus, for all further experiments 5% was used as the drug to polymer ratio for formulating the NPs. Next, the hydrodynamic diameter of the non-targeted NP (Mean=214.2 ± S.D. 2.27) and the targeted NP (Mean=236.8 ± S.D. 1.19) was measured by dynamic light scattering. The polydispersity was also calculated for the non-targeted NP (Mean= 0.114 ± SEM 0.012) and the targeted NP (Mean= 0.121 ± SEM 0.003) (Figure 1b). Nanoparticles were imaged with scanning electron microscopy (SEM) and shown to be of spherical shape with textured surface details as seen in (Figure 2 e-f). No significant morphological differences were noted between the targeted and non-targeted NP.

The release kinetics of cabazitaxel from the nanoparticle were investigated *in vitro*. The cabazitaxel exhibited a strong initial burst phase release for 7.5 hours with approximately 80% of the cabazitaxel being released from the nanoparticle during this time. This initial period was followed by a longer sustained release of the remaining cabazitaxel up to 98% cumulative drug released at 72 hours (Figure 2d).

a

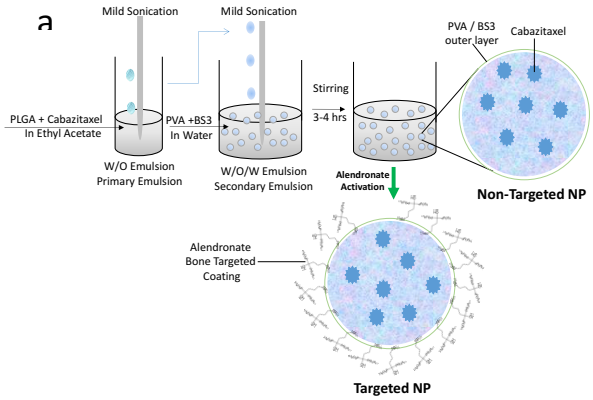

b

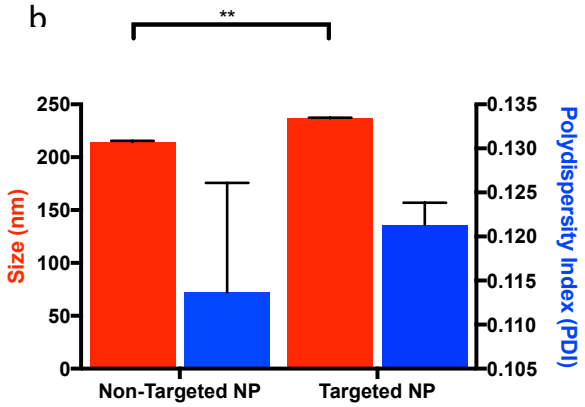

c

Initial Cabazitaxel in NP Formulation (%)	Encapsulation Efficiency (%)	Drug Loading (%)
0.5	37.7	0.3
1.0	27.9	0.4
2.0	45.5	1.1
3.0	48.8	1.6
4.0	55.3	2.5
5.0	55.8	3.7

d

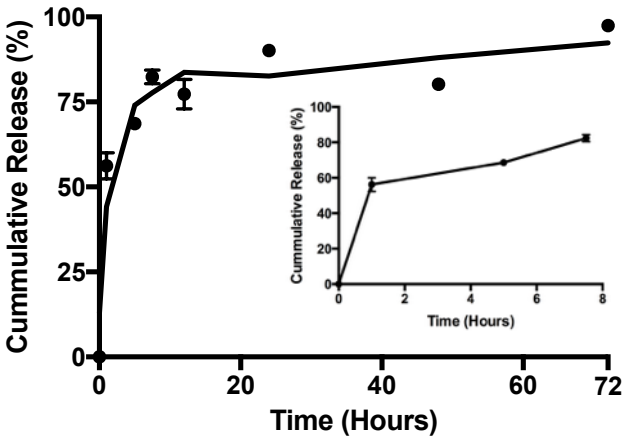

e

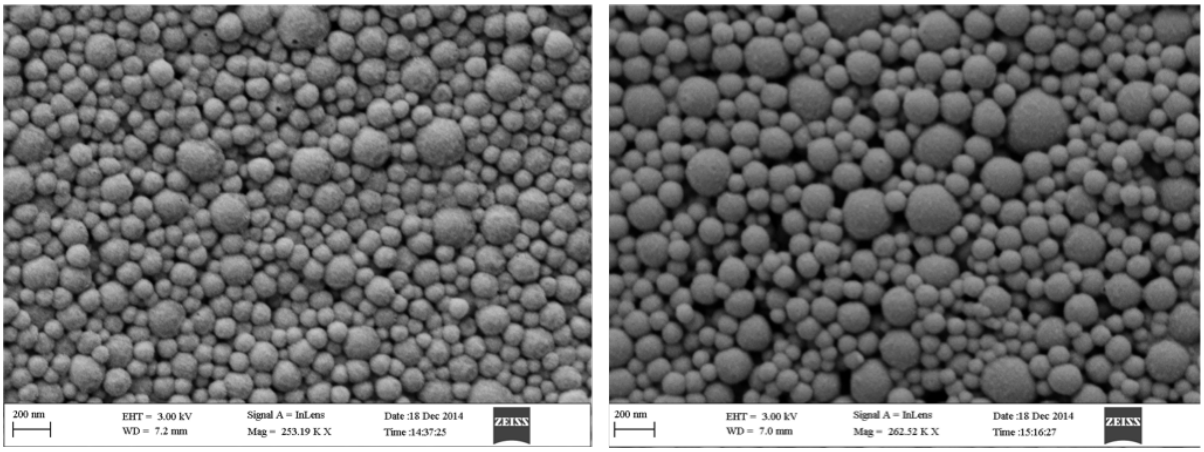

Non-Targeted NP

Targeted NP

Figure 2: Nanoparticle physical characterization. (a) Schematic illustrating nanoparticle (NP) synthesis through water-in-oil-in-water double emulsion solvent evaporation technique followed by activation of nanoparticle with alendronate for bone targeting. **(b)** Size (red) and polydispersity index **(blue)** of non-targeted NP versus targeted NP. Mean ± SEM (n=3). ** P value < 0.005. **(c)** Mean encapsulation efficiency of drug within nanoparticle at various initial concentrations of cabazitaxel in the NP formulation as a percentage of total weight of polymer and drug. **(d)** Release kinetics of cabazitaxel from NP at time points (1, 5, 8, 12, 24, 72 hours). (Inset) magnification of time points (1, 5, 8 hours). Mean ± SEM (n=3). **(e)** Scanning electron microscopy (SEM) images of non-targeted NP and targeted NP.

In 2D cellular viability assays (MTT assay), our results indicated that C4-2B cells were more sensitive to the treatments (free cabazitaxel, the non-targeted NP and the targeted NP) as compared to PC-3 cells. Additionally, the nanoparticle formulations compared to the free drug exhibited similar cell viability in the assays. No significant differences were observed between the non-targeted NP and the targeted NP groups. This was expected because the targeted mechanism is against the bone and not against the cancer cell per se and thus the targeting is not being tested in this assay. Finally, all treatment groups in both cell lines exhibited decreased survival at the longer treatment time points (Figure 3).

C4-2B cells were used to construct 3-D spheroids as an *in vitro* model of prostate cancer. After treatment exposure, calcein AM was added to spheroids and fluorescence integrated density (FID) was used to quantify the difference in viability between treatment groups. Consistent with the results from the 2D cell viability assay, there was not a significant difference between spheroids treated with free drug and those treated with the equivalent dose of targeted NP. This suggests the possibility that the targeted NP provides comparable tumor inhibition through penetration of tumor spheroids. Additionally, the targeted NP group with no cabazitaxel loaded in it had the same viability as the saline treatment (Control) spheroid group which demonstrates that the targeted-NP without the cabazitaxel doesn't have any impact on cell viability (Figure 3b-c).

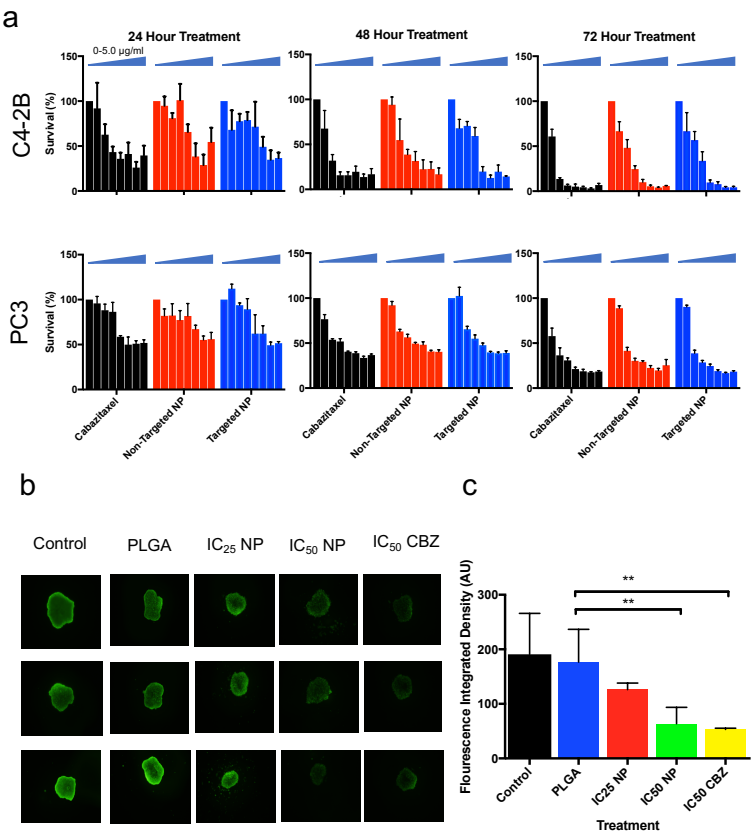

Figure 3: Nanoparticle *in vitro* studies. (a) Dose and time dependent MTT growth inhibition assay of treatments in C4-2B (top row) and PC3 (bottom row) cell lines. Each cell line was treated for 24, 48, or 72 hours with either cabazitaxel (black), non-targeted NP (red), or targeted NP (blue) at increasing concentrations (0.0000, 0.0005, 0.0050, 0.0100, 0.0250, 0.0500, 0.5000, 5.0000 µg/ml). Mean ± SEM (n=3). **(b)** 3D Tumor Spheroid viability assay. Representative prostate spheroids were treated for 72 hours with either DMSO as control vehicle (control), blank PLGA NP (PLGA), IC_{25} of cabazitaxel loaded Targeted NP (IC_{25} NP), IC_{50} of cabazitaxel (CBZ) loaded Targeted NP (IC_{50} NP), or the equivalent drug concentration of free cabazitaxel (IC_{50} Cab). After 72 hours, spheroids were treated with calcien AM to determine spheroid

viability. **(c)** Fluorescent integrated density quantification of prostate spheroids. Mean ± SEM (n=4). ** P value < 0.005.

Targeted NPs have bone affinity

We investigated whether the targeted NP had the ability to bind to bone *ex vivo* by performing a bone binding assay. This assay showed a nearly 4-fold increase of targeted NP binding to bone compared to non-targeted NP at the 6 hour time point. The difference in binding of the targeted NP to the non-targeted NP was also increased to approximately 5-fold and 8-fold in the subsequent 24 and 72 hours respectively (Figure 4 a-b).

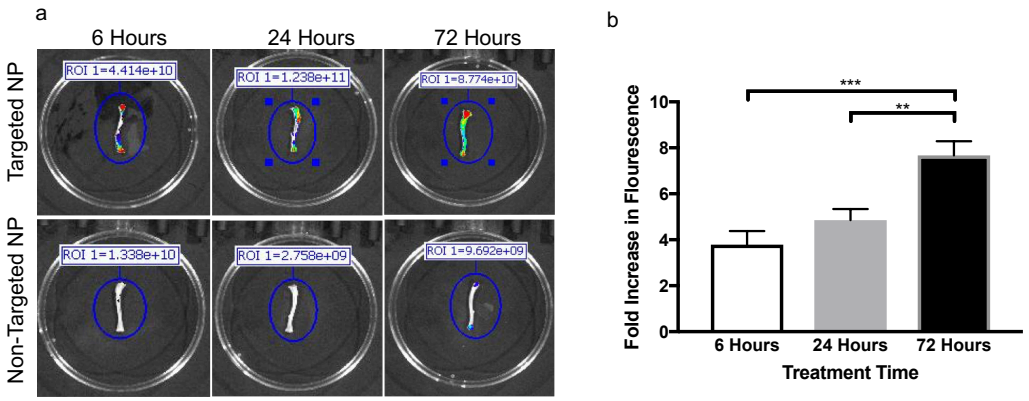

Figure 4: *Ex-vivo* bone binding of nanoparticles. **(a)** Representative imaging with fluorescent overlay of mouse femurs after being incubated with either targeted NP tagged with fluorescent dye (top row) or non-targeted NP tagged with fluorescent dye (bottom row). Bones were incubated with NP for either 6, 24, or 72 hours. **(b)** Quantification of fold increase in fluorescent signal between targeted NP and non-targeted NP at various time points. Mean ± SEM (n=3). ** P value < 0.005. *** P value < 0.0005.

Targeted NPs are effective at reducing tumor burden and maintaining bone structure

To determine the anti-tumor efficacy of the targeted-NP we used an intraosseous model of prostate cancer. Male athymic mice were injected intratibially with PC-3-luciferase cells. Tumors were allowed to develop for 7 days. At 7 days, mice were randomized into treatment groups based on bioluminescence signal of the PC-3 luciferase cells so that there was no statistically significant difference in starting tumor volume between groups. Mice were treated with intravenous injection weekly with one of the following treatments: 1.) Saline, 2.) Cabazitaxel, 3.) Non-targeted NP, or 4.) Targeted NP. After one month of treatment, mice were euthanized and lower limbs were isolated by excision at the knee and ankle joints and skin removal. Tumor burden was measured with bioluminescence signal as well as limb weight at termination of the experiment. When measuring tumor weight, both the targeted-NP and non-targeted NP groups showed a significant reduction in tumor compared to control treatment (P value= 0.0001). The difference between the cabazitaxel group and the saline treated group was also significant but to a lesser degree (P value = 0.002). When comparing the cabazitaxel treatment to the nanoparticle treatment groups, only the targeted NP treatment had a significant reduction in limb weight (P value= 0.0447) (Figure 5 d). When comparing the overall change in bioluminescence from the initial time point to the final week of the experiment, we observed a significant reduction in bioluminescence signal in the cabazitaxel group compared to the saline group (P value= 0.0283) and an even more significant different between the targeted and the non-targeted NP group (P values= 0.0027 and 0.0019, respectively) (Figure 5 e).

We also investigated whether the targeted-NP impacts the physical structure of the bone through analysis of x-ray imaging in the tumor burdened limb prior to limb excision. Of note, we found that treatment with the targeted NP provided protection from bone lesions in all the mice imaged while those mice treated with the non-targeted NP showed bone lesions in 33% of the mice. Further, every mouse in the saline and cabazitaxel groups developed bone lesions (Figure 5 c).

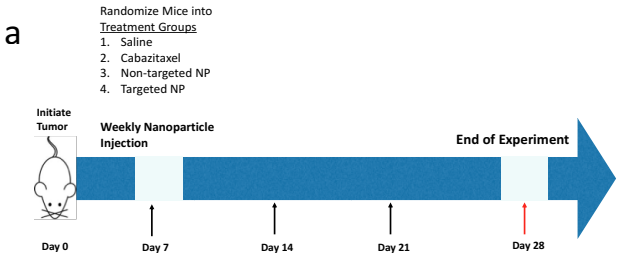
a
Randomize Mice into
Treatment Groups
1. Saline
2. Cabazitaxel
3. Non-targeted NP
4. Targeted NP
Initiate Tumor
Weekly Nanoparticle Injection
End of Experiment
Day 0
Day 7
Day 14
Day 21
Day 28

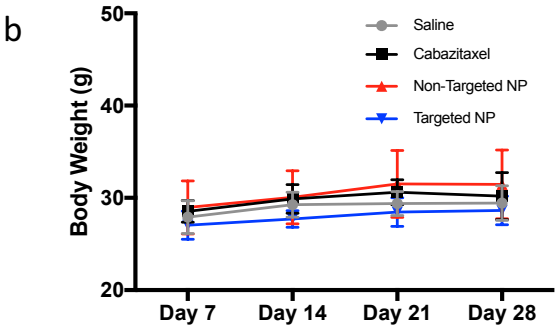
b
Body Weight (g)
50
40
30
20
Saline
Cabazitaxel
Non-Targeted NP
Targeted NP
Day 7
Day 14
Day 21
Day 28

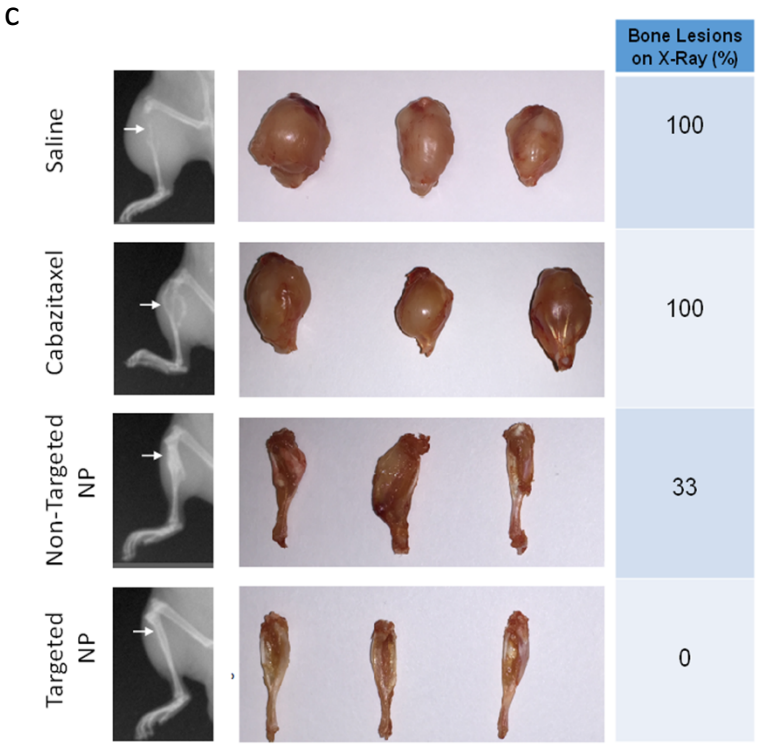
c
Bone Lesions on X-Ray (%)
Saline
100
Cabazitaxel
100
Non-Targeted NP
33
Targeted NP
0

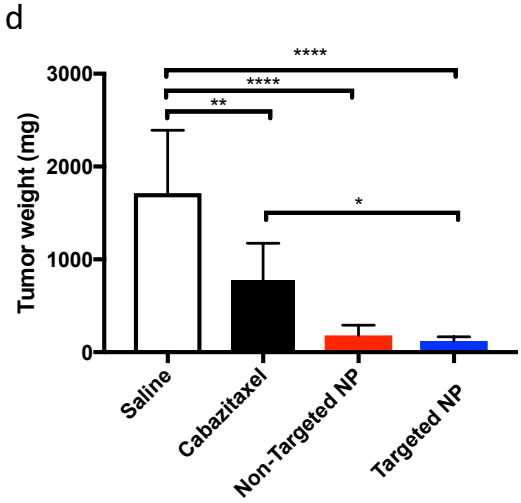
d
Tumor weight (mg)
3000
2000
1000
0
****
****
**
*
Saline
Cabazitaxel
Non-Targeted NP
Targeted NP

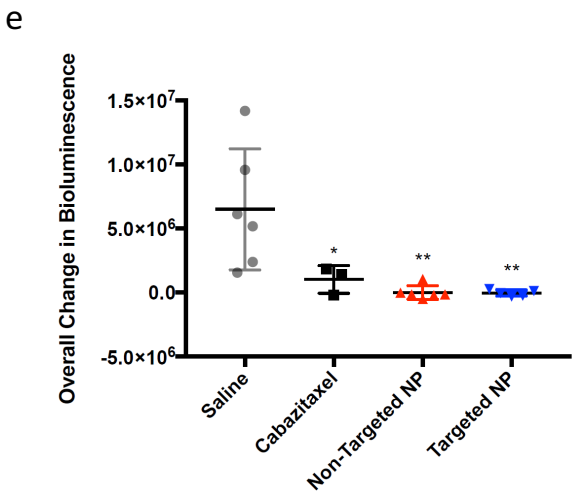
e
Overall Change in Bioluminescence
1.5×10^7
1.0×10^7
5.0×10^6
0.0
-5.0×10^6
*
**
**
Saline
Cabazitaxel
Non-Targeted NP
Targeted NP

Figure 5: *In vivo* tumor efficacy study. (a) Schematic representing design of efficacy study. Tumors were initiated by injecting PC3 cells intraosseously in the tibia of mice. After 7 days mice were randomized into treatment groups based on bioluminescence signal to assure there were no significant differences in initial intraosseous tumor burden. Mice were injected via tail vein with either saline, cabazitaxel, non-targeted NP or targeted NP once every 7 days for 28 days. Mice were sacrificed at 28 days. **(b)** Mouse body weight measurement throughout experiment didn't demonstrate a significant difference between treatments **(c)** (Middle) Representative images of excised tumors at end of experiment. (Left) Representative x-ray images of mice bone structure at end of experiment. Arrow shows tibia with bone lesion (saline, cabazitaxel, non-targeted NP) or intact bone (targeted NP). (Right) Percentage of mice in each group with bone lesions as measured by X-ray. **(d)** Final tumor weight of intratibial tumors after sacrifice. Mean ± SEM (n=6 in all groups except targeted NP where n=5). **(e)** Change in bioluminescence signal from day 7 to day 28. Mean ± SEM (n=6 in saline and non-targeted groups, n=5 in targeted NP, n=3 for cabazitaxel group). **** P value < 0.0001, ** P value< 0.005, * P value< 0.05 using Dunnett's multiple comparisons test.

Targeted NPs improve pain response

To evaluate functional status, we assessed both pain via the von Frey assay and gait via paw print analysis. In the von Frey assay the targeted NP group significantly reduced the relative response to the filament in the tumor burdened limb (P value= 0.026), whereas non-targeted NP and cabazitaxel treatments did not show a statistically significant relative reduction in response (Figure 6). Gait parameters that were measured included: stance width between opposite limbs,

left limb stride distance, and right limb stride distance. There were no significant differences between any treatment groups in gait parameters (results not shown).

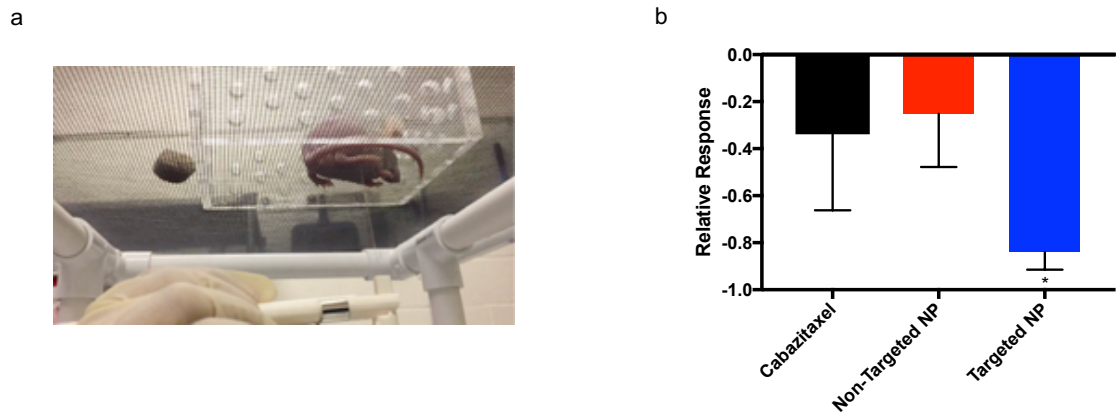

Figure 6: Animal behavioral von Frey monofilament assay. (a) Representation of experimental setup (video demonstration in supplemental. When mouse feels painful filament stimulus, it will lift limb in response). **(b)** Relative response of treatment groups as normalized to saline treatment group response (n=6). There was a significant decrease in relative response to stimulus between saline and targeted NP groups when the untransformed data of saline and targeted NP were compared using ANOVA. Mean ± SEM (n=6 in non-targeted NP group, n=5 in saline and targeted groups, n=2 in cabazitaxel group). * P value < 0.05.

IV. DISCUSSION

Our overall objective was to engineer an effective treatment for bone metastatic prostate cancer and test this therapy in a manner that can address some of the current challenges in treating bone metastatic prostate cancer. We have designed this targeted nanoparticle system with attention to

addressing challenges at the molecular level, the tumor microenvironment and bone structure level, as well as the functional level.

Cabazitaxel was chosen as the cytotoxic agent for this nanoparticle system, which was successfully loaded into the nanoparticle with an adequate encapsulation efficacy of 55.8 % at a drug-polymer ratio of 5% (w/w) (Figure 2 c). Cabazitaxel was chosen because it is a 3rd generation microtubule inhibitor that was approved by the FDA in 2010 for treating hormone-refractory metastatic prostate cancer that has progressed despite treatment with docetaxel. Unlike the older taxane drugs, paclitaxel and docetaxel, cabaxitaxel exhibits much lower substrate affinity for the ATP-dependent drug efflux pump glycoprotein (P-gp) that is commonly up-regulated in metastatic and chemotherapy resistant cancers[14],[15]. However, cabazitaxel does exhibit some toxicities that include: neuropathies, myelosuppression, febrile neutropenia, diarrhea, fatigue, and asthenia among others[16]. The goal of formulating cabazitaxel in a targeted NP is to reduce the dosage of cabazitaxel and hence reduce its associated side effects.

There is disparity in the literature as to the size nanoparticles should be made in order to provide best delivery to the tumor but most reports agree that a size less than the 200-250 nm range is optimal[12]. We have manufactured the nanoparticles for this project to be within this size range with mean size of 236 nm after coating with alendronate (Figure 2 b). Nanoparticles in this range can utilize passive targeting through the enhanced permeability and retention (EPR) phenomenon while achieving active targeting with the alendronate coating.

In the *in vitro* cell viability studies, we found that addition of the targeting component, alendronate, to the targeted NPs didn't increase growth inhibition in either the C4-2B or PC3 cell line. This was expected and similar results were seen in the 3D spheroid experiments, likely because of two reasons: 1.) the targeting mechanism of the alendronate moiety is against the hydroxyapatite structure of the bone and thus in this assay the targeting is not being tested and 2.) the alendronate doesn't have any intrinsic cytotoxic activity against cancer cells. The benefit of utilizing alendronate as a targeting component is realized in further studies where bone is introduced into the experimental models.

Our previous publications describe the linker system used to attach amine containing ligands, in this case ALN, to the nanoparticle surface [11],[17]. This method noncovalently incorporates Bis[sulfosuccinimidyl] suberate (BS3) linker with its amine reactive N-hydroxysulfosuccinimide (NHS) ester into a nanoparticle stabilizer coating consisting of poly (vinyl alcohol) (PVA). The amine reactivity of the BS3 linker allows the amine group of ALN to be conjugated to the surface of the nanoparticle while the bisphosphonate groups of ALN are left reactive and facing outward with the ability to bind to hydroxyapatite. Bisphosphonates are used clinically as anti-resorptive drugs that have high binding affinity for hydroxyapatite[18]. They are approved for use in a variety of conditions ranging from osteoporosis, multiple myeloma, and Paget's disease, to palliation for various skeletally metastasized cancers. Additionally, because of its high osteotropism and known toxicity profile, our group as well as others have pursued various strategies to utilize bisphosphonates groups in conjugation to proteins, liposomes, and nanoparticles so that therapeutics can be targeted to the bone[19-21]. However, cabazitaxel has not been utilized as a therapeutic payload in this context and few preclinical studies have

investigated whether these bone targeted nanoparticle systems are effective in improving functional status and maintaining bone structure in the setting of bone metastatic cancer.

Using an intraosseous model of bone metastatic prostate cancer, we measured tumor burden using two orthogonal approaches, with limb tumor weights and bioluminescence imaging. We found that all three treatment groups had a significant difference in tumor limb weight after the experiment and the non-targeted NP and targeted NP treatments had a very significant reduction in tumor size compared to the control group (P value = 0.0001). Results of the bioluminescence imaging were consistent with the tumor weight studies. In addition, there was a significant difference between the targeted NP and free cabazitaxel treatment groups tumor limb weight (P value = 0.0447), however no significant difference between the non-targeted and the free cabazitaxel groups (Figure 5). We speculate that the beneficial effect of both the targeted NP and non-targeted NP groups could be explained from the nature of a two-stage targeting effect. The first stage, utilizing the EPR of the tumors by employing the size of the nanoparticle to concentrate the drug at the site of the tumor is used by both the targeted and non-targeted NP. While the second stage incorporates bone targeting by utilizing the alendronate coating on the surface of the targeted NP to bind the hydroxyapatite structure and further increase cabazitaxel at the lesion.

In addition to evaluation of tumor size, x-ray imaging revealed no bone lesions in the animals treated with targeted NPs. This is compared to the other treatment groups which developed varying degrees of lesions attributed to the osteoclastic nature of the lesions characteristic of the

PC-3 cell line (Figure 5). We suspect that improved drug delivery to the lesion with the targeted NP served to mitigate bone damage by inhibiting the vicious cycle of bone destruction that occurs in the bone microenvironment setting.

Most literature evaluating pre-clinical therapeutic agents for bone metastatic cancer focus on tumor efficacy while neglecting an important clinical aspect, which is pain and functional status. In addition to studying the tumor efficacy *in vivo,* we have utilized animal behavioral assays in the overall evaluation of the bone targeted nanoparticles. Two behavioral assays were utilized to gauge whether the treatments had an impact on the functional status of the mice and the pain they experience. The first test was a gait analysis that can assess the change in gait pattern[22]. As the tumors and treatments progressed, a slight difference was observed in gait parameters measured in tumor burdened limb with a trend toward improved gait in the targeted NP group (data not shown). In addition, the von Frey assay was used to indicate functional pain status in these mice[23-25]. Interestingly, we found the group treated with targeted NPs had a significant reduction in relative response indicating they were experiencing less pain. These initial functional tests provide insight into the value of utilizing these targeted NP for bone metastatic prostate cancer and future research will focus on more functional status testing and elucidating more thoroughly the mechanisms involved.

V. CONCLUSION

This bone targeted nanoparticle system shows promise for treating bone metastatic prostate cancer. Notably, this targeted nanoparticle formulation showed efficacy in treating prostate cancer bone metastasis, improved bone structure, and reduced pain from the bone tumor.

VI. MATERIAL AND METHODS

Nanoparticle Formulation

The nanoparticles were prepared using a water-in-oil-in-water emulsion solvent evaporation similar to that described previously[11]. Briefly, 20 mg/ml PLGA 50:50 i.v. 0.77 dL/g (~0.5% w/v in chloroform at 30^{o} C); m.w. 124 kDa (Lakeshore Biomaterials) and 5% cabazitaxel (MedChem Express, Monmouth Junction, NJ) was dissolved in 2 mL ethyl acetate. 400µl of PBS was added to the 2 mL ethyl acetate PLGA solution and vortexed for 30 seconds, followed by sonicating with ultrasonic processor UP200H system (Hielscher Ultrasonics GmbH, Germany) twice at 40% amplitude for 30 seconds on ice. This mixture was then transferred to an aqueous solution of 10 mL of 1% poly (vinyl-alcohol) (Sigma) plus 0.5mg/ml of (Bis[sulfosuccinimidyl] suberate (BS3) crosslinker (ProteoChem) followed by sonication for 1 minute on pulsing mode at 40% amplitude on ice. Excess solvent was evaporated under continuous magnetic stirring for 2-3 hours. These nanoparticles were washed three times by centrifugation and resuspended in water. Nanoparticles were then lyophilized on ATR FD 3.0 system (ATR Inc., MO, USA) and stored at 4^{o} C until used.

Conjugation of Alendronate on Nanoparticles

Lyophilized nanoparticles and alendronate (Santa Cruz Biotechnology) were used at a 1:1 w/w ratio and suspended in 1mL of PBS at room temperature for 15 minutes separately. Then, the two solutions were mixed together for 1 hour at room temp for alendronate conjugation. The reaction was stopped by adding 50mM Tris Buffer (pH 7.4) for 15 minutes at room temperature and excess alendronate was removed by centrifugation. The nanoparticle pellet was resuspended in PBS for use.

Nanoparticle Size and Polydispersity Index (PDI) Measurement

Hydrodynamic particle size and PDI of targeted NP and non-targeted NP were determined by dynamic light scattering (DLS) utilizing the Zetasizer Nano ZS instrument (Malvern Ltd).

Scanning Electron Microscopy (SEM)

Surface morphology of the nanoparticles was studied using SEM. Lyophilized nanoparticles were imaged using a Sigma VP Field Emission Scanning Electron Microscope (Carl Zeiss Microscopy Ltd). Cressington 108 Auto Sputter Coater for thirty seconds was utilized prior to imaging. The target used for coating was gold/platinum.

Encapsulation Efficiency and Drug Loading

The encapsulation efficiency of the cabazitaxel in the nanoparticles was determined by HPLC. First, a known amount of lyophilized nanoparticles were dissolved in acetronitrile for 4 hours. The Agilent 6460 QQQ HPLC/Mass Spectrometer system (Santa Clara, CA) equipped with a UV detector and reverse-phase C18 column (Allure C-18, 5 μm, 100mm x 4.6mm, Restek,

Germany) with gradient mobile phase with dilutent of acetonitrile: water (1:1, v/v), mobile phase A of Trifluoroacetic acid: water (0.5:1000, v/v) and mobile phase B of Trifluoroacetic acid: acetonitrile (0.5:1000, v/v). Samples were run at a constant flow rate of 1 mL/min and the cabazitaxel quantified by integration of the area under its peak at wavelength of 220 nm and used to compare with the standard curve. The equation that was used to calculate encapsulation efficiency (EE) was: EE = (actual amount of drug encapsulated in nanoparticles) / (starting amount of drug used in nanoparticles) x 100%. Drug loading (DL) was calculated with the equation: DL= (weight of drug in nanoparticles) / (weight of nanoparticles) x 100%.

Drug Release Kinetics

The percentage of total cabazitaxel released at various time points was determined using a dialysis method. Nanoparticles were suspended in PBS at a concentration of 5 mg/ml. 100 µl of NP solution was added to Slide-A-Lyzer Mini Dialysis Units with 3500 MWCO (Life Technologies) and placed in sink conditions of 4L PBS at 37° C with stirring at 100 rpm for indicated time points. At indicated time points, acetonitrile was used to recover nanoparticles and drug that remained in dialysis chamber. Amount of drug that remained in nanoparticles was quantified by HPLC as described above.

Cancer Cell Viability

Prostate cancer cell lines PC-3-luciferase and C4-2B-luciferase were used to assess cell viability after treatment with nanoparticles or cabazitaxel. PC-3-luciferase cells were generously provided by Dr. Dan Theodorescu (University of Colorado Cancer Center) and C4-2B-luciferase cells were generously provided by Dr. Even Keller (University of Michigan). PC-3 cells were grown in DMEM/F12 media supplemented with 10mM Sodium pyruvate, 10% FBS, and 1% antibiotic-

antimycotic (Gibco) while C4-2B cells were grown in RPMI-Media supplemented with 10% FBS and 1% antibiotic-antimycotic (Gibco). Cells were plated in quadruplicate on 96 well flat bottom plates (Corning Incorporated Durham, NC) at a density of 2000 cells per well. Cells were allowed to attach for 24 hours then treated with nanoparticles or free drug for a period of 24, 48, or 72 hours in standard cell culture conditions. At respective time points 20 μl Tiazolyl Blue Tetrazolium Bromide (MTT) (Sigma, St. Louis, MO) suspended in PBS at a concentration of 5mg/mL was added to the 96 well plate. After 3 hours of incubation, media was removed and 100 μl of DMSO was added to all wells and mixed by pipetting. Absorbance was read on BioTek Synergy 2 Multi-Mode Plate Reader (Winooski, VT) at 570 nm for triplicate samples.

3D Spheroid Assay

3D prostate cancer spheroid assay was used to compare cytotoxicity of nanoparticles to free drug. Cells were plated on Lipidure-Coat 96 well U bottom plate at an initial density of 1000 cells per well and cultured in standard conditions. After 48 hours, spheroids were treated with nanoparticles or free drug. After 72 hours of treatment, calcien AM was added to each well and fluorescent image was taken with the Olympus AX70 Florescent Microscope. Integrated fluorescent intensity of spheroids was quantified using Image J software.

***Ex Vivo* Bone Binding Assay**

Affinity of the alendronate coated nanoparticles to the bone was determined utilizing an *ex vivo* binding assay. Accordingly, nanoparticles were formulated with Nile red dye encapsulated as a fluorescent tag and then either conjugated with alendronate on the outside or surface neutralized with Tris buffer. Freshly excised mouse femurs were cleaned of tissue and incubated in Eppendorf tubes with 5 mg/mL of nanoparticles in PBS at room temperature on gentle rocking

for either 6, 24, or 72 hours. At specified time points, bones were removed from nanoparticle solution, washed in PBS, and fluorescently imaged using the IVIS Animal Imaging System (Perkin Elmer, Waltham, MS).

Intraosseous Efficacy Experiment

After institutional IACUC approval, an orthotopic bone tumor model was used to test *in vivo* nanoparticle efficacy. Male athymic mice were purchased from Harlan laboratories and were 6-7 weeks old. Mice were allowed to acclimate 1 week before experiments. Mice were anesthetized with buprenorphine SR and isoflurane gas and injected at the proximal tibia with 1 x 10^6 PC-3 luciferase cells. Tumors developed for 1 week then randomized into groups by determining bioluminescence signal with VivoGlo Luciferin (Promega) per manufacturer's instructions so that starting bioluminescence signal was equal across treatment groups at day 7. On day 7 after tumor initiation, treatment commenced with weekly intravenous injections via lateral tail vein. Treatment groups were: saline, free cabazitaxel, non-targeted NP, and targeted NP. X-ray and bioluminescence were used to monitor groups at the final time point. At experiment termination mice were sacrificed by CO2 asphyxiation. Lower limb tumors were removed and analyzed.

Von Frey

The paw withdrawal threshold (PWT) in response to mechanical stimulation was measured by applying calibrated von Frey filaments from underneath the cage through openings in the mesh floor to the hindpaws. Mice were placed in separate transparent plexiglass chambers with a wire mesh floor underneath and acclimated to the test chamber for 2 minutes. A filament with 4.17 grams of force was applied vertically to the plantar surface of the hind paw repeatedly ten times with 10 seconds rest in between so the filament was bent during each test. The von Frey filament

was chosen based on preliminary tests that showed to be intermediate between the lowest force with no response and the force which had consistent response. Brisk withdrawal, paw flinching or licking was considered a positive response and recorded. Both the right and left paw were measured. The response rate on the right where the tumor was implanted was subtracted from that of the left to control for inter-mouse variability.

Gait Analysis

Gait was assessed with a simple footprint test. The hindpaws were painted and the mouse was pre-trained to walk in a straight line (2 trials) over absorbent paper in a rectangular acrylic box made to mimic a dark alley lined with absorbent paper. The footprint patterns were analyzed for stride length and base width. Mice were assessed at three sessions each one week apart.

VII. REFERENCES

1. Coleman RE. Clinical features of metastatic bone disease and risk of skeletal morbidity. *Clinical cancer research : an official journal of the American Association for Cancer Research* 12(20 Pt 2), 6243s-6249s (2006).

2. Howlader N NA, Krapcho M, Miller D, Bishop K, Altekruse Sf, Kosary Cl, Yu M, Ruhl J, Tatalovich Z, Mariotto a, Lewis Dr, Chen Hs, Feuer Ej, Cronin Ka (Eds). SEER Cancer Statistics Review, 1975-2013, National Cancer Institute. (2016).

3. Gartrell BA, Saad F. Managing bone metastases and reducing skeletal related events in prostate cancer. *Nature reviews. Clinical oncology* 11(6), 335-345 (2014). *This article provides a clinic overview of the managing bone metastatic prostate cancer.

4. Saad F, Gleason DM, Murray R *et al*. A randomized, placebo-controlled trial of zoledronic acid in patients with hormone-refractory metastatic prostate carcinoma. *Journal of the National Cancer Institute* 94(19), 1458-1468 (2002).

5. Fizazi K, Carducci M, Smith M *et al*. Denosumab versus zoledronic acid for treatment of bone metastases in men with castration-resistant prostate cancer: a randomised, double-blind study. *Lancet (London, England)* 377(9768), 813-822 (2011).

6. Petrylak DP, Tangen CM, Hussain MH *et al*. Docetaxel and estramustine compared with mitoxantrone and prednisone for advanced refractory prostate cancer. *The New England journal of medicine* 351(15), 1513-1520 (2004).

7. Tucci M, Bertaglia V, Vignani F *et al*. Addition of Docetaxel to Androgen Deprivation Therapy for Patients with Hormone-sensitive Metastatic Prostate Cancer: A Systematic Review and Meta-analysis. *European urology* 69(4), 563-573 (2016).

8. Parker C, Nilsson S, Heinrich D *et al*. Alpha emitter radium-223 and survival in metastatic prostate cancer. *The New England journal of medicine* 369(3), 213-223 (2013). *This article provides one of the first bone targeted agents that improves overall survival in the context of bone metastatic prostate cancer.

9. Dansereau RN. A unique drug distribution process for radium Ra 223 dichloride injection and its implication for product quality, patient privacy, and delineation of professional responsibilities. *The Annals of pharmacotherapy* 48(11), 1512-1514 (2014).

10. Autio KA, Scher HI, Morris MJ. Therapeutic strategies for bone metastases and their clinical sequelae in prostate cancer. *Current treatment options in oncology* 13(2), 174-188 (2012).

11. Thamake SI, Raut SL, Gryczynski Z, Ranjan AP, Vishwanatha JK. Alendronate coated poly-lactic-co-glycolic acid (PLGA) nanoparticles for active targeting of metastatic breast cancer. *Biomaterials* 33(29), 7164-7173 (2012). *This article was part of our previous work with bone targeting in metastatic breast cancer.

12. Mohan S, Baylink DJ. Bone growth factors. *Clinical orthopaedics and related research* (263), 30-48 (1991).

13. Wang F, Chen L, Zhang R, Chen Z, Zhu L. RGD peptide conjugated liposomal drug delivery system for enhance therapeutic efficacy in treating bone metastasis from prostate cancer. *Journal of controlled release : official journal of the Controlled Release Society*

196 222-233 (2014). **This article provides an excellent design and characterization of bone targeted liposomes and includes a reduction in pain as well as efficacy against the tumor.

14. Paller CJ, Antonarakis ES. Cabazitaxel: a novel second-line treatment for metastatic castration-resistant prostate cancer. *Drug design, development and therapy* 5 117-124 (2011).

15. Galsky MD, Dritselis A, Kirkpatrick P, Oh WK. Cabazitaxel. *Nature reviews. Drug discovery* 9(9), 677-678 (2010).

16. Nightingale G, Ryu J. Cabazitaxel (jevtana): a novel agent for metastatic castration-resistant prostate cancer. *Pharmacy and Therapeutics* 37(8), 440 (2012).

17. Thamake SI, Raut SL, Ranjan AP, Gryczynski Z, Vishwanatha JK. Surface functionalization of PLGA nanoparticles by non-covalent insertion of a homo-bifunctional spacer for active targeting in cancer therapy. *Nanotechnology* 22(3), 035101 (2011).

18. Reszka AA, Rodan GA. Bisphosphonate mechanism of action. *Current rheumatology reports* 5(1), 65-74 (2003).

19. Swami A, Reagan MR, Basto P *et al*. Engineered nanomedicine for myeloma and bone microenvironment targeting. *Proceedings of the National Academy of Sciences of the United States of America* 111(28), 10287-10292 (2014). *This article provides evidence for effectiveness of a bone targeted nanoparticle loaded with bortezomib in the context of multiple myeloma.

20. Chang Q, Geng R, Wang S, Qu D, Kong X. DOPA-based paclitaxel-loaded liposomes with modifications of transferrin and alendronate for bone and myeloma targeting. *Drug delivery* 23(9), 3629-3638 (2016).

21. Doschak MR, Kucharski CM, Wright JE, Zernicke RF, Uludag H. Improved bone delivery of osteoprotegerin by bisphosphonate conjugation in a rat model of osteoarthritis. *Molecular pharmaceutics* 6(2), 634-640 (2009).

22. Lakes EH, Allen KD. Gait analysis methods for rodent models of arthritic disorders: reviews and recommendations. *Osteoarthritis and cartilage* 24(11), 1837-1849 (2016).

23. Blackburn-Munro G. Pain-like behaviours in animals - how human are they? *Trends in pharmacological sciences* 25(6), 299-305 (2004).

24. Lariviere WR, Wilson SG, Laughlin TM *et al*. Heritability of nociception. III. Genetic relationships among commonly used assays of nociception and hypersensitivity. *Pain* 97(1-2), 75-86 (2002).

25. Mogil JS, Crager SE. What should we be measuring in behavioral studies of chronic pain in animals? *Pain* 112(1-2), 12-15 (2004).

CHAPTER III

PROGRAMMABLE BIOINSPIRED NANOPARTICLES ENGINEERED FOR TARGETED DELIVERY TO THE BONE

I. ABSTRACT

Targeting therapeutic agents to specific organs in the body remains a challenge despite advances in the science of systemic drug delivery. We have engineered a programmable bioinspired nanoparticle (P-BiNP) delivery system to simultaneously target the bone and increase uptake in homotypic tumor cells by coating polymeric nanoparticles with programmed cancer cell membranes. This approach is unique in that we have incorporated relevant clinical bioinformatics data to guide the design and enhancement of biological processes that these nanoparticles are engineered to mimic. To achieve this, an analysis of RNA expression from metastatic prostate cancer patients identified ITGB3 (a subunit of integrin $\alpha V\beta_3$) as overexpressed in patients with bone metastasis. Cancer cells were stimulated to increase this integrin expression on the cell surface and these membranes were subsequently used to coat cargo carrying polymeric nanoparticles. Physicochemical optimization and characterization of the P-BiNPs showed desirable qualities regarding size, zeta potential, and stability. *In vitro* testing confirmed enhanced homotypic binding and uptake in cancer cells. P-BiNPs also demonstrated improved bone localization *in vivo* with a murine model. This novel approach of identifying clinically relevant targets for dual homotypic and bone targeting has potential as a strategy for treatment and imaging modalities in diseases that affect the bone as well as broader implications for delivering nanoparticles to other organs of interest.

II. INTRODUCTION

Nanoparticles have the potential to improve drug delivery through targeting either by passive or active means. Passive targeting utilizes the small size of nanoparticles to achieve enhanced permeability and retention (EPR) in tumors through penetration of leaky vasculature and accumulation in the tumor due to inadequate or absent lymphatic drainage [1]. In comparison, active targeting requires the use of a ligand against an entity that is overexpressed on cancer cells to allow increased binding and uptake of the nanoparticle, thereby improving cargo uptake into the cancer cell [2]. In the preclinical setting, both passive and active strategies have been employed effectively to enrich nanoparticle concentration in tumors. However, the active targeting approach for nanoparticles has been generally less successful, especially in the clinical setting.

This difference between preclinical success and clinical translation may be due to a variety of factors. First, many ligand coating strategies for targeted nanoparticles involve difficult and complicated chemical conjugation strategies which can alter the ligand's affinity for its target [3]. Second, often the choice of target in the preclinical setting is made without the input of clinically relevant targets and data from patients. Third, an often-neglected consideration in engineering targeted nanoparticles is the impact of ligand surface density on binding as well as uptake into cells [4]. Fourth, the heterogeneity of surface markers on cancer cells often diminishes the ability to efficiently target all cells which make up the tumor [5].

Considering these factors, we have designed and engineered a biologically inspired strategy to simultaneously enhance nanoparticle delivery to the bone with increased targeted cell uptake.

The primary goal of this approach was inspired by prostate cancer cells' ability to home to the bone during the metastatic process. The progression of bone metastasis is quite complex and involves multiple coordinated events including escape from the primary tumor, survival in systemic circulation, and the ability to home to the bone microenvironment [3, 6]. This nanoparticle delivery system seeks to mimic the latter two processes so that nanoparticle cargo can be transported and retained in the bone. Coating nanoparticles with biological membranes has been shown to increase the circulation time of the nanoparticles due to the improved biocompatibility in systemic circulation [7]. In addition, specific factors involved in the homing process that are present on the membranes can be enhanced through *ex vivo* biological methods and thus eliminate the need for traditional challenging chemical conjugation schemes. This alternative strategy allows fusing the cell membranes to core nanoparticles as a simple method to create a complex biocompatible system for improved targeting ability.

Several essential factors involved in prostate cancer cells homing to the bone have been described in the *in vitro* and *in vivo* experimental setting [8]. However, less data exists demonstrating validation of these alterations in human samples. Thus a combination of *in vivo* data and patient RNAseq data was evaluated in selecting factors that could be enhanced. A bioinformatics analysis of an RNAseq database from prostate cancer patients with metastasis to various sites was used to establish differentially expressed factors in patients with bone metastasis. Increased mRNA expression was used as an indicator of factors involved in the bone metastatic process. ITGB3 was identified as having increased expression in the tumors of patients with bone metastatic prostate cancer but not metastasis to other common locations such as the liver and lymph nodes. ITGB3 encodes an important subunit of the integrin $\alpha V\beta_3$ which is

a critical factor contributing to the ability of prostate cancer cells to specifically home and bind to endothelial cells in the bone [9]. Increased membrane expression of this integrin occurs when prostate cancer cells are stimulated by the chemokine factor, C-X-C motif chemokine ligand 12, (CXCL12) that originates from osteoblasts in the bone [9]. We hypothesized that using this signaling pathway we would be able to stimulate or program BiNPs to have enhanced bone homing and retention.

The secondary objective of the P-BiNPs was to achieve selective uptake in specific cells so that once the nanoparticles have homed to the organ of interest, there will be preferential uptake into the identified cells. This strategy has the potential to improve delivery of therapeutic agents, enhance imaging agents, and decrease off-target side effects.

III. RESULTS AND DISCUSSION

Target Identification and Validation

Several studies have demonstrated the principle of homotypic targeting, through which nanoparticles can be coated with various cancer cell lines and result in higher uptake into homologous tumors [10-13]. However, the factors responsible for homotypic binding have largely been unexplored especially in the clinical context. Further, it has not been established whether stimulating a factor that is important in homotypic binding can simultaneously be exploited for enhancing delivery of nanoparticles to an organ of interest. Thus, the goal of this manuscript was to test the proof of concept that personalized nanoparticles could be engineered with enhanced ability for synchronized selective organ localization and homotypic binding (Figure 7). Prostate

cancer was chosen as the prototype for this proof of concept due to its high prevalence, bone homing ability in the metastatic setting, and low immunogenicity.

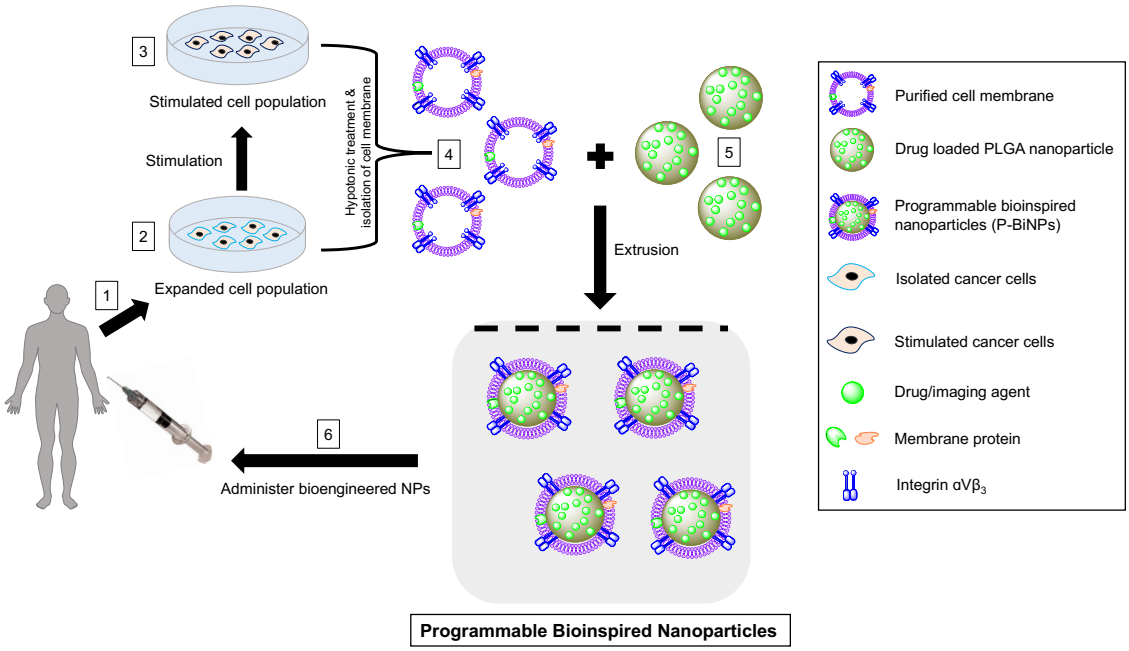

Figure 7: Proposed clinical scenario of programmable bioinspired nanoparticles. (1) Cells are isolated from patient's biopsy. (2) Cells are grown in a petri dish and programmed by (3) stimulation with CXCL12 to enhance homotypic binding and bone adhesion ability. (4) Membrane is isolated from programmed cancer cells and used to coat (5) nanoparticles with drug or imaging agent cargo. (6) Programmable bioinspired nanoparticles (P-BiNPs) are injected back into patient with enhanced bone homing and homotypic binding.

A gene set enrichment analysis (GSEA) search identified 50 genes that were enhanced in the process of homotypic cell-cell adhesion. Subsequent bioinformatics analysis of a RNAseq database from metastatic prostate cancer patient samples (n=118) identified ITGB3 as being

significantly increased in bone metastatic lesions compared to metastases from other sites such as liver, lymph nodes, or other organs (P <0.0001) (Figure 8). ITGB3 is a subunit of integrin $\alpha V\beta_3$ and was selected as a clinically relevant target protein for which enhancement could impact nanoparticle delivery to bone and homotypic binding in the final P-BiNP.

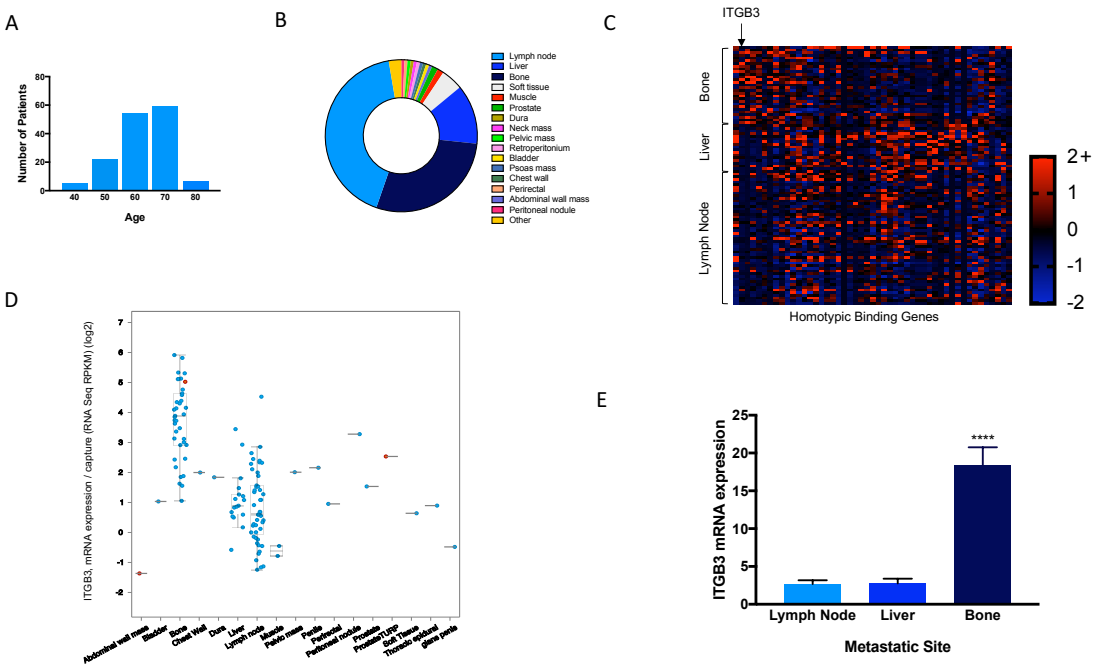

Figure 8: $\alpha V\beta_3$ identified as target for enhanced homotypic binding and bone adhesion. (A) Age of patients at diagnosis in database. Total patients involved in study (n=150). Tumor samples with mRNA in database (n=118). **(B)** Percentage distribution of prostate cancer metastatic locations, the top three metastatic sites were bone, liver and lymph node. **(C)** Heat map of mRNA z-score organized by metastatic location vs. genes identified by gene set enrichment analysis involved in homotypic cell-cell adhesion. **(D)** Increased expression of the beta 3 (ITGB3) subunit of $\alpha V\beta_3$ integrin in bone metastatic prostate cancer compared to other metastatic sites. **(E)** Quantification of ITGB3 expression levels (RNA Seq RPKM) of the three

most common metastatic locations. Bone has a significantly higher level of expression of ITGB3 compared to liver and lymph nodes. Mean ± SEM. **** P <0.0001.

CXCL12 was identified through a literature search as a ligand that can increase surface expression of integrin $\alpha V\beta_3$ through binding to CXCR4 on cancer cells in culture. Further, the increased $\alpha V\beta_3$ expression has been shown to increase binding of prostate cancer cells specifically to bone marrow-derived endothelial cells in experimental models [9]. The C4-2B prostate cancer cell line has been used for this proof of concept. This prostate cancer cell line has known ability to create bone lesions in a mouse model [14-15].

C4-2B prostate cancer cells were first stimulated with CXCL12 for varying amounts of time and the expression level of $\alpha V\beta_3$ was determined after specified time points through immunocytochemistry. There was an approximately 2-fold increase in expression level of $\alpha V\beta_3$ after the first hour of stimulation and this remained constant for the duration of the experiment (Figure 9). Thus, 1 hour was chosen as the length of time needed to program the cells for increased surface expression of $\alpha V\beta_3$ in subsequent experiments.

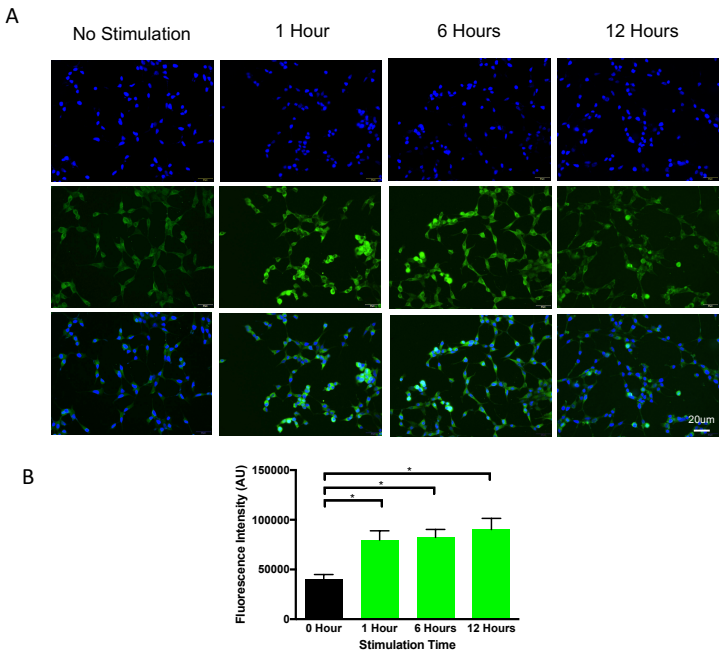

Figure 9: Programming cancer cells to have higher surface expression of $\alpha V\beta_3$. (A) Representative immunocytochemistry images of C4-2B cells at various time points after stimulation. (Top) Dapi. (Middle) $\alpha V\beta_3$ expression. (Bottom) Overlay. **(B)** Quantification of average fluorescent intensity per cell with increased $\alpha V\beta_3$ surface expression after stimulation (n=3). * $P< 0.05$. Mean ± SEM.

Preparation and Characterization of Nanoparticles

After cancer cells were programmed to have increased expression of $\alpha V\beta_3$, the next step was to isolate those cancer cell membranes and optimize the coating and physical properties of the nanoparticles. We first isolated the membranes by a differential centrifugation technique to harvest the lipid and embedded protein components. Western blot was used to verify the purity of the membrane fraction and confirmed the presence of Na/K ATPase, a membrane marker, in

both the whole cell lysate and purified membrane samples. As expected, nuclear marker (lamin) and mitochondrial marker (cytochrome C) were absent in the purified membrane lysates but present in the whole cell lysates (Supplemental 2). Additionally, coomassie blue stain displayed a considerable profile of membrane proteins that were expressed after the membrane purification process in both C4-2B and LNCaP prostate cancer cell lines (Supplemental 2). These other membrane proteins may also have an impact on the homotypic binding and bone adhesion of the nanoparticles beyond the known functional influence of $\alpha V\beta_3$ integrin.

Next, the ideal amount of cell membrane to coat the nanoparticle was explored using a nanoparticle stability assay. Various ratios of nanoparticle to cell membrane were coated and then introduced into an ionic solution of PBS to induce aggregation of non-coated or partially coated nanoparticles as measured by an increase in hydrodynamic diameter [10, 16]. Nanoparticles coated with ratios of 0.25:1 and 0.5:1 (weight of cell membrane protein to weight of polymer) were most stable after being introduced into PBS. Whereas, non-coated PLGA nanoparticles and P-BiNPs with membrane to polymer ratio of .1:1 tended to aggregate. Thus, the ratio 0.5:1 was selected for further experiments (Supplemental 2). For the nanoparticle core, we have utilized Poly(DL-lactide-co-gylcolide) (PLGA) polymeric nanoparticles due to their negative zeta potential, biocompatibility, and high encapsulation efficiency of hydrophobic molecules that can be loaded for therapeutic or imaging purposes [17].

Nanoparticle size, as measured by dynamic light scattering (DLS), showed an expected size increase after being coated with the cancer cell membrane. The initial size of non-coated

nanoparticles was 97.2 nm and increased to 117-138 nm when coated (P<0.0001) (Figure 10). Transmission electron microscopy (TEM) was used to visualize and verify the membrane coating on the NP (Figure 10). Zeta potential also significantly changed as the nanoparticles were coated with the cancer cell membrane from -44 mV when uncoated, to -28 mV through -33 mV in the coated nanoparticles (Figure 10). Other cell types were tested and found to have similar trends in both increased size and zeta potential measurements when nanoparticles were coated. Also, stability measurements of both the BiNP and the P-BiNP show similar constancy in both size and PDI over the time course of one week when stored at 4° C.

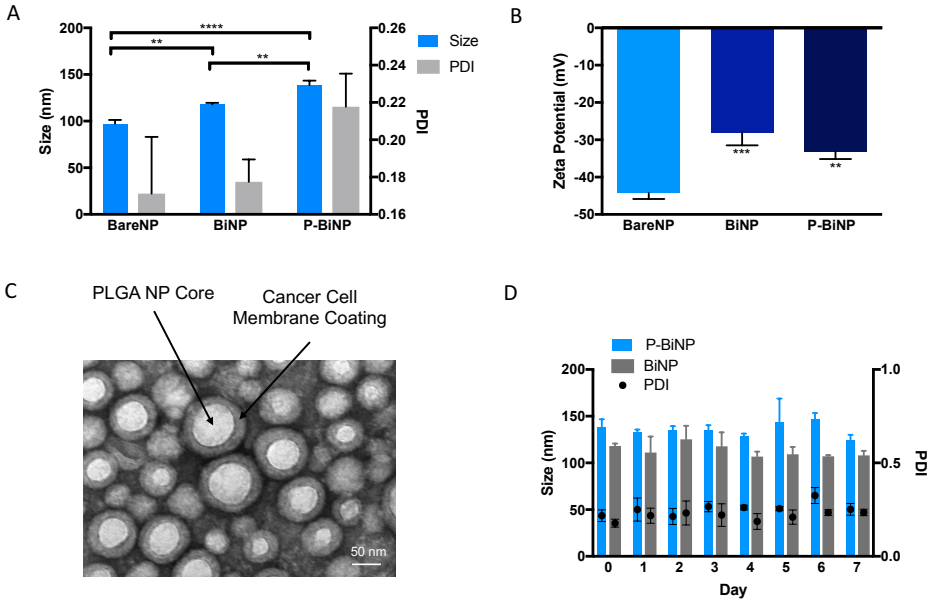

Figure 10: Nanoparticle characterization. (A) Size and PDI of nanoparticles as measured by dynamic light scattering. There was a clear increase in size when comparing bare nanoparticles to nanoparticles coated with membranes. **(B)** Zeta potential measurements resulted in a less

negative zeta potential when comparing bare nanoparticles to membrane coated nanoparticles. **(C)** Transmission electron micrograph (TEM) of BiNP nanoparticles showing coating with cancer cell membrane. **(D)** Stability study performed for 7 days demonstrates the nanoparticles are not aggregating in solution. Samples run in triplicate. Mean ± SEM. ** P <0.01, *** P <0.0005, **** P<0.0001.

In Vitro Uptake and Cytotoxicity of P-BiNPs

Some cancer cells and nanoparticles coated with cancer cells have been reported to exhibit homotypic binding properties in which they self-recognize tumor cells of the same type [12, 18]. To determine whether this self-recognition could be enhanced through programming cells to increase expression of $\alpha V\beta_3$ by a natural stimulation process we treated both C4-2B and fibroblasts with either BareNPs, BiNPs, or P-BiNPs that were derived from C4-2B membranes and fluorescently labeled. Flow cytometry and immunocytochemistry were used to measure the uptake in the cells. P-BiNPs had a much higher uptake in the C4-2B cell line as measured through flow cytometry (Figure 11). The approximately 4-fold increased uptake with the P-BiNP group compared to the BiNP group indicates that the stimulation process is an important factor for enhancing the nanoparticle cellular uptake.

This increased uptake was also studied by labeling both the membrane component and the nanoparticle core with two separate fluorescent dyes of different peak emission wavelengths prior to nanoparticle coating (Supplemental 3). Co-localization of both fluorescent dyes after confocal microscopy imaging was found indicating that the nanoparticles and coating were taken

up in the cancer cells as a unit. Moreover, when 3D prostate cancer spheroids were created, the P-BiNP had no issue thoroughly penetrating the spheroid (Supplemental 4).

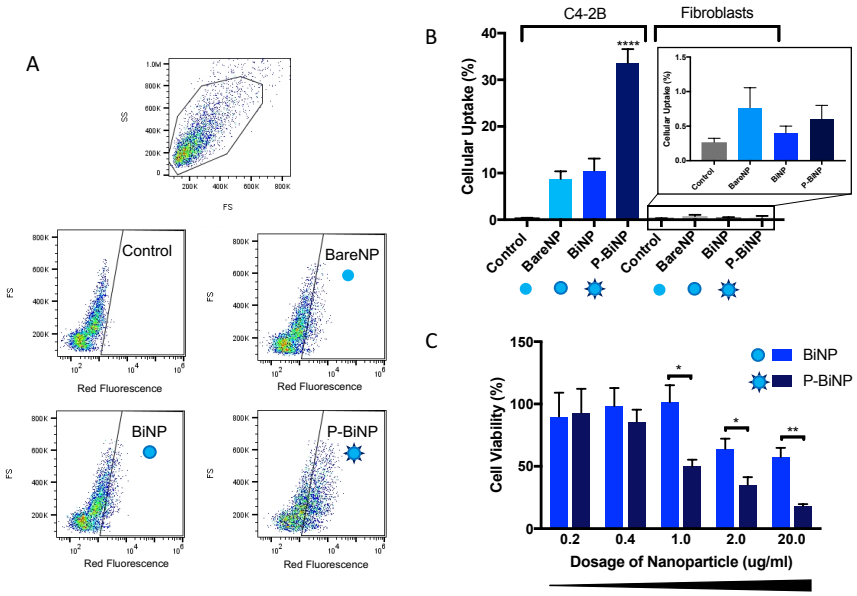

Figure 11: Programmed bioinspired nanoparticles have increased uptake into cancer cells. **(A)** Representative images of flow uptake experiment. Nanoparticles were tagged with nile red dye and incubated with C4-2B prostate cancer cells or human fibroblast cells for 1 hour and uptake was assessed through flow cytometry gated to detect nile red fluorescence. **(B)** Quantification of triplicate experiments showing highest uptake in C4-2B cells when incubated with P-BiNPs. (Inset) Nanoparticle uptake in fibroblast. **(C)** MTT cell viability assay after treatment with increasing concentrations (0.2-20.0 mg/ml) of BiNP or P-BiNP resulting in decreased cell viability of P-BiNPs at equivalent treatment dosage as BiNPs after 72 hours. (n=4). Mean ± SEM. * P < 0.05, ** P <0.01, **** P<0.0001.

Increased cell uptake into cancer cells and tumors should result in improved cytotoxicity of chemotherapy delivered to the cells as the molecules are transported inside the cells more efficiently. We tested whether programming cabazitaxel loaded nanoparticles to have increased $\alpha V\beta_3$ on their surface would translate to having increased cytotoxic effects compared to BiNP with no stimulation using a MTT cell viability assay. Cabazitaxel was chosen as a model drug because in addition to being FDA approved for metastatic prostate cancer, it has lower substrate affinity for the ATP-dependent drug efflux pump glycoprotein (P-gp) that is commonly up-regulated in metastatic and chemotherapy-resistant cancers [19]. Thus, Cabazitaxel is less likely to be pumped out of the advanced tumor cells after gaining entrance into the cell. P-BiNPs showed decreased cell viability compared to BiNP (Figure 11) demonstrating that the natural stimulation process can enhance therapeutic efficacy via improvement of chemotherapy delivery inside the cell.

In Vivo Bone Homing of P-BiNPs

Bolstering homotypic targeting was one of the design goals of this nanoparticle. The second objective was enhancing the ability of the P-BiNP to bind to the bone through a bioinspired and clinically relevant approach. This was achieved by identification of $\alpha V\beta_3$ integrin playing an important role in bone homing of prostate cancer. This integrin has been studied in the context of tumor cell adhesion to bone components such as vitronectin, bone sialoprotein, osteopontin, and other bone extracellular matrix factors [20-23]. It is possible that the low blood flow environment of

the bone coupled with the binding affinity of $\alpha V\beta_3$ generates a suitable situation for prostate cancer cells to bind to the bone during the metastatic process.

A systemic injection was utilized to test whether there was increased accumulation BiNP and P-BiNP in the bone. This route of administration indicates whether the P-BiNPs can mimic the bone homing ability observed in prostate cancer cells. It was found that two hours after mouse tail vein injection, the P-BiNPs groups had a higher fluorescent signal in the bone compared to the BiNP and the dye injected groups. Interesting it was also found that the P-BiNP had a higher concentration in the heart compared to the BiNP. However, the absolute amount of fluorescent signal in the heart was much less than that found in the bone in the P-BiNP group. Nevertheless, others have shown that stem cells can home to the heart after damage to cardiac tissue through a chemotactic gradient from CXCL12. We suspect that the CXCL12 stimulation along with other factors may be responsible for the increased concentration of the P-BiNP in the bone and the slight increase in P-BiNP localized to the heart. As expected, there was also elevated levels of nanoparticles in the liver and lungs in all groups (Figure 12).

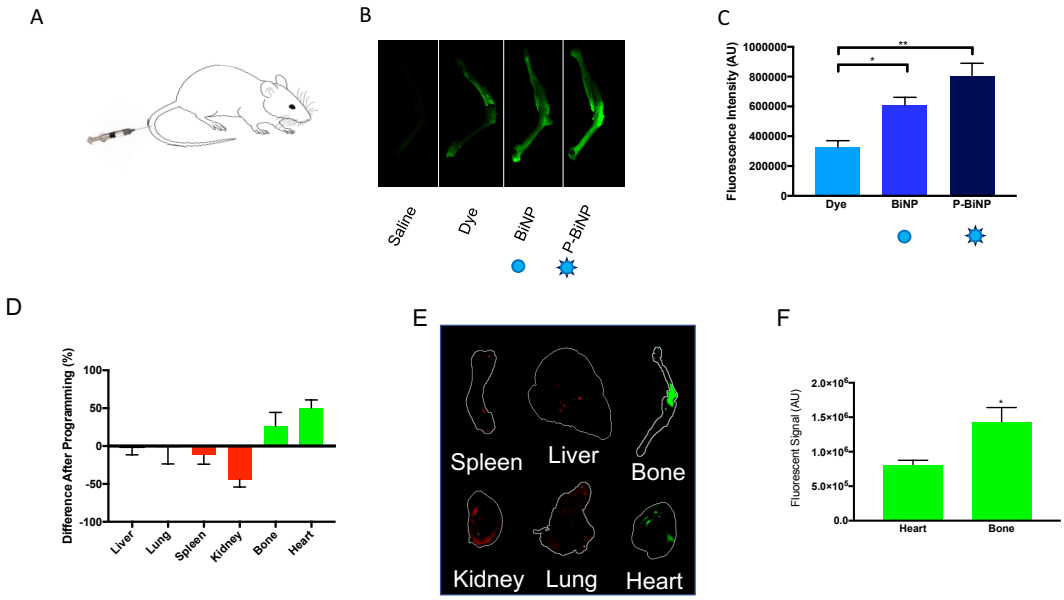

Figure 12: Enhancement of bone homing via programmable bioinspired nanoparticles. (A) Mice were injected intravenously via tail vein with either dye, BiNP, or P-BiNP. After two hours, organs (liver, kidneys, spleen, heart, lungs, and hind limb) were excised and imaged to detect NIR signal. **(B)** Hind limbs were scanned at high resolution for sensitive detection of NIR dye. Green = 800 nm wavelength emission of NIR dye. **(C)** Quantification of NIR signal in different treatment groups. **(D)** BiNP and P-BiNP nanoparticles were compared to determine effect of stimulation on nanoparticle organ localization. **(E)** Representative image showing difference in nanoparticle localization with a reduction in P-BiNP (red) or increased P-BiNP in a particular organ (green) compared to BiNP. **(F)** Total fluorescent signal comparing heart and lung of P-BiNPs. (n=4). Mean ± SEM. * $P < 0.05$, ** $P < 0.001$.

V. CONCLUSION

We have successfully utilized a bioinformatics identification process to engineer programmable bioinspired nanoparticles and demonstrated their utility of increased self-recognition of cancer cells as well as their ability to home to the bone. This novel bioinspired platform is promising in that we have incorporated relevant clinical gene expression data to guide the design and enhancement of biological processes that these nanoparticles mimic. It is envisioned that this platform can be used in future applications as a personalized approach for simultaneously delivering therapeutic or imaging agents to the bone and other organs with targeted uptake in designated cell types.

VI. MATERIALS AND METHODS

Bioinformatics Data

Gene ontology consortium (http://www.geneontology.org) query identified potential targets involved in homotypic cell-cell adhesion. These targets were cross-referenced with RNAseq expression levels from patients with metastatic prostate cancer to various organ locations. Multiple hits were identified for upregulated mRNA expression in bone metastatic samples compared to metastatic lesions of other sites. Literature analysis of the top differentially expressed genes revealed the functional importance of ITGB3 in its role as the critical subunit of integrin $\alpha V\beta_3$ in both prostate cancer cell homing to bone and in homotypic binding between cells. ITGB3 mRNA expression level was compared in the top three metastatic sites and bone had the most significantly increased expression level compared to lymph node and liver. cBioProtal was used to access the Metastatic Prostate Cancer Patient database, SU2C/PCF

Dream Team Cancer study was used as the primary database. The genomic profiles that were selected were mRNA expression data/ capture z-Scores (RNA Seq capture).

Cell Culture

C4-2B cells were purchased from MD Anderson Characterized Cell Line Core Facility (Houston, TX) and LNCaP cells were purchased from ATCC (Manassas, VA). Both cells lines were maintained in standard cell culture conditions (5% CO_2, 37°C) and cultured in RPMI-1640 medium, 10% fetal bovine serum, and 1% antibiotic-antimycotic (Gibco).

$\alpha V\beta_3$ Protein Stimulation and Verification

C4-2B cells were grown in triplicate on glass coverslips in a six-well dish and then stimulated to express $\alpha V\beta_3$ by treatment with 200 ng/mL of recombinant human CXCL12 (R&D Systems, Minneapolis, MN) for 1, 6, or 12 hours at 37°C. After cells were stimulated they were rinsed with PBS, fixed with 4% formaldehyde (Affymetrix) for 10 min at room temperature, washed twice with PBS, and blocked for 1 hour with 1% BSA in PBS. Next cells were incubated for 4 hours with a 1:100 dilution of anti-integrin $\alpha V\beta_3$ antibody, clone LM609 (Millipore). Incubation was followed by three washes with PBS, and then incubated for 45 minutes with a 1:200 dilution of the goat anti-mouse IgG (H+L) secondary antibody, Alexa Fluor 488 conjugate (Life Technologies). Cells were washed twice more and mounted on slides with Prolong Gold antifade reagent with DAPI (Invitrogen). Fluorescent images were taken with Olympus AX70 Florescent Microscope.

Cancer Coated Nanoparticle Preparation

C4-2B cells were grown to 90% confluency in a T-175 flask and then if P-BiNPs were to be made, they were stimulated with 200 ng/ml recombinant human CXCL12 for 1 hour at 37°C. After stimulation step for P-BiNP or no stimulation for BiNP, cells were prepared similarly to publication by Fang *et al*. with modifications [10]. Cells were washed with PBS and lifted from flask using 2mM ethylenediaminetetraacetic acid (EDTA) in PBS. Cells were washed three more times with PBS by centrifugation at 500 g. On final wash, cells were resuspended in hypotonic buffer solution consisting of 10mM KCl, 2mM MgCl2, 20mM Tris-HCl adjusted to pH 7.5. Immediately before hypotonic buffer use, 1 Pierce EDTA-free protease inhibitor tablet (Thermo Scientific) and phosphate inhibitor cocktail (EMD Millipore, USA) were added to 50mL of the hypotonic buffer. Next, cancer cells in the hypotonic buffer were placed in Dounce homogenizer and mashed 25 times. Homogenized cells were centrifuged at 3200 g for 5 minutes at 4°C on desktop centrifuge and supernatant was removed and saved on ice. Pellet was resuspended in hypotonic buffer and again the Dounce homogenizer was used for 25 mashes. The second homogenate was placed in centrifuge at 3200 g for 5 minutes at 4°C and supernatant was removed and placed on ice. Pooled supernatant was spun at 20,000 g for 20 minutes. The supernatant was removed and transferred to clean ultracentrifuge tubes and spun at 100,000 g for 16 hours. The supernatant was removed and discarded. Pellet consisting of purified cell membrane fraction was washed in Tris Buffer (10mM Tris-HCl with 1 mM EDTA adjusted to pH 7.5). The total protein in the membrane fraction was quantified using a Pierce BCA Protein Assay kit (Life Technologies) per manufacturer's instructions. This membrane was then used in further experiments.

PLGA nanoparticles were made using a nanoprecipitation method. Briefly, a 26 G flat tipped needle attached to a 1mL syringe was used to inject 7.5 mg/mL PLGA 5050 dissolved in acetone (Lakeshore Biopharmaceutics) into sterile water. The acetone was evaporated under nitrogen gas flow for 20 minutes. If cabazitaxel (5% initial w/w drug to polymer) (MedChem Express), Nile Red fluorescent dye (Invitrogen), or IR-780 dye (Sigma Aldrich) was to be used in the experiment, then it was dissolved in the initial PLGA/acetone mixture prior to nanoprecipitation. These nanoparticles were then used as the stock for the core of the cancer coated nanoparticles to ensure equivalent dye or drug concentration for an experiment.

Nanoparticle coating was performed by an extrusion process. The membrane fraction was extruded through a Nuclepore Track-Etch Membrane (Whatman) with 400 nm pore size 11 times using an Avanti Lipids extruder. Nanoparticles were added so that the ratio of membrane protein to nanoparticles (.5:1) (w/w). This mixture was extruded again 11 more times. Coated nanoparticles were collected and were used immediately after extrusion process.

Cancer Cell Membrane Fraction Verification

Western Blot was used to verify membrane fraction preparation by comparing protein expression in the pure membrane fraction versus whole cell lysate in two different cell lines. For the whole cell lysate, total protein was extracted from cancer cells and quantified. The membrane fraction used was from the protocol described above. Protein was separated on 4-12% Bis-Tris Nu-PAGE gel (Invitrogen, CA) with MES running buffer. The primary antibodies were against Na^+/K^+ ATPase as membrane marker (mouse monoclonal antibody from Developmental Studies

Hybridoma Bank, IA), lamin was used as a nuclear marker (Santa Cruz Biotechnology, CA), and cytochrome c was used as a mitochondria marker (Santa Cruz Biotechnology, CA). Appropriate secondary antibodies, diluted to 1:200, and conjugated with horseradish peroxidase (Promega, WI) were incubated with membranes for 2 hours at room temperature. Membranes were developed using ECL plus (Amersham Pharmacia Biotech, IL) and images were taken with α-imager Fluortech HD2 (San Jose, CA).

Coomassie stain was used to verify that the membrane fraction still maintained a broad profile of protein expressed on the surface of the cells. All initial steps are the same as described in the Western Blot procedure above however after the protein was separated on 4-12% Bis-Tris NuPAGE gel, it was stained with Coomassie Brilliant Blue (BioRad, CA) for 30 minutes. The gel was then destained for 2 days by washing with destain solution (20% methanol, 10% glacial acetic acid, in ddH_2O). The gel was then imaged with the α-imager Fluortech HD2.

Membrane Coating Stability

Various ratios of membrane to nanoparticles were used to determine the optimal ratio needed for complete coating of cancer coated nanoparticles. Nanoparticles were then incubated in PBS solution which will cause non-coated nanoparticles to aggregate. The size was checked after 12 hours by DLS utilizing the Zetasizer Nano ZS instrument (Malvern Ltd). In addition, we assessed whether there was a difference in stability between the P-BiNPs and BiNPs over the course of seven days when nanoparticles were stored at 4 degrees Celsius by measuring size and PDI daily.

Hydrodynamic Size and PDI

Particle size and PDI of membrane coated and non-coated nanoparticles were measured by dynamic light scattering (DLS) utilizing the Zetasizer Nano ZS instrument (Malvern Ltd).

Zeta Potential

The zeta (ζ) potential of the membrane coated and non-coated nanoparticles were measured using the Zetasizer Nano ZS Instrument. Nanoparticles were loaded into a folded capillary cell (Malvern Ltd.) and zeta potential was determined based on the electrophoretic mobility of the nanoparticles.

Transmission Electron Microscopy

Nanoparticles were prepared for transmission electron microscopy (TEM) by placing a formvar-carbon coated grid in a Pelco easiGlow discharge machine. One drop of the nanoparticles was placed on the grid and left for 1 minute. Liquid was wicked off grid with filter paper. For negative staining, one drop of 1% uranyl acetate was added to the grid and left for 1 minute and then the liquid was wicked off with filter paper. Sample was imaged with the FEI Tecnai G2 Spirit Biotwin Transmission Electron Microscope.

Nanoparticle Uptake in C4-2B Cells

Flow cytometry was used to determine uptake of P-BiNP. PLGA nanoparticles were tagged with Nile red fluorescent dye and coated with membranes as described above. C4-2B cells or human fibroblast cells (HFF1 purchased from ATCC) were plated on six-well dishes at a density of 0.5 x 10^6 cells per well in triplicate and allowed to attach for 24 hours prior to being treated with either: BareNPs, BiNPs, or P-BiNPs for an hour. After incubation, cells were rewashed with PBS and then detached with trypsin. Cells were washed by centrifuging at 200 g for 10 min with 1% FBS diluted in PBS. Cells were fixed with 2% PFA for 15 minutes at 4 degrees C. Then 1% FBS in PBS was added to cells followed by centrifugation at 200 g for 10 min. Cells were resuspended in 1% FBS in PBS. Beckman Coulter Cytomics FC500 Flow Cytometry Analyzer was gated on red fluorescence channel to determine nanoparticle uptake.

Simultaneous uptake of cell membrane coating and nanoparticle core was additionally studied. C4-2B cells were plated on glass coverslips in six-well plates at density described above and allowed to attach for 24 hours. Nanoparticles were prepared by incorporating Nile red into the core PLGA as described above. Cancer cell membrane fraction was tagged with Pkh26 (Sigma Aldrich) per manufacturer's protocol prior to the first extrusion. Nanoparticles were added to cell culture media for 1 hour. Excess nanoparticles were washed out thrice with PBS. Cells were fixed with 4 % paraformaldehyde for 10 minutes, washed with PBS, then mounted on microscope slides with Prolong Gold anti-fade reagent with DAPI (Invitrogen). Cells were imaged with the Zeiss LSM 510 confocal microscope.

For spheroids generation, C4-2B and HFF-1 cell lines were combined at a 3:1 ratio and plated at $3x10^6$ cell/mL in Aggrewell 800 plates (Stem Cell Technologies) following manufacturer's instructions. Aggregates were allowed to form over 24 hrs in Aggrewells followed by 24 hrs in ultralow six-well plates on an orbital shaker. Resulting spheroids were incubated with BareNP or P-BiNP loaded with Nile Red dye for 3 hrs in a 1.5mL microcentrifuge tube at 37 degrees C and 5% CO2 with gentle shaking. Nanoparticles were removed from solution by washing spheroids and fixed in 4% paraformaldehyde for 30 minutes. Samples were washed in PBS, then in 100uL of 100% methanol incubation for 15 minutes. Samples were further processed by adding 20% DMSO in 100% methanol for 2 minutes and repeated, then 80% methanol in PBS for 2 minutes, 50% methanol in PBS for 2 minutes, PBS alone for 2 minutes twice, and finally twice in 1% TritonX-100 in PBS for 2 minutes. Samples were then placed in penetration buffer consisting of 0.2% Triton/0.3M glycine/ 20% DMSO in PBS for 15 minutes and blocked with 0.2% TritonX/6% donkey serum /10% DMSO in PBS at 37ºC with gentle shaking for 15 minutes. Spheroids were finally stained with DAPI and imaged on Keyence BZ-X700.

Cell Viability Assay

C4-2B cells were plated on 96 well flat bottom plates (Corning Incorporated Durham, NC) at a density of 2000 cells per well. Cells were allowed to attach for 24 hours then treated with increasing concentrations (0-20 ug/ml cabazitaxel loaded) BiNP or P-BiNP for 72 hours in standard cell culture conditions. At respective time points 20 μl Thiazolyl Blue Tetrazolium Bromide (MTT) (Sigma, St. Louis, MO) suspended in PBS at a concentration of 5mg/mL was added to the 96 well plate. After three hours of incubation, media was removed and 100 μl of DMSO was added to all wells and mixed by pipetting. Absorbance was read on BioTek Synergy

2 Multi-Mode Plate Reader (Winooski, VT) at 570 nm. Percentage cell viability was calculated by dividing absorbance of sample by the average of untreated cells in quadruplicate and then multiplied by one hundred.

In vivo bone homing

Male athymic nude-foxn1nu were injected intravenously with 100 ul of freshly prepared saline, dye, BiNP, or P-BiNP via lateral tail vein injection. Treatment groups were prepared as described above with incorporation of IR-780 dye (Sigma-Aldrich, USA) into the core of the nanoparticle (similar to described above encapsulation of Nile red into nanoparticle core) prior to coating or the equivalent concentration of dye used in dye only group to ensure consistency among groups. Two hours after injection mice were sacrificed and organs excised and NIR was imaged and quantified with Odyssey CLx (LI-COR, USA).

VII. SUPPLEMENTAL FIGURES

Supplemental 1:

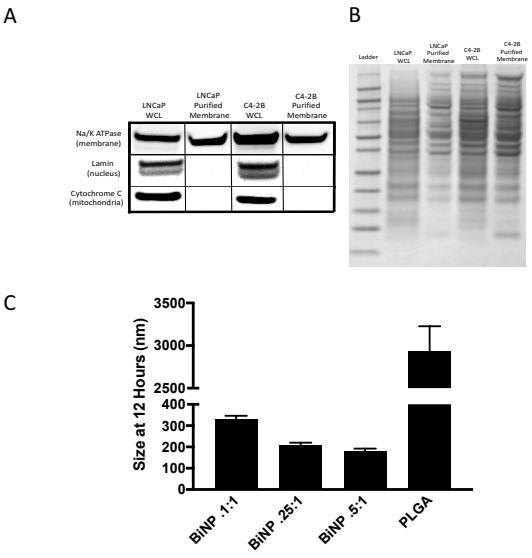

Figure 13: S1: Membrane fraction purification. **(A)** Western blot of LNCap and C4-2B cell lines were used to verify that purified membrane did not contain nuclear or mitochondrial components. **(B)** Coomassie blue stain used to verify purified membrane of both C4-2B and LNCaP cell lines retained a variety of membrane proteins. **(C)** PLGA nanoparticles were coated with different ratios of cell membrane to nanoparticle polymer to determine optimal amount of cell membrane coating needed to stabilize nanoparticles as measured through stability of size. Nanoparticles were placed in PBS solution and size was measured after 12 hours. An increase in size is indicative of aggregation. (WCL=whole cell lysate). (n=3). Mean ± SEM.

Supplemental 2:

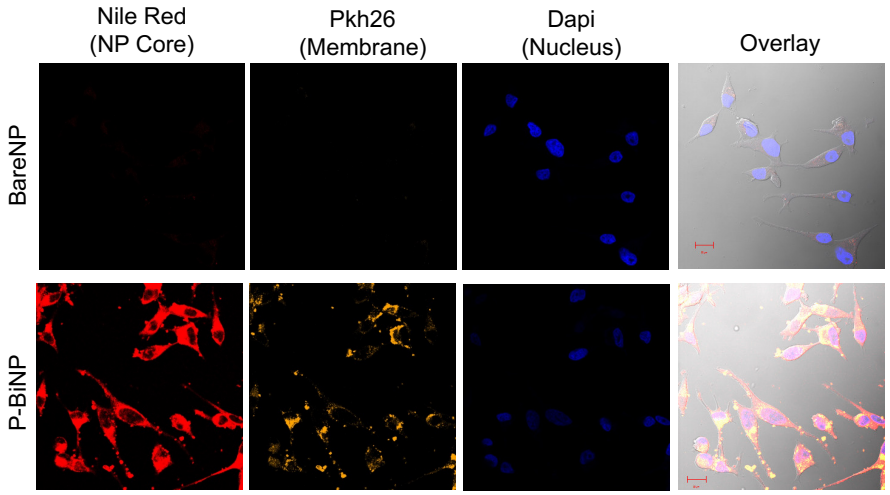

Figure 14: S2: Fluorescent microscopy of P-BiNP cellular uptake. Either BareNPs (top) or P-BiNP (bottom), both with cores labeled with nile red fluorescent dye were incubated in C4-2B cells. Additionally, during the preparation process, the lipid component of the cell membrane coating was tagged with Pkh26 dye in the P-BiNPs. There was increased simultaneous uptake of both the nanoparticle core and membrane coating of P-BiNPs in the prostate cancer cells. Blue=Dapi. Red=nile red in core of NPs. Yellow=Pkh26 label of lipid membrane coating.

Supplemental 3:

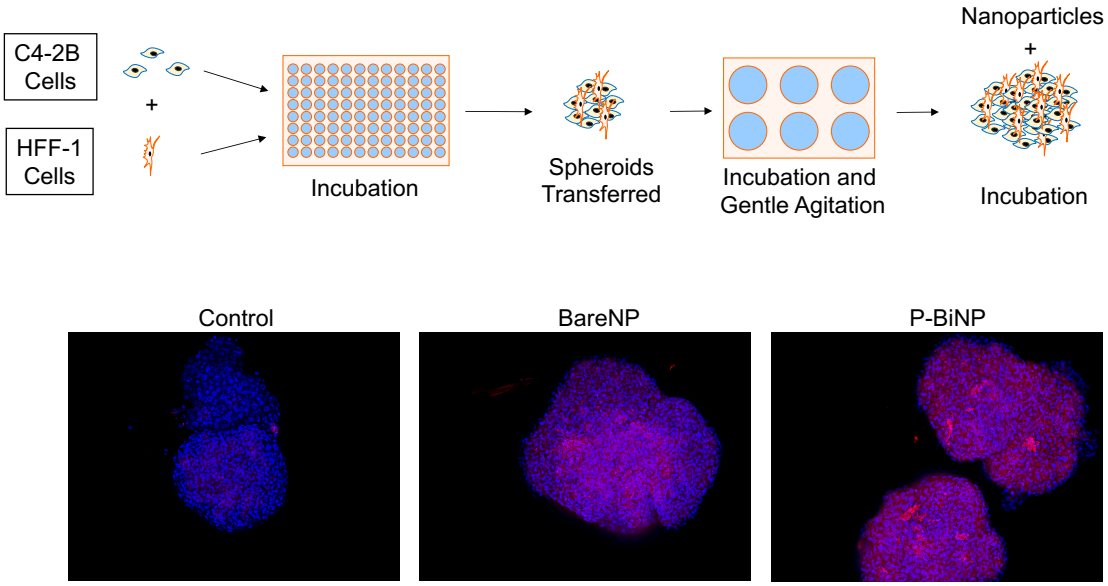

Figure 15: S3: Co-culture spheroid penetration assay. C4-2B (prostate cancer cells) and HFF-1 (fibroblasts) were co-cultured in non-adherent dish. After 3D spheroid formation, incubation was performed with either BareNP or P-BiNP, both labeled with nile red fluorescent dye. Confocal imaging showed P-BiNP were able to thoroughly penetrate spheroids after 3 hours of incubation. Blue=Dapi. Red=nile red in core of NPs.

VIII. REFERENCES

1. Danhier, F.; Feron, O.; Preat, V., To exploit the tumor microenvironment: Passive and active tumor targeting of nanocarriers for anti-cancer drug delivery. *J Control Release* 2010, *148* (2), 135-46.

2. Bertrand, N.; Wu, J.; Xu, X.; Kamaly, N.; Farokhzad, O. C., Cancer nanotechnology: the impact of passive and active targeting in the era of modern cancer biology. *Adv Drug Deliv Rev* 2014, *66*, 2-25.

3. Peer, D.; Karp, J. M.; Hong, S.; Farokhzad, O. C.; Margalit, R.; Langer, R., Nanocarriers as an emerging platform for cancer therapy. *Nature nanotechnology* 2007, *2* (12), 751-60.

4. Elias, D. R.; Poloukhtine, A.; Popik, V.; Tsourkas, A., Effect of ligand density, receptor density, and nanoparticle size on cell targeting. *Nanomedicine : nanotechnology, biology, and medicine* 2013, *9* (2), 194-201.

5. Marusyk, A.; Almendro, V.; Polyak, K., Intra-tumour heterogeneity: a looking glass for cancer? *Nature reviews. Cancer* 2012, *12* (5), 323-34.

6. Gdowski, A. S.; Ranjan, A.; Vishwanatha, J. K., Current concepts in bone metastasis, contemporary therapeutic strategies and ongoing clinical trials. *J Exp Clin Cancer Res* 2017, *36* (1), 108.

7. Hu, C. M.; Zhang, L.; Aryal, S.; Cheung, C.; Fang, R. H.; Zhang, L., Erythrocyte membrane-camouflaged polymeric nanoparticles as a biomimetic delivery platform. *Proceedings of the National Academy of Sciences of the United States of America* 2011, *108* (27), 10980-5.

8. Jin, J. K.; Dayyani, F.; Gallick, G. E., Steps in prostate cancer progression that lead to bone metastasis. *International journal of cancer* 2011, *128* (11), 2545-61.

9. Sun, Y. X.; Fang, M.; Wang, J.; Cooper, C. R.; Pienta, K. J.; Taichman, R. S., Expression and activation of alpha v beta 3 integrins by SDF-1/CXC12 increases the aggressiveness of prostate cancer cells. *The Prostate* 2007, *67* (1), 61-73.

10. Fang, R. H.; Hu, C. M.; Luk, B. T.; Gao, W.; Copp, J. A.; Tai, Y.; O'Connor, D. E.; Zhang, L., Cancer cell membrane-coated nanoparticles for anticancer vaccination and drug delivery. *Nano letters* 2014, *14* (4), 2181-8.

11. Glinsky, V. V.; Glinsky, G. V.; Glinskii, O. V.; Huxley, V. H.; Turk, J. R.; Mossine, V. V.; Deutscher, S. L.; Pienta, K. J.; Quinn, T. P., Intravascular metastatic cancer cell homotypic aggregation at the sites of primary attachment to the endothelium. *Cancer research* 2003, *63* (13), 3805-11.

12. Khaldoyanidi, S. K.; Glinsky, V. V.; Sikora, L.; Glinskii, A. B.; Mossine, V. V.; Quinn, T. P.; Glinsky, G. V.; Sriramarao, P., MDA-MB-435 human breast carcinoma cell homo- and heterotypic adhesion under flow conditions is mediated in part by Thomsen-Friedenreich antigen-galectin-3 interactions. *The Journal of biological chemistry* 2003, *278* (6), 4127-34.

13. Li, S. Y.; Cheng, H.; Xie, B. R.; Qiu, W. X.; Zeng, J. Y.; Li, C. X.; Wan, S. S.; Zhang, L.; Liu, W. L.; Zhang, X. Z., Cancer Cell Membrane Camouflaged Cascade Bioreactor for Cancer Targeted Starvation and Photodynamic Therapy. *ACS nano* 2017, *11* (7), 7006-7018.

14. Sarveswaran, S.; Ghosh, R.; Morisetty, S.; Ghosh, J., MK591, a second generation leukotriene biosynthesis inhibitor, prevents invasion and induces apoptosis in the bone-invading

C4-2B human prostate cancer cells: implications for the treatment of castration-resistant, bone-metastatic prostate cancer. *PloS one* 2015, *10* (4), e0122805.

15. Thalmann, G. N.; Anezinis, P. E.; Chang, S. M.; Zhau, H. E.; Kim, E. E.; Hopwood, V. L.; Pathak, S.; von Eschenbach, A. C.; Chung, L. W., Androgen-independent cancer progression and bone metastasis in the LNCaP model of human prostate cancer. *Cancer research* 1994, *54* (10), 2577-81.

16. Luk, B. T.; Hu, C. M.; Fang, R. H.; Dehaini, D.; Carpenter, C.; Gao, W.; Zhang, L., Interfacial interactions between natural RBC membranes and synthetic polymeric nanoparticles. *Nanoscale* 2014, *6* (5), 2730-7.

17. Hines, D. J.; Kaplan, D. L., Poly(lactic-co-glycolic) acid-controlled-release systems: experimental and modeling insights. *Critical reviews in therapeutic drug carrier systems* 2013, *30* (3), 257-76.

18. Zhu, J. Y.; Zheng, D. W.; Zhang, M. K.; Yu, W. Y.; Qiu, W. X.; Hu, J. J.; Feng, J.; Zhang, X. Z., Preferential Cancer Cell Self-Recognition and Tumor Self-Targeting by Coating Nanoparticles with Homotypic Cancer Cell Membranes. *Nano letters* 2016, *16* (9), 5895-901.

19. de Leeuw, R.; Berman-Booty, L. D.; Schiewer, M. J.; Ciment, S. J.; Den, R. B.; Dicker, A. P.; Kelly, W. K.; Trabulsi, E. J.; Lallas, C. D.; Gomella, L. G.; Knudsen, K. E., Novel actions of next-generation taxanes benefit advanced stages of prostate cancer. *Clinical cancer research : an official journal of the American Association for Cancer Research* 2015, *21* (4), 795-807.

20. Wong, N. C.; Mueller, B. M.; Barbas, C. F.; Ruminski, P.; Quaranta, V.; Lin, E. C.; Smith, J. W., Alphav integrins mediate adhesion and migration of breast carcinoma cell lines. *Clinical & experimental metastasis* 1998, *16* (1), 50-61.

21. van der, P.; Vloedgraven, H.; Papapoulos, S.; Lowick, C.; Grzesik, W.; Kerr, J.; Robey, P. G., Attachment characteristics and involvement of integrins in adhesion of breast cancer cell lines to extracellular bone matrix components. *Laboratory investigation; a journal of technical methods and pathology* 1997, *77* (6), 665-75.

22. Sung, V.; Stubbs, J. T., 3rd; Fisher, L.; Aaron, A. D.; Thompson, E. W., Bone sialoprotein supports breast cancer cell adhesion proliferation and migration through differential usage of the alpha(v)beta3 and alpha(v)beta5 integrins. *Journal of cellular physiology* 1998, *176* (3), 482-94.

23. Noti, J. D., Adherence to osteopontin via alphavbeta3 suppresses phorbol ester-mediated apoptosis in MCF-7 breast cancer cells that overexpress protein kinase C-alpha. *International journal of oncology* 2000, *17* (6), 1237-43.

CHAPTER IV

ADDITIONAL NANOPARTICLE SYNTHESIS METHOD:

OPTIMIZATION AND SCALE UP OF MICROFLUIDIC NANOLIPOMER PRODUCTION METHOD FOR PRECLINICAL AND POTENTIAL CLINICAL TRIALS

I. ABSTRACT

Background: The process of optimization and fabrication of nanoparticle synthesis for preclinical studies can be challenging and time consuming. Traditional small scale laboratory synthesis techniques suffer from batch to batch variability. Additionally, the parameters used in the original formulation must be re-optimized due to differences in fabrication techniques for clinical production. Several low flow microfluidic synthesis processes have been reported in recent years for developing nanoparticles that are a hybrid between polymeric nanoparticles and liposomes. However, use of high flow microfluidic synthetic techniques has not been described for this type of nanoparticle system, which we will term as nanolipomer. In this manuscript, we describe the successful optimization and functional assessment of nanolipomers fabricated using a microfluidic synthesis method under high flow parameters.

Results: The optimal total flow rate for synthesis of these nanolipomers was found to be 12 ml/min and flow rate ratio 1:1 (organic phase: aqueous phase). The PLGA polymer concentration of 10 mg/ml and a DSPE-PEG lipid concentration of 10% w/v provided optimal size, PDI and stability. Drug loading and encapsulation of a representative hydrophobic small molecule drug, curcumin, was optimized and found that high encapsulation efficiency of 58.8% and drug loading of 4.4% was achieved at 7.5% w/w initial concentration of curcumin/ PLGA polymer. The final size and polydispersity index of the optimized nanolipomer was 102.11 nm and 0.126, respectively. Functional assessment of uptake of the nanolipomers in C4-2B prostate cancer cells showed uptake at 1 hour and increased uptake at 24 hours. The nanolipomer was more effective in the cell viability assay compared to free drug. Finally, assessment of *in vivo* retention in mice of these nanolipomers revealed retention for up to 2 hours and were completely cleared at 24 hours.

Conclusions: In this study, we have demonstrated that a nanolipomer formulation can be successfully synthesized and easily scaled up through a high flow microfluidic system with optimal characteristics. The process of developing nanolipomers using this methodology is significant as the same optimized parameters used for small batches could be translated into manufacturing large scale batches for clinical trials through parallel flow systems.

II. INTRODUCTION

Many anti-cancer therapeutics are hydrophobic small molecule drugs and must be formulated appropriately so that it will achieve suitable bioavailability when administered systemically[1]. Formulating such nanosystems can be tedious and pose many challenges at both the preclinical and clinical stages of drug development[2] using conventional scale-up processes. The major limitation occurs when transitioning from preclinical formulations to scaling up production for the purposes of clinical trials[3]. This requires a large amount of time and resources. In recent years, microfluidic nanoparticle synthesis strategies have been developed with the goal of providing a successful approach to scale up the nanoparticle synthesis process in a reliable and reproducible manner. Utilizing microfluidics allows for the same parameters used in small scale batches to be applied in parallel during the scale up process[4]. Microfluidics has the possibility to become widely used as the processes are economical, reproducible and amenable to modifications. Further, this can be integrated with many other processes or technologies[5].

Microfluidic devices allow for control over the mixing time by varying solvent flow rates or channel geometry. Moreover, better heat transfer owing to large surface areas enables better

temperature control, preventing the formation of large temperature gradients. Finally, as the channel length directly corresponds to the time taken by the reactants to flow through it in continuous flow synthesis, the reaction time can be controlled by tuning the channel length or by adding reagents at precise downstream locations during the particle formation process to quench the reaction[6].

It was our goal in the manuscript to determine if a high flow microfluidic process could be used to synthesize a nanoparticle formulation composed of poly (lactic-co-glycolic acid) (PLGA) and lipid surface coating consisting of DSPE-PEG, which we will refer to as a nanolipomer (NLP). Previous attempts have utilized high flow rates for making various formulations of either liposomes or nanoparticles[7-9]. However, hybrid formulations utilizing a core polymeric nanoparticle with a lipid coating for stabilization have only been made at low flow rates[5, 10]. These low flow rates achieve stable and effective nanoparticle formulations but it is uncertain how increasing the flow rate to greater than 1000 times previously reported rates will affect these nanolipomers.

In our system, the herringbone pattern incorporated into the microfluidic channel allows for adequate mixing and coating of the DSPE-PEG onto the polymeric nanoparticle at a high flow rate. The optimization of this formulation proceeded with adjustment of instrument flow settings. Next, formulation parameters were optimized that included polymer concentration, lipid coating concentration, as well as drug concentration (Figure 16). After the nanolipomer was optimized for size, polydispersity, and drug encapsulation parameters, we performed functional assessments that included both *in vitro* and *in vivo* studies using a murine model.

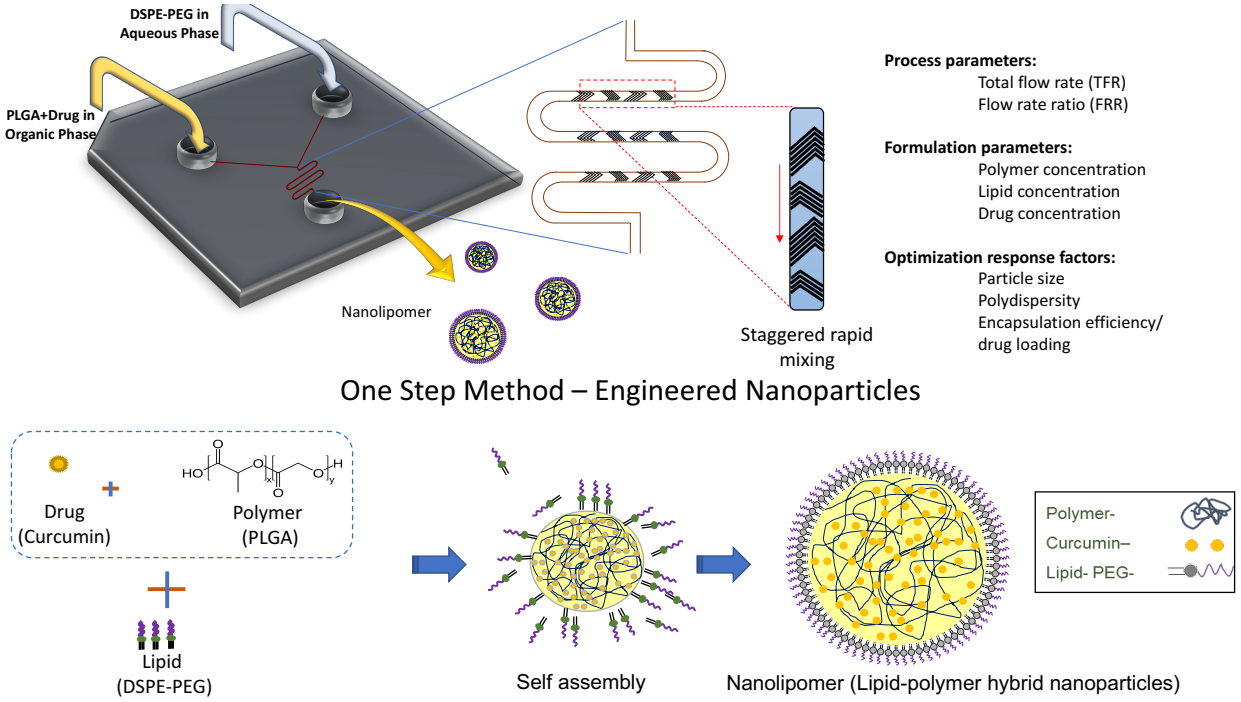

Figure 16: Schematic diagram of synthesis process. Staggered herringbone based microfluidic chip for synthesizing the nanolipomer nanoparticles. The PLGA + drug core is formed by nano-precipitation in the microfluidic chip and introduced from one inlet while the DSPE-PEG lipid coating is injected from the opposite port. The final nanolipomer is collected in the third port after rapid mixing has occurred.

III. RESULTS

Self-assembly of nanolipomers by microfluidic synthesis

The instrument parameters were focused on first. Analysis of the effects of adjusting the total flow rate (TFR) showed that increasing TFR impacted the size of the NLPs, particularly at the low (5 mg/ml) and high (20 mg/ml) initial polymer concentrations showed that as the TFR was increased from 2 ml/min to 6 ml/min there was a significant increase in size of the NLP. Further, increase in TFR from 6 ml/min to 12 ml/min does not have a significant difference in the size of the NLPs. We found minimal change in the nanoparticle size and concentration at the midrange initial polymer range (10 and 15 mg/ml) across the different total flow groups. As expected, we found that in each flow rate group the size of the nanoparticles increased as the PLGA concentration increased. Since the 10 mg/ml concentration of PLGA nanoparticles were stable with low size and PDI at a total flow rate of 12 ml/min, we selected this as the optimal total flow rate (Figure 17).

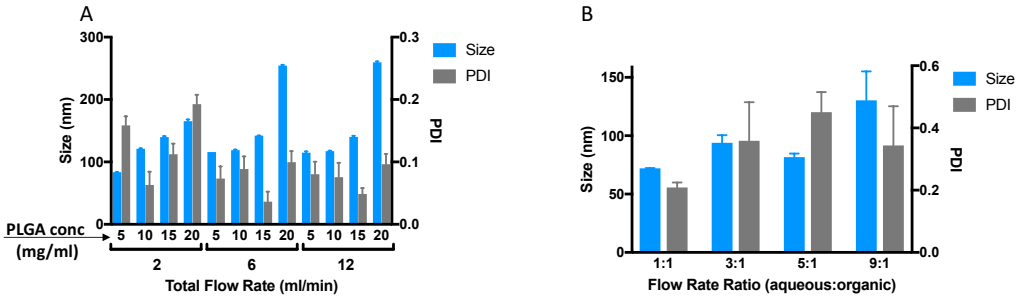

Figure 17: Instrument parameters optimization (A) Effect of total flow rate (TFR) on the size and polydispersity (PDI) of the nanolipomers at polymer concentration of 5, 10, 15, & 20 mg/ mL (DSPE-PEG concentration = 40%, aqueous:solvent FRR = 1:1) **(B)** Effect of aqueous:solvent flow rate ratio (FRR) on the size and polydispersity (PDI) of nanolipomers at polymer concentration of 10 mg/ mL (DSPE-PEG concentration = 40%, TFR = 12 ml/min). (n=3: mean± SD).

Next, the flow rate ratio (FRR) of aqueous solution to organic solvent was determined. The FRR of 1:1 aqueous solution to organic solvent created uniform and small nanoparticles with average size 72 nm and PDI of .209. The higher flow rate ratios that were tested yielded NLPs larger in size with a higher PDI (Figure 17).

After the instrument parameters were optimized, attention was turned to optimizing the initial polymer concentrations and lipid coating. Polymer concentration consisting of 5, 10, 20 mg/ml in acetonitrile was tested against an initial concentration of DSPE-PEG at 0, 5, and 10% w/w. When no DSPE-PEG is used (0%) for stabilizing the NLPs, the size is increased, likely due to aggregation. As the DSPE-PEG is introduced at 5% and 10% the particle size stabilizes and size remains small. The 10% DSPE-PEG and 10 mg/mL achieved combination of small nanoparticle size (mean=112.2 nm, SD 5.24) with low PDI (mean=0.129, SD 0.01) (Figure 18). These values were used for the final parameter before the drug encapsulation optimization.

NLPs showed stability when stored at 4 degree Celsius over a period of 7 days. There was minimal fluctuation of both size and polydispersity of this formulation (Figure18).

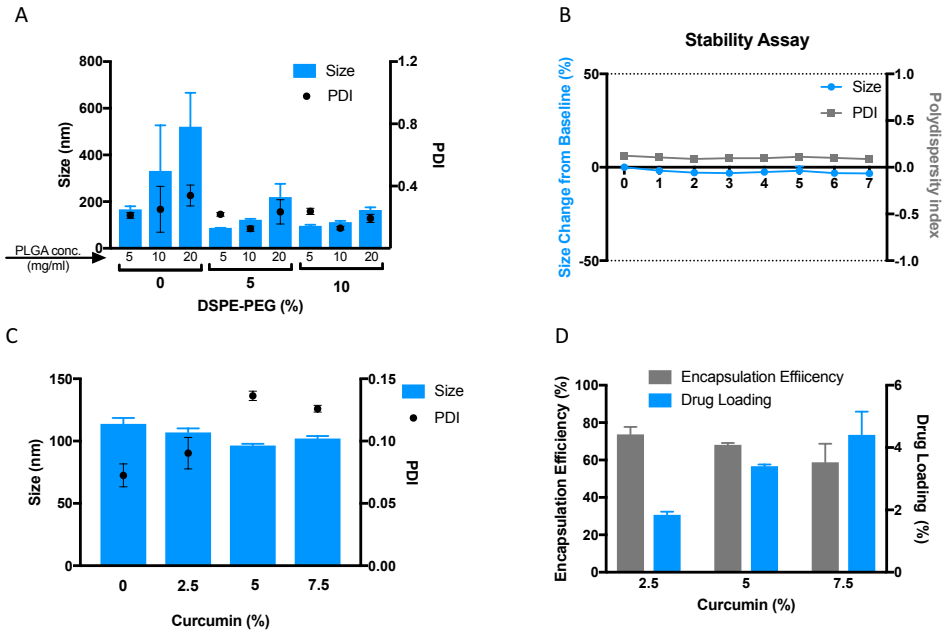

Figure 18: Nanolipomer formulation parameters (A) Effect of PLGA and DSPE-PEG concentration on the size and PDI of nanolipomers **(B)** Nanolipomer stability assay at 4 degrees Celsius over one week **(C)** Effect of initial curcumin concentration on size and PDI **(D)** Curcumin encapsulation efficiency and drug loading at various initial concentrations of curcumin. (n=3: mean± SD).

Efficient drug loading using microfluidic synthesis

The size of the NLP was stable as the amount of curcumin used in the initial concentration was increased from 0% to 7.5%. The PDI slightly increased at the 5% (0.136) and 7.5% (0.126) curcumin concentrations compared to the 0% (0.073) and 2.5% (.090). The encapsulation efficiency at 2.5% initial curcumin was approximately 73.68% and it decreased in a linear fashion to approximately 58.79% at the highest concentration of initial curcumin which was 7.5% w/w.

Drug loading peaked at the highest concentration of initial curcumin (7.5%) for this method at 4.41% (Figure 18).

NLP fluorescent characterization

The absorption spectra of curcumin and loaded nanolipomers have similar peaks at 424 nm. The NLP absorption spectrum is more structured and narrow after correction for scattering. For steady state emission, the NLPs exhibit a blue shift of approximately 40 nm compared to free curcumin. Time resolved lifetime measurements show that the lifetime of curcumin nearly doubles from 0.29 ns to 0.64 ns when packed within NLPs. Time resolved anisotropy show a higher anisotropy of 0.23 ns for NLPs as compared to 0.18 ns for curcumin alone. This could be on account of a more rigid environment in NLPs due to packing of curcumin molecules (Figure 19).

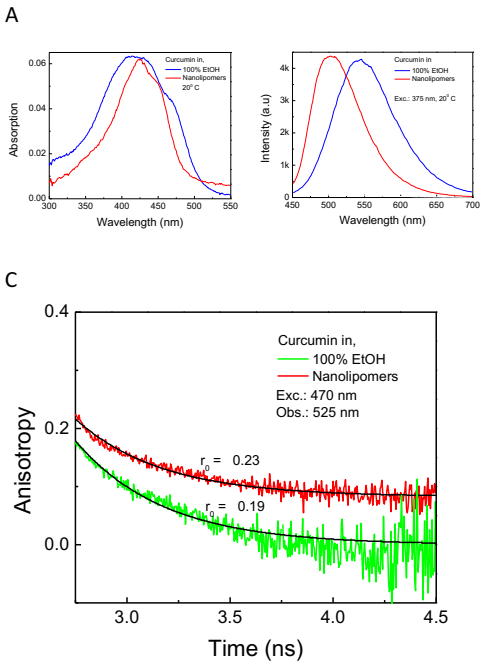

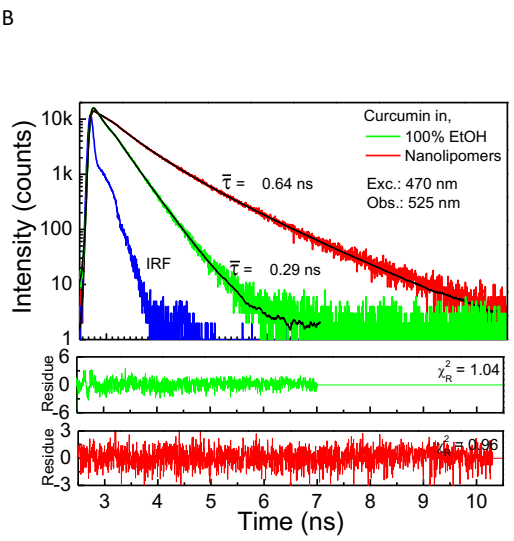

Figure 19: Fluorescence measurements of nanolipomers (A) Absorption spectrum of curcumin and nanolipomers after curcumin encapsulation **(B)** Time resolved lifetime measurements of curcumin vs nanolipomers **(C)** Time resolved anisotropy measurements of curcumin vs nanolipomers.

Nanolipomers are effective in *in vitro* functional assays

Hybrid nanoparticles were verified to have substantial uptake in the C4-2B prostate cancer cell line. The uptake was followed at 2 time points (1 hour and 24 hours) and shown to have increased uptake at 24 hour time point as measured through confocal microscopy (Figure 20).

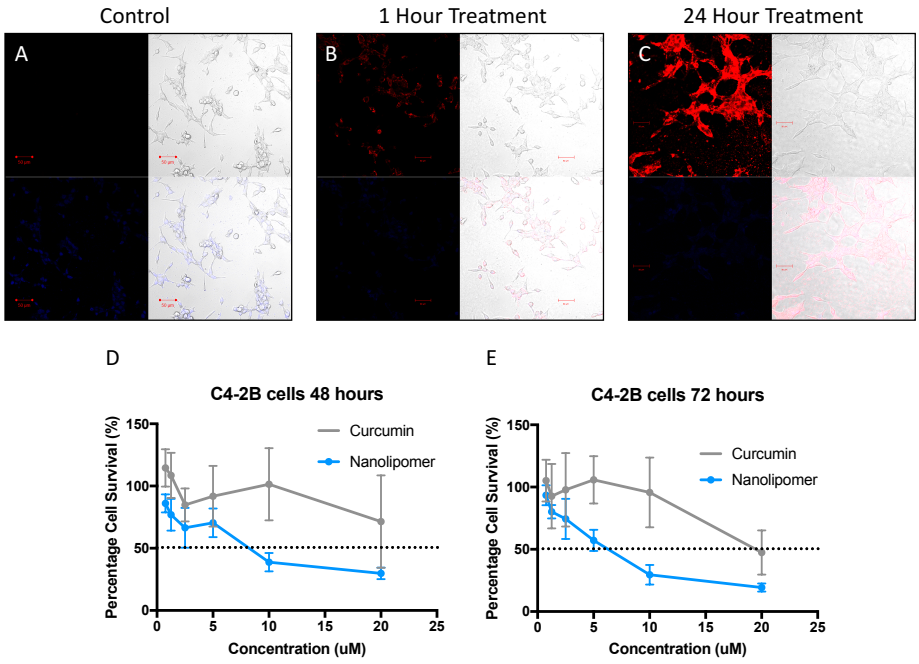

Figure 20: *In vitro* functional assessment of nanolipomers (A-C) C4-2B prostate cancer cell uptake experiment at 1 hour and 24 hours **(D)** Cell viability of C4-2B cells after 48 hours of treatment **(E)** Cell viability of C4-2B cells after 72 hours of treatment (n=3: mean± SD).

In the MTT cell viability assay, the synthesized NLPs were more effective at treating C4-2B cells than the free curcumin at equivalent concentration. This increased effectiveness was true at both the 48 and 72 hour time points. The concentration at which the NLPs inhibited 50% of cell viability was considered the IC_{50} of the NLPs. At 48 hours the IC_{50} was ~8.45 uM while the free curcumin at the 48-hour time point didn't achieve an IC_{50} at the highest concentration tested. At 72 hours the IC_{50} of the NLPs was found to be more effective at 6.5 uM, while the IC_{50} of the curcumin was 19.89 uM (Figure 20).

NLP coating allows for adequate *in vivo* retention

NLPs were assessed for their retention in a murine system. We found that the NLPs exhibited relatively stable fluorescent signal during the period from 25 minutes to 2 hours after tail vein injection. At 24 hours, both the NLP nanoparticles had been completed removed from the system (Figure 21).

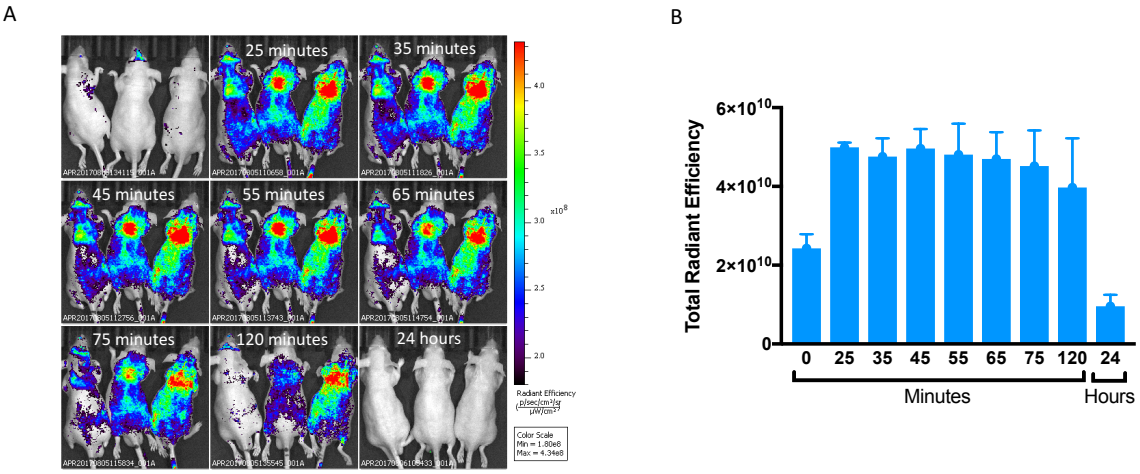

Figure 21: *In vivo* nanolipomer retention assay. (A) Live animal imaging at various time points after tail vein injection of fluorescently labeled nanolipomer **(B)** Quantification of fluorescent signal at various time points. (n=3: mean± SD).

IV. DISCUSSION

In this paper, we have demonstrated the ease and scalability of utilizing a microfluidics system to synthesize nanolipomers. Others have reported the use of microfluidic systems for fabrication of nanoparticles and liposomes with various stabilizer coatings at high flow rates[7-9, 12]. However, it has not been demonstrated whether using high flow rates could achieve stable and adequate nanoparticle coating of DSPE-PEG onto PLGA nanoparticles. Utilizing this hybrid concept of PLGA polymeric nanoparticles with a DSPE-PEG lipid coating allows us to combine the advantageous properties of both PLGA nanoparticles and DSPE-PEG[13]. The polymeric

nanoparticle provides stable controlled release drug kinetics[14]. The addition of DSPE-PEG allows for decreased protein absorption on the surface of the nanoparticle and a longer circulation time[13].

The optimization strategy that was employed for this project proceeded in an orderly stepwise fashion focusing on two principle components. The parameters intrinsic to the instrument itself were the first components and the variables within the formulation were the second components. The instrument parameters included the total flow rate and flow rate ratio. We based our optimization on the highly desirable nanoparticle product characteristics, small size and low polydispersity. To this point, we found that when total flow rate was increased from 2 ml/min to 12 ml/min, there was little change in the NLP size or polydispersity at the polymer concentration in the mid-range that was tested (10 mg/ml and 15 mg/ml). However, there was an increase in size between the flow rates at the lowest concentration of polymer used (5 mg/ml) and the highest concentration of polymer used (20 mg/ml). The overarching goal of this project was to maximize NLP production while maintaining acceptable characteristics so the total flow rate of 12 ml/min was chosen for the remaining experiments. The microfluidic synthesis process and coating with DSPE-PEG onto polymeric nanoparticles has previously only been reported successful at low flow rates on the order of ul/min [5, 10]. To reduce production times, higher flow rates must be tested and validated for these types of hybrid nanoparticles.

The next aspect of the instrument to be optimized was the flow rate ratio of aqueous phase to organic phase. When increasing this ratio, there was an increase in both size and PDI of the NLP.

The shift in the polarity of the solution when rapidly mixing the aqueous and organic phases together results in a supersaturation of hydrophobic molecules in a new solvent and thus causes the precipitation resulting in formation of the PLGA nanoparticle with a small size [15]. However, the PLGA nanoparticles must be stabilized with DSPE-PEG to prevent the nanoparticles from aggregating once they are formed. The change in polarity felt by the amphiphilic DSPE-PEG is less and this lower driving force of the DSPE-PEG to arrange on the hydrophobic PLGA core results in larger core nanoparticles as the flow rate ratio increased. We found the best balance between these two factors to be at the 1:1 flow rate ratio.

The next phase was to optimize the formulation parameters. The three parameters to be optimized were the concentrations of: DSPE-PEG, PLGA polymer, and initial drug used. These parameters could be rapidly optimized due to the ease of manufacturing with the microfluidic system. It was found that as the concentration of PLGA was increased, the nanoparticle size increased. This is likely due to the increase in viscosity of the organic phase that occurs with the increased concentration of polymer. This increased viscosity lowers the diffusion speed of the polymer while mixing and results in larger particles. In addition, as the DSPE-PEG concentration was increased from 5% to 10% we found slight benefits in terms of size and PDI and also found that the particles were most stable in phosphate buffered saline at the 10% concentration (data not shown). Thus DSPE-PEG concentration of 10% was chosen. Further, these particles were stable over the course of 7 days with minimal fluctuation in size and PDI when suspended in water.

In this process, curcumin was chosen as a representative drug for encapsulation within the nanolipomer. Curcumin is hydrophobic and thus serves as an illustrative molecule for many anti-cancer agents[16]. In addition, curcumin is fluorescent so determining its encapsulation within the nanolipomer is also relatively simple[17]. We found this process resulted in a high encapsulation efficiency (58.8%) and drug loading (4.4%) when the initial concentration of curcumin was set at 7.5% w/w polymer. Time resolved lifetime measurements show that the lifetime of curcumin nearly doubles when packed within nanoparticles. This is important in the context of imaging and drug tracking as fluorophores with shorter fluorescent lifetimes are characteristic of weak emitters. By increasing the lifetime and anisotropy of the molecule after encapsulation in nanolipomers, it reconfirms that the curcumin is encapsulated within the nanoparticle and also improves the ability to track the curcumin during *in vitro* and *in vivo* experimentation[18].

The DSPE-PEG lipid coating of these nanolipomers has been reported to allow for a more biocompatible formulation and improved cancer cell uptake[19]. We found that these NLPs had increased at 24 hours compared to 1 hour of treatment. This increased uptake over a longer course of time was evident in the results of the MTT cell viability assay. It was found that treatment with the NLP in prostate cancer cell line C4-2B had a lower IC_{50} value at the 72-hour time point than the 48 hour time point, indicating improved efficacy at 72 hours. Additionally, the NLP was more effective at reducing the prostate cancer cell viability at both the 48 hour and 72 hour times points compared to the equivalent dose of free curcumin.

The NLP formulation was fluorescently labeled and administered in a mouse model to determine the length of time these NLPs were retained after systemic injection. It was found that the NLP was retained in the system and provided a stable signal for up to 2 hours after injection. At the 24-hour time point after injection the NLP had been cleared.

At the flow rates used in this project, we have estimated the amount of nanopliomer product that could be fabricated. We calculated that it was feasible for one person completing the nanolipomer synthesis, as described, could easily make 14.4 grams of product at the flow rate of 12 ml/min during one day.

Table 3. NLP production estimate

Polymer Concentration (mg/ml)	**10 mg/ml**	**10 mg/ml**	**10 mg/ml**
Total Flow Rate (ml/min)	2	6	12
Production Rate (g/day)	2.4	7.2	14.4

Table 3: Based on an initial concentration of PLGA at 10 mg/ml and total flow rates ranging from 2-12 ml/min, the estimated production rate of product was calculated based on the feasibility for a single operator during one day.

V. CONCLUSION

In this study, we have demonstrated a successful one–step microfluidic process for facilitating the manufacturing and scaling up of nanolipomers. Prior attempts at producing these nanolipomers were burdened by low flow rates, low batch yield, inconsistencies between batches, and difficultly scaling the manufacturing process to make amounts that could be used on the clinical scale. This method provides a simple way to scale up optimization of small batch production techniques that can be used to translate into larger quantities while retaining the same beneficial properties that make nanolipomer nanoparticles of value. The successful scaling up of nanoparticle systems using microfluidics can lead to faster clinical approval possibilities thereby addressing the major limitation that hinders successful translation of these nanotherapeutics to reach patients.

VI. MATERIALS AND METHODS

Chemicals

PLGA ester-terminated (lactide to glycolide ratio 50:50, molecular weight 45,000 - 55,000), Nile Red dye, acetonitrile HPLC grade 99.93%, and curcumin were obtained from Sigma-Aldrich (St Louis, MO). 1,2-distearoyl-sn-glycero-3-phosphoethanolamine-N-[amino(polyethylene glycol)-2000] (ammonium salt) (DSPE-PEG (2000) Amine (2790.486 (average MW due to polydispersity of PEG) was purchased from Avanti (Alabaster, Alabama). Roswell Park Memorial Institute (RPMI) 1640 medium, fetal bovine serum, and penicillin/streptomycin were purchased from Hyclone. MilliQ water (Millipore) was used for all experiments.

Microfluidic production of nanolipomer nanoparticles

The basis of the microfluidic synthesis strategy reported in this manuscript utilizes addition of reagents at two inlet ports. One port with the aqueous phase which contains a lipid/stabilizing component. The second port with the organic phase contains polymer and drug. When these channels combine, a nanoprecipitation reaction occurs and rapid mixing in milliseconds[11] allows for coating the lipid/stabilizing agent onto the polymeric nanoparticle core. Overall, this process allows for high flow rates.

All optimization experiments were conducted using the NanoAssemblr Benchtop instrument (manufactured by Precision Nanosystems). PLGA nanoparticles were synthesized by dissolving PLGA +/- curcumin in acetonitrile at varying concentrations, this organic solvent mixture was injected in one inlet port in the system. Simultaneously, the DSPE-PEG (at varying concentrations) in 4% ethanol mixture was injected in the other inlet port of the system. Immediately prior to inlet port injection of the DSPE-PEG solution, it was heated in a water bath at 60 degrees C for 30 seconds.

Instrument parameters optimization

This was achieved by manipulating control of Total Flow Rate (TFR) 2-12 ml/min at PLGA concentrations 5-20 mg/ml and DSPE-PEG concentration of 40% w/w. Next, Flow Rate Ratios of aqueous:solvent (1:1) through (9:1) with 10 mg/mL PLGA in acetonitrile and 40% DSPE-PEG in 4% ethanol while TFR was held at 12 ml/min. NP product was gathered in 15 ml falcon tube while separately disposing the initial volume of 0.25 ml and the final 0.05 ml of NP solution. After the

nanolipomer (NLPs) were manufactured, they were processed to remove the aceteonitrile with a solvent exchange method to water in which NLPs were diluted and centrifuged thrice at 1600 g for 30 minute runs in Amicon Ultra Centrifugal Filters 10,000 NMWL. The NLP size and distribution were tested in distilled water and PBS with the Malvern Zetasizer ZS instrument.

Optimization of NLP formulation parameters

PLGA and DSPE-PEG parameters were optimized with polymer concentration 5, 10, and 20 mg/ml and lipid concentrations of 0, 5, and 10% w/w. This was followed by solvent exchange and determination of size and polydispersity as described above.

After determination of optimized formulation parameters to this point, the encapsulation of curcumin was performed. Curcumin was dissolved in 10 mg/ml of PLGA in acetonitrile so initial concentration of curcumin was varied between 0 - 7.5% curcumin w/w polymer. 10% DSPE-PEG w/w of lipid to polymer ratio was used with a TFR of 12 ml/min and a flow rate ratio (FRR) of 1:1 (aqueous channel input to organic channel input). Solvent exchange to remove non-encapsulated curcumin was performed and the amount of encapsulated curcumin was quantified by UV-Vis plate reader against a standard curve of curcumin in acetonitrile using absorbance at wavelength of 450 nm.

Drug loading and encapsulation efficiency were determined for the different initial concentrations of curcumin. Encapsulation Efficiency (EE) was calculated using the following equation: EE =

(actual amount of drug encapsulated in nanoparticles) / (starting amount of drug used in nanoparticles) x 100%. Drug loading (DL) was calculated with the equation: DL= (weight of drug in nanoparticles) / (weight of nanoparticles) x 100%.

NLP stability was assessed by incubating 100 ul of 10 mg/ml NLP formulation into 1 ml of molecular biology reagent water (Sigma-Aldrich). Nanoparticles were stored at 4 degrees Celsius then size and PDI were measured daily for a period of 7 days.

Fluorescent Characterization Studies

Time-Resolved Measurements

Fluorescence lifetime and anisotropy decay were measured using FluoTime200 (PicoQuant,GmbH, Berlin, Germany) time domain fluorometer. This instrument, equipped with microchannel plate detector (Hamamatsu, Japan) and a 470 nm pulsed picosecond laser diode provided resolution of 4ps/channel. The fluorescence lifetime of curcumin-loaded NP was measured at magic angle conditions and data were analyzed with a FluoFit version 5.0 software (PicoQuant,GmbH, Berlin, Germany). The lifetime data were fitted to the multi-exponential deconvolution model:

$$I(t) = \int_{-\infty}^{t} IRF(t') \sum_{i} \alpha_i e^{\frac{-t-t'}{\tau_i}}$$

where $IRF(t')$ represents the instrument response function at time t', τ_i is the lifetime of the ith component, and α_i is the amplitude of decay of the ith component at time t. The average values were calculated as:

$$\bar{\tau} = \sum_i f_i \tau_i \qquad f_i = \frac{\alpha_i \tau_i}{\sum_i \alpha_i \tau_i}$$

The anisotropy decays were measured using VV and VH polarizer orientation on the emission side with a 470nm laser diode. Anisotropy decays were analyzed with multi-exponential fitting model in FluoFit3 program from PicoQuant, Inc (Germany) using following equation.

$$r(t) = \sum_i r_i e^{-t/\Phi_i}$$

Steady-State Measurements

All measurements were performed in a 1cm x 1cm quartz cuvette at room temperature (20^0C). On account of poor water solubility, Curcumin dissolved in 100% ethanol was used as a reference. The nanoparticles were easily dissolved in water. Absorption spectra were collected on a Cary 50 Bio UV-visible spectrophotometer (Varian Inc., Australia). The absorption was scanned from 300-500 nm and water was used as a baseline reference. Emission spectra were measured using Cary Eclipse spectrofluorometer (Varian Inc., Australia). The samples were excited at 375 nm, and the emission scanned from 450-700 nm in a square geometry set-up.

Cell viability assay

Prostate cancer cell line C4-2B-luciferase was used to assess cell viability after treatment with NLP or free curcumin. C4-2B-luciferase cells were generously provided by Dr. Even Keller (University of Michigan). Cells were grown in RPMI-Media supplemented with 10% FBS and 1% antibiotic-antimycotic. Upon reaching 70% confluency, cells were subcultured and plated on 96 well flat bottom plates at a seeding density of 2000 cells per well in quadruplicate with the same culture conditions as described above. Cells were allowed to attach for 24 hours, media was replaced with fresh media and then cells were treated with NLPs or free drug for a period of either 48, or 72 hours with concentration range 0-20 uM curcumin or equivalent dose of NLP. At respective time points, 10 ul Tiazolyl Blue Tetrazolium Bromide (MTT) suspended in PBS at a concentration of 10.5 mg/mL was added to the 200 ul media in each 96 well plate. Cells were incubated with MTT reagent for 3 hours, media was then removed and 150 ul of DMSO was added to all wells and mixed. Absorbance was read on BioTek Synergy 2 Multi-Mode Plate Reader at 570 nm.

Cellular uptake studies

C4-2B-luciferase cells were plated on glass cover slips in 6 well plates at a density of 0.5 x 10^6 cells per well and attachment allowed for 24 hours. During NLP synthesis step, Nile Red dye was incorporated into PLGA core and excess dye washed out of the formulation. NLP was added to cell culture media at a concentration of 200 ug/ml for 0-6 hour time points and at appropriate time washed three times with PBS to remove NLP that was not taken up by cells. Cells were fixed with

4 % paraformaldehyde for 10 minutes, washed, then mounted on slides with Prolong Gold antifade reagent with DAPI. Imaging was performed with the Zeiss LSM 510 confocal microscope.

NLP retention study

To determine *in vivo* retention time of NLP, Nile red was incorporated into the NLP formulation as described above. Male nude mice aged 5 weeks were injected via tail vein with 2 mg of final NLP formulation. Fluorescent signal after injection was monitored between 25 minutes and 24 hours using the IVIS animal imaging system (Perkin Elmer, USA). All institutional IACUC animal protocols were followed.

VII. REFERENCES

1. Vrignaud S, Benoit JP, Saulnier P: Strategies for the nanoencapsulation of hydrophilic molecules in polymer-based nanoparticles. *Biomaterials* 2011, 32(33):8593-8604.

2. Desai N: Challenges in development of nanoparticle-based therapeutics. *The AAPS journal* 2012, 14(2):282-295.

3. Paliwal R, Babu RJ, Palakurthi S: Nanomedicine scale-up technologies: feasibilities and challenges. *AAPS PharmSciTech* 2014, 15(6):1527-1534.

4. Garg S, Heuck G, Ip S, Ramsay E: Microfluidics: a transformational tool for nanomedicine development and production. *Journal of drug targeting* 2016, 24(9):821-835.

5. Valencia PM, Pridgen EM, Rhee M, Langer R, Farokhzad OC, Karnik R: Microfluidic platform for combinatorial synthesis and optimization of targeted nanoparticles for cancer therapy. *ACS nano* 2013, 7(12):10671-10680.

6. DeMello AJ: Control and detection of chemical reactions in microfluidic systems. *Nature* 2006, 442(7101):394-402.

7. Guimaraes Sa Correia M, Briuglia ML, Niosi F, Lamprou DA: Microfluidic manufacturing of phospholipid nanoparticles: Stability, encapsulation efficacy, and drug release. *International journal of pharmaceutics* 2017, 516(1-2):91-99.

8. Yanagi T, Tachikawa K, Wilkie-Grantham R, Hishiki A, Nagai K, Toyonaga E, Chivukula P, Matsuzawa S: Lipid Nanoparticle-mediated siRNA Transfer Against

PCTAIRE1/PCTK1/Cdk16 Inhibits In Vivo Cancer Growth. *Molecular therapy Nucleic acids* 2016, 5(6):e327.

9. Li B, Luo X, Deng B, Wang J, McComb DW, Shi Y, Gaensler KM, Tan X, Dunn AL, Kerlin BA *et al*: An Orthogonal Array Optimization of Lipid-like Nanoparticles for mRNA Delivery in Vivo. *Nano letters* 2015, 15(12):8099-8107.

10. Zhang L, Feng Q, Wang J, Zhang S, Ding B, Wei Y, Dong M, Ryu JY, Yoon TY, Shi X *et al*: Microfluidic Synthesis of Hybrid Nanoparticles with Controlled Lipid Layers: Understanding Flexibility-Regulated Cell-Nanoparticle Interaction. *ACS nano* 2015, 9(10):9912-9921.

11. Zhigaltsev IV, Belliveau N, Hafez I, Leung AK, Huft J, Hansen C, Cullis PR: Bottom-up design and synthesis of limit size lipid nanoparticle systems with aqueous and triglyceride cores using millisecond microfluidic mixing. *Langmuir : the ACS journal of surfaces and colloids* 2012, 28(7):3633-3640.

12. Karnik R, Gu F, Basto P, Cannizzaro C, Dean L, Kyei-Manu W, Langer R, Farokhzad OC: Microfluidic platform for controlled synthesis of polymeric nanoparticles. *Nano letters* 2008, 8(9):2906-2912.

13. Zhang L, Chan JM, Gu FX, Rhee JW, Wang AZ, Radovic-Moreno AF, Alexis F, Langer R, Farokhzad OC: Self-assembled lipid--polymer hybrid nanoparticles: a robust drug delivery platform. *ACS nano* 2008, 2(8):1696-1702.

14. Grottkau BE, Cai X, Wang J, Yang X, Lin Y: Polymeric nanoparticles for a drug delivery system. *Current drug metabolism* 2013, 14(8):840-846.

15. Belliveau NM, Huft J, Lin PJ, Chen S, Leung AK, Leaver TJ, Wild AW, Lee JB, Taylor RJ, Tam YK *et al*: Microfluidic Synthesis of Highly Potent Limit-size Lipid Nanoparticles for In Vivo Delivery of siRNA. *Molecular therapy Nucleic acids* 2012, 1:e37.

16. Ranjan AP, Mukerjee A, Gdowski A, Helson L, Bouchard A, Majeed M, Vishwanatha JK: Curcumin-ER Prolonged Subcutaneous Delivery for the Treatment of Non-Small Cell Lung Cancer. *Journal of biomedical nanotechnology* 2016, 12(4):679-688.

17. Chignell CF, Bilski P, Reszka KJ, Motten AG, Sik RH, Dahl TA: Spectral and photochemical properties of curcumin. *Photochemistry and photobiology* 1994, 59(3):295-302.

18. Berezin MY, Achilefu S: Fluorescence lifetime measurements and biological imaging. *Chemical reviews* 2010, 110(5):2641-2684.

19. Bose RJ, Lee SH, Park H: Lipid-based surface engineering of PLGA nanoparticles for drug and gene delivery applications. *Biomaterials research* 2016, 20:34.

CHAPTER V

DEVELOPMENT OF BIODEGRADABLE NANOCARRIERS LOADED WITH A MONOCLONAL ANTIBODY

I. ABSTRACT

Treatments utilizing monoclonal antibody therapeutics against intracellular protein-protein interactions in cancer cells have been hampered by several factors, including poor intracellular uptake and rapid lysosomal degradation. Our current work examines the feasibility of encapsulating monoclonal antibodies within poly(lactic-co-glycolic acid) (PLGA) nanoparticles using a water/oil/water double emulsion solvent evaporation technique. This method can be used to prepare protective polymeric nanoparticles for transporting functional antibodies to the cytoplasmic compartment of cancer cells. Nanoparticles were formulated and then characterized using a number of physical and biological parameters. The average nanoparticle size ranged from 221 to 252 nm with a low polydispersity index. Encapsulation efficiency of 16%–22% and antibody loading of 0.3%–1.12% were observed. The antibody molecules were released from the nanoparticles in a sustained manner and upon release maintained functionality. Our studies achieved successful formulation of antibody loaded polymeric nanoparticles, thus indicating that a PLGA-based antibody nanoformulation is a promising intracellular delivery vehicle for a large number of new intracellular antibody targets in cancer cells.

II. INTRODUCTION

Approximately 30 monoclonal antibody therapeutics have been approved for clinical use in the United States and more are in various stages of clinical trials [1]. Research and treatments with antibodies used for cancer therapy have been limited to targeting extracellular or secreted antigens because in the infrequent event that non-receptor mediated endocytosis of an antibody occurs, the antibody will be destined for the harsh environment of the lysosome and thus rendered inactive [2]. One strategy to overcome this obstacle and achieve intracellular delivery of antibodies is to encapsulate the antibody molecules within polymeric nanoparticles. The nanoparticles can protect the antibody while in transit through the circulation and when the nanoparticles are endocytosed by the cancer cells they have the ability to rapidly escape the lysosomal compartment [3], degrade, and release the antibody molecules inside the cancer cell's cytoplasmic compartment.

Poly(lactic-co-glycolic acid) (PLGA) is a biodegradable polymer that has been approved by the US Food and Drug Administration [4]. Numerous examples exist in the literature demonstrating PLGA as a controlled release nanoparticle vehicle for various drug molecules including: small hydrophobic molecules [5], nucleic acids [6], and proteins [7]. In addition, many groups have used antibodies on the outside of the nanoparticles for targeting purposes. However, to our knowledge no studies have reported using antibodies encapsulated inside PLGA nanoparticles for cancer treatment and research.

For characterization purposes we have chosen to use an antibody against AnnexinA2 (AnxA2) as a model antibody in this formulation. AnxA2 is a calcium-dependent phospholipid binding protein found on various cell types. AnxA2 is highly expressed in certain cancer cells and plays multiple roles in regulating cellular functions including: angiogenesis, proliferation, apoptosis, cell migration, invasion, and adhesion [8]. Anti-AnxA2 antibody was chosen because its functionality can be validated in both western blots and immunofluorescence experiments.

In this article, we present evidence that monoclonal antibodies can be successfully encapsulated using a modified water in oil in water (w/o/w) double emulsion solvent evaporation technique. Further, we demonstrate that when using this method of antibody encapsulation, target binding of the released antibody is maintained. This strategy for delivering functional antibodies inside cancer cells has the potential to open up a large number of new targets for antibody based therapeutics.

III. RESULTS AND DISCUSSION

The double emulsion with solvent evaporation technique yielded antibody encapsulation efficiency ranging from 16% to 22% (Figure 22). This represents an adequate value given the large dimensions of IgG molecules (~14.2 nm across the longest dimension) [9] and hydrophilic nature of antibodies. Higher drug loading can be achieved if nanoparticle size is increased, however the goal of this formulation was to create nanoparticles that would be able to utilize the enhanced permeability and retention effect for delivery to solid tumors [10]. Thus, the hydrodynamic diameter was limited to less than ~250 nm in all formulations (Figure 22). As

expected, the hydrodynamic size of the nanoparticles tended to slightly increase as we increased the initial antibody concentration and more antibody molecules were loaded into the nanoparticles (Figure 22).

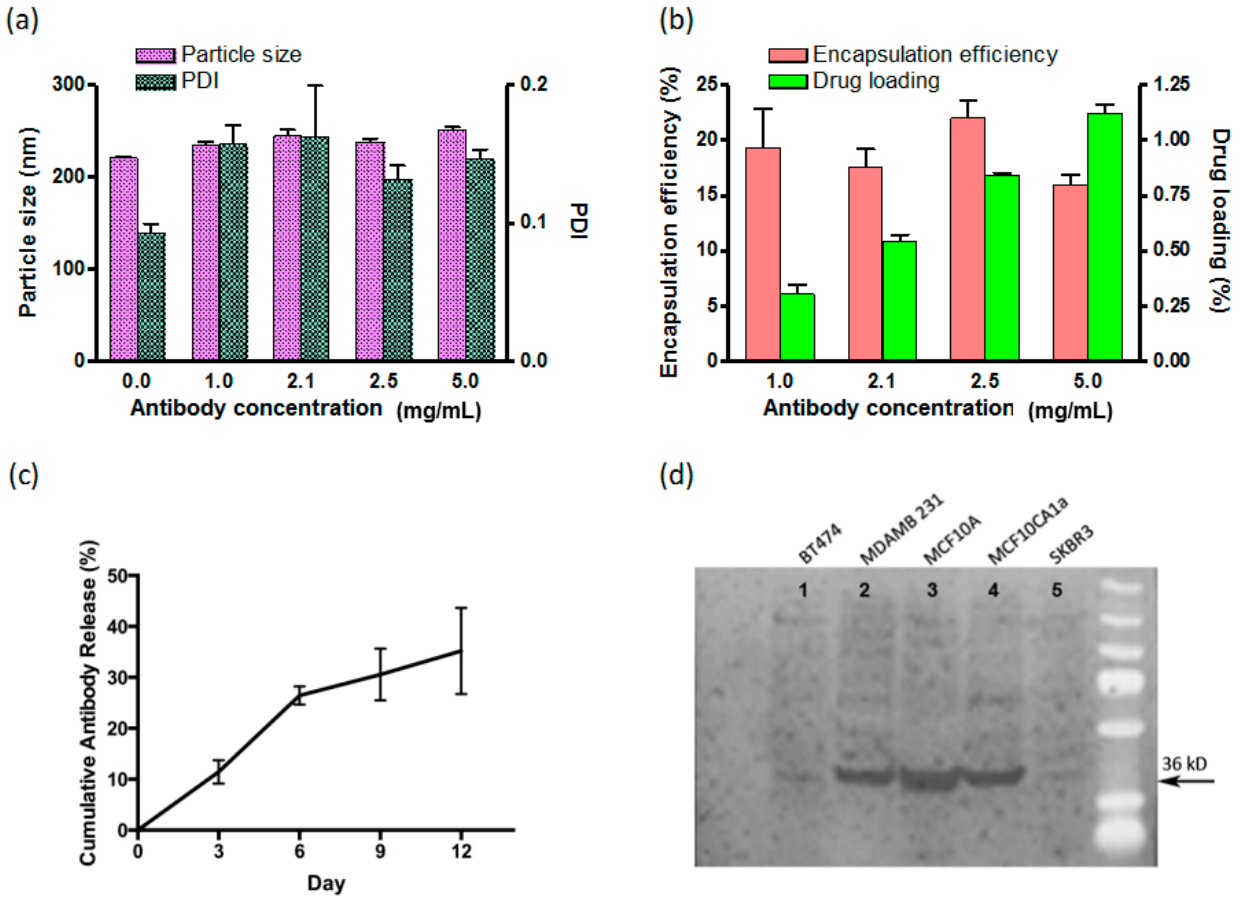

Figure 22: Characterization of anti-Anx A2 antibodies encapsulated within nanoparticles

(a) Dynamic Light Scattering (DLS) measurement of the size and polydispersity index (PDI) of the nanoparticles; **(b)** Encapsulation efficiency and drug loading of the nanoparticles; **(c)** Twelve day cumulative antibody release experiment; and **(d)** Immunoblot of whole cell lysates from breast cancer cell lines showing functional binding of released AnnexinA2 (AnxA2) antibody from the nanoparticle at 36 kD. The BT474 and SKBR3 cell lines are known to have very low

AnxA2 expression. MDAMB231, MCF10A, and MCF10CA1a cell lines are known to have high AnxA2 expression. (Bars represent standard error of the mean, n = 3).

Release kinetics performed over the course of 12 days revealed the antibodies were released from the nanoparticles in a sustained manner (Figure 22 c).

Finally, antibody functionality was assessed after release from the nanoparticles to demonstrate that in fact binding specificity of the antibody remained intact after undergoing the chemical and physical stresses during the encapsulation process. The released antibody was able to show a strong signal when binding to the whole cell lysates from cell lines of high AnxA2 expression while minimal signal was detected on low AnxA2 cell lines (Figure 22). In addition, immunofluorescence staining using the released antibody also showed maintained antibody functionality (Figure 23).

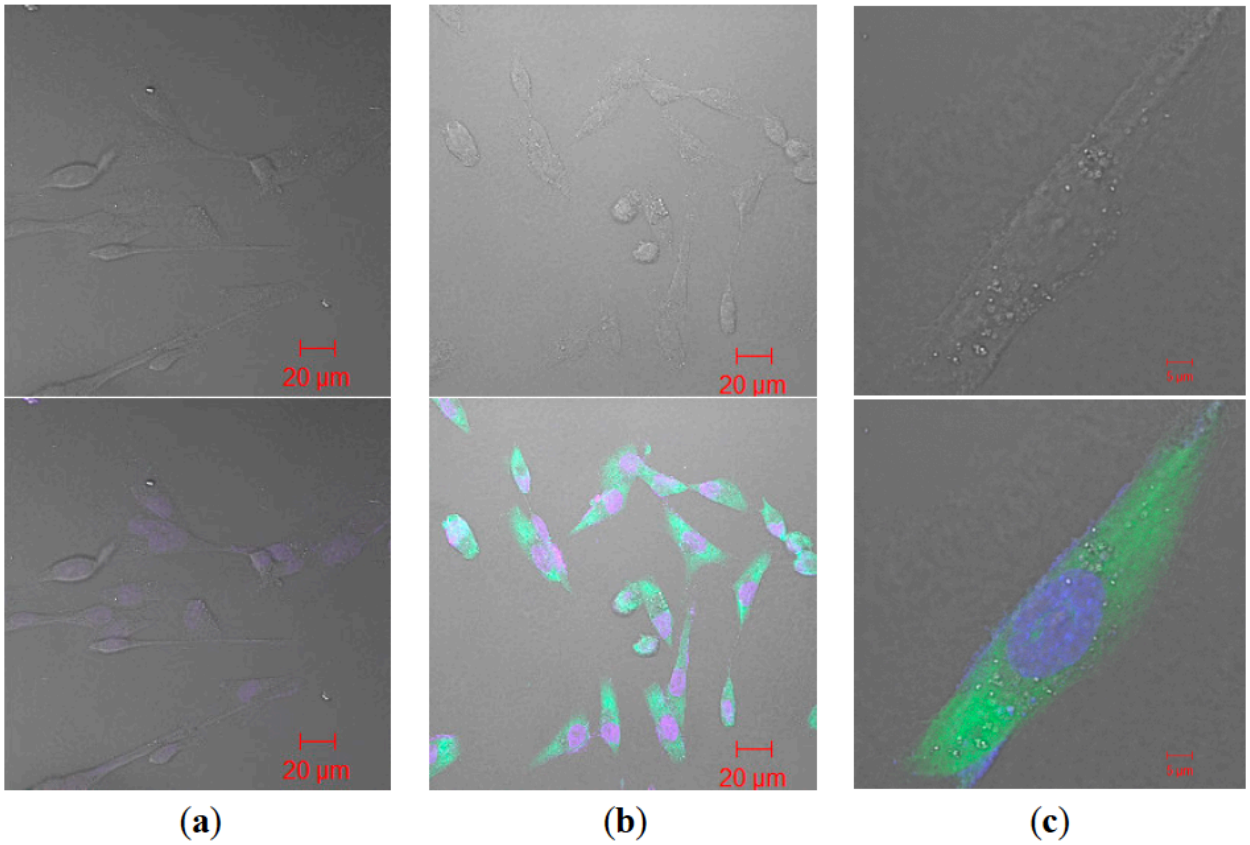

Figure 23: Immunofluorescence of released anti-AnxA2 antibody from nanoparticle (a) MDAMB 231 cells treated with heat inactivated anti-AnxA2 antibody released from nanoparticle; **(b)** Lower magnification of MDAMB 231 cells treated with anti-AnxA2 antibody released from nanoparticles; **(c)** Higher magnification of single MDAMB 231 cell treated with released anti-AnxA2 antibody. Green = Alexa fluor 488 tagged secondary antibody. Blue = DAPI.

IV. MATERIALS AND METHODS

Anti-AnxA2 encapsulated PLGA nanoparticles (AbNPs) were prepared using a double emulsion

with solvent evaporation technique. Mouse monoclonal anti-AnxA2 (D1/274.5) antibody was a kind gift from Dr. Tony Hunter, Salk Institute for Biological Studies, La Jolla, CA, USA. D1/274.5 was generated from hybridoma cells and are isotype IgG2a. Encapsulation was performed with AnxA2 antibody (D1/274.5) used at various initial concentrations (0, 1, 2.1, 2.5, 5 mg/mL) by diluting in PBS pH 7.4, added into 2 mL PLGA (50:50) ethyl acetate solution, mixture was vortexed for 30 s, then sonicated on ice at 40% continuous intensity for two 30 s time periods with a ten second break in between. Primary emulsion was transferred into 10 mL of 2% poly(vinyl alcohol) (PVA) and sonicated on ice at 40% intensity on intermittent setting for 1 min. Organic solvent was evaporated at atmospheric pressure by magnetic stirring. Next, nanoparticles were washed three times by centrifuging three times at 18,000 g for 40 min and washed with water at the end of each centrifugation time point. The nanoparticles were resuspended on the final wash, flash frozen, and lyophilized. The nanoparticles were stored at 4 °C for further use.

Nanoparticles were characterized to determine hydrodynamic particle size and polydispersity index (PDI) by dynamic light scattering using the Zetasizer Nano ZS instrument (Malvern Ltd., Worcestershire, UK).

Encapsulation efficiency was determined by setting up a standard curve of known anti-AnxA2 antibody in Bis-Tris polyacrylamide gels. Samples were prepared by addition of 2 mg AbNP into 5% 2-mercaptoethanol (BME) reducing dye, boiled, and loaded into the gel. Coomassie Brillant

Blue R-250 staining (Thermo Fisher Scientific Inc., Rockford, IL, USA) was used for quantification using linear regression calculations based on Image J analysis of heavy chains.

In vitro release kinetics were carried out by addition of 2 mg of AbNP to 1 mL of PBS solution pH 7.4. Nanoparticles were continuously mixed at 37 °C. At specified time points, tubes were centrifuged at 18,000 g for 40 min to pellet the nanoparticles. Supernatant with released antibody were collected and quantified by bicinchoninic acid (BCA) kit (Thermo Fisher Scientific Inc., Rockford, IL, USA).

Antibody functionality after release from nanoparticles was determined by adding the AbNP to 1 mL of PBS pH 7.4 and continuously mixed for 9 days at 4 °C. Nanoparticles were then pelleted by centrifugation at 18,000 g for 40 min, supernatant was collected and released antibody was used as the primary antibody for western blot detection of AnxA2 in various breast cancer whole cell lysates.

Confocal images were obtained using LSM 510 confocal microscope (Zeiss, Pleasanton, CA, USA) after human breast cancer cells (MDA-MB-231) were grown on coverslips, permeabilized, fixed, treated with anti-AnxA2 that was released from nanoparticles, and labeled with Alexa Fluor 488 goat anti-mouse IgG secondary antibody (Sigma Aldrich, Saint Louis, MO, USA).

V. CONCLUSION

This study provides evidence for utilizing PLGA nanoparticles as sustained release vehicles for the intracellular delivery of therapeutic antibodies to cancer cells. Delivery of functional antibodies to the cytoplasmic compartment may enable these antibodies to target numerous aberrant intracellular biomolecules for cancer treatment. Furthermore, this method of antibody delivery might also have utility studying various biological processes in the context of live intracellular imaging with fluorescently labeled antibodies.

VI. REFERENCES

1. Mueller, K. The future is now. Science 2013, 341, 1191.

2. Shih, L.; Thorpe, S.; Griffiths, G.; Diril, H.; Ong, G.; Hansen, H.; Goldenberg, D.; Mattes, M. The processing and fate of antibodies and their radiolabels bound to the surface of tumor cells in vitro: A comparison of nine radiolabels. J. Nucl. Med. 1994, 35, 899–908.

3. Panyam, J.; Dali, M.; Sahoo, S.; Ma, W.; Chakravarthi, S.; Amidon, G.; Levy, R.; Labhasetwar, V. Polymer degradation and in vitro release of a model protein from poly(D,L-lactide-co-glycolide) nano-and microparticles. J. Control. Release 2003, 92, 173–187.

4. Lü, J.; Wang, X.; Marin-Muller, C.; Wang, H.; Lin, P.; Yao, O.; Chen, C. Current advances in research and clinical applications of PLGA-based nanotechnology. Expert Rev. Mol. Diagn. 2009, 9, 325–341.

5. Dhar, S.; Gu, F.; Langer, R.; Farokhzad, O.; Lippard, S. Targeted delivery of cisplatin to prostate cancer cells by aptamer functionalized Pt (IV) prodrug-PLGA–PEG nanoparticles. Proc. Natl. Acad. Sci. USA 2008, 105, 17356–17361.

6. Braden, A.; Kafka, M.; Cunningham, L.; Jones, H.; Vishwanatha, J. Polymeric nanoparticles for sustained down-regulation of annexin A2 inhibit prostate tumor growth. J. Nanosci. Nanotechnol. 2009, 9, 2856–2865.

7. Panyam, J.; Zhou, W.Z.; Prabha, S.; Sahoo, S.K.; Labhasetwar, V. Rapid endo-lysosomal escape of poly(D,L-lactide-co-glycolide) nanoparticles: Implications for drug and gene delivery. FASEB J. 2002, 16, 1217–1226.

8. Lokman, N.A.; Ween, M.P.; Oehler, M.K.; Ricciardelli, C. The role of annexin A2 in tumorigenesis and cancer progression. Cancer Microenviron. 2011, 4, 199–208.

9. Sarma, V.R.; Silverton, E.W.; Davies, D.R.; Terry, W.D. The three-dimensional structure at 6 A resolution of a human γG1 immunoglobulin molecule. J. Biol. Chem. 1971, 246, 3753–3759.

10. Acharya, S.; Sahoo, S.K. PLGA nanoparticles containing various anticancer agents and tumor delivery by EPR effect. Adv. Drug Deliv. Rev. 2011, 63, 170–183.

CHAPTER VI

SUMMARY AND FUTURE DIRECTIONS

In this thesis project, successful formulation, characterization, and *in vivo* testing were performed on a variety of nanoparticle delivery systems designed to improve treatment of bone metastatic prostate cancer. Each project has focused on applying nanoparticle engineering principles to solve clinically relevant problems. In targeting the bone lesions, we focused our efforts on targeting the microenvironment rather than the classical approach of targeting an upregulated tumor specific antigen. This approach of targeting the bone microenvironment eliminates the concern of heterogeneous expression of tumor associated antigens on cancer cells.

In the second chapter, the effectiveness of targeting the hydroxyapatite structure of the bone was demonstrated as a successful treatment for bone metastatic lesions. One of the main benefits of this approach is that most materials utilized are FDA approved in a variety of contexts so low levels of toxicity are anticipated. The FDA issues guidance and general expectations for the development of both nanotechnology products and cancer therapeutics. These documents are meant to serve as considerations that should be addressed during the development phases and prior to filing an investigational new drug application with the FDA. The guidance provided for nanotechnologies focuses on thorough characterization of the product, especially the features that are important due to the unique properties of materials created at the nanoscale. Drug release kinetics from the nanoparticle as well as physical and chemical characterization are very important for the nanoparticles we have developed.

The guidance the FDA provides for preclinical characterization of cancer therapeutics has more concrete recommendations. Efficacy in a relevant model is an important consideration. In this

study, the animal model we chose was an intraosseous injection of prostate cancer cells. Another model that may help reinforce the efficacy is an intra-cardiac model of bone metastasis. Clinically most prostate cancer lesions that develop in the bone are osteoblastic in nature, thus an additional cell line that develops osteoblastic lesions may provide more information for clinical context and deeper insight into the mechanism of these nanoparticles. Further, models of pain behavior with larger numbers of mice to assess reduction in pain will also benefit this project.

Defining the toxicity of the product under development is also an important consideration. A future study that should be performed in the development process is a dose escalation study to define the maximum tolerated dose. We anticipate the major toxicities that will develop at the higher doses of cabazitaxel to be like that seen in clinical trials but potentially to a lesser degree due to the targeted nature of the nanoparticles. The main adverse events in clinical trials were: pancytopenia, febrile neutropenia, sepsis, diarrhea, as well as others. Studies can be devised to measure the main toxicities by performing *in vivo* monitoring with blood analysis that is correlated to the dosage of the nanoparticle being administered. The other factor that may cause toxicity but probably to a lesser degree is the alendronate molecule. We anticipate this toxicity may be significantly lower than what is seen in the bisphosphonate drugs because the quantity of alendronate used for targeting purposes should be lower than when used solely in the therapeutic context. Nevertheless, the main clinical adverse reactions that occur with alendronate are esophagitis, esophageal erosion, hypersensitivity, and osteonecrosis of the jaw. These toxicities can be monitored at the termination of the experiment with histology sections and comparison to controls. We don't expect toxicities to be associated with the PLGA nanoparticles based on preclinical and clinical safety reports.

The third chapter validated the proof of concept that a bioinformatics approach can be used to identify and enhance targeting of bioinspired nanoparticles. Future aims of this project include: re-engineering the manufacturing process of the P-BiNPs, tumor efficacy experiments, and identification of other factors important for homing to various organs. Re-engineering the manufacturing process is a critical step in allowing scale up from lab studies to the tumor efficacy and toxicity experiments. The current manufacturing process in the lab involves an extrusion process for development. This process results in relatively low yield of product making the process difficult for larger proof of concept studies. A future manufacturing process will incorporate a microfluidics process for scaling up the production. Developing liposomes from the cancer membranes or other cell types in lieu of the hybrid type of nanoparticles remains another option. This may serve to increase the product that is produced but may suffer from being a less stable drug delivery system.

Efficacy experiments will focus on utilizing the bone metastatic prostate cancer model that we have used in other studies. Following tumor efficacy experiments, toxicity experiments should be performed with these nanoparticles in a similar manner as described for the alendronate coated nanoparticles. Incorporation of alternative targets that have been identified from the bioinformatics analysis to target other organs may serve to improve the function of these nanoparticles in the animal studies. Additional entities in the nanoparticle design may serve for improved targeting or other useful biological purposes.

For the nanoparticles described in this thesis to translate to clinical realities, more effort must focus on addressing the scale up process. We have addressed this challenge in the fourth chapter and have proposed a facile microfluidic synthesis method to quickly optimize and scale up the nanoparticle engineering process. We are hopeful that integrating this process in the future workflow of the nanoparticle synthesis steps at the early stages will provide benefits in the later developmental stages when large amounts of nanoparticles are required.

The fifth chapter describes our early efforts at encapsulating an antibody inside of a polymeric nanoparticle. At the time of writing this thesis there were approximately 25 approved antibodies by the FDA for cancer therapy. The majority, if not all, bind to targets on the extracellular membrane. There are many potential targets intracellularly that may be explored through antibody protein-protein interactions that were not previously able to be studied in this manner. Through encapsulation of antibodies inside nanoparticles we may be able to efficiently deliver more antibodies inside cancer cells. Further studies on maintenance of antibody binding after release from the nanoparticle will be needed to ensure the antibodies still have strong affinity for their targets.

It is my sincere hope that concepts and publications derived from this thesis will help guide future efforts for targeted therapy and improve the lives of patients with cancer.